Doctor of Philosophy in

"Information and Communications Technologies

Radar and Remote Sensing"

Department of Information Engineering, Electronics and Telecommunications

Cycle XXIX

_____

Ph.D. Dissertation

THEORETICAL MODELING OF DUAL-FREQUENCY SCATTEROMETER RESPONSE: IMPROVING OCEAN WIND AND RAINFALL EFFECTS

Candidate

Federica Polverari

Matr. 1205617

Tutor

Prof. Frank S. Marzano

Ph.D. Program Coordinator

Prof. Maria-Gabriella Di Benedetto

Academic Year 2016-2017

This research has been carried out in collaboration with
NASA-Jet Propulsion Laboratory, California Institute of Technology
under the mentorship of Dr. Svetla M. Hristova-Veleva and Dr. Joseph Turk.

Contents

Summary

Ocean surface wind is a key parameter of the Earth's climate system. Occurring at the interface between the ocean and the atmosphere, ocean winds modulate fluxes of heat and moisture as well as gas exchanges. They reflect the lower branch of the atmospheric circulation and represent a major driver of the ocean circulation [Bourassa *et al*., 2010(a); Fairall *et al*., 2010]. Studying the long-term trends and variability of the ocean surface winds is of key importance in our effort to understand the Earth's climate system and the causes of its changes on a variety of temporal and spatial scales. To this end, a consistent and long-term ocean surface winds Climate Data Record (CDR) is critically needed to understand several phenomena [Atlas *et al*., 2011] - from convective organization and its upscale growth, to the Madden-Julian Oscillation evolution and El Niño/Southern Oscillation events [DeMott *et al*., 2015] - and to evaluate whether such phenomena are properly reflected in climate models.

Spaceborne scatterometers provide high-resolution measurements of surface winds. By being assimilated into weather prediction and forecast models, scatterometer wind retrievals have significantly improved tropical cyclones forecasting, marine now-casting as well as numerical weather predictions [Bourassa *et al*., 2010(b)]. Currently, more than three decades of surface wind data are available from spaceborne scatterometer/radiometer missions and the Ocean Vector Wind Science Team is now working to inter-calibrate all these measurements with the aim of building a consistent Global Ocean Wind CDRs. In this scenario, it is crucial to have accurate scatterometer wind retrievals as well as consistency among measurements from scatterometers at different frequencies [Wentz *et al*., 2016].

Wind retrievals are obtained by inversion algorithms of geophysical model functions (GMFs) that represent the relationship between ocean backscatter and the wind parameters [Wentz and Smith, 1999; Hersbach *et al*., 2007]. Such relationship is defined on empirical basis by either correlating collocated backscatter with buoy-based wind measurements or by fitting satellite data with weather model winds. Being measurement-dependent, the GMFs reflect the uncertainty in the measurements and they are not properly defined in all weather conditions, causing errors in the wind retrievals [Soisuvarn *et al*., 2013; Ricciardulli *et al*., 2015]. In addition, winds retrieved from sensor-specific GMFs may compare differently with modeled winds and the use of these empirical functions complicates the understanding of the sources of these inconsistencies, affecting the reliability of the CDRs.

Theoretical models of ocean backscatter have the big potential of providing a more general and understandable relation between the measured microwave backscatter and the surface wind field than empirical models. This theoretical model will not only help to correct the limit of the current GMFs, but it will also help to interpret the ocean response for complex ocean and atmospheric conditions. Therefore, the goal of this research is to understand and address the limitations of the theoretical modeling, in order to propose a new

strategy towards the definition of an optimized multi-frequency model able to account for the effects of both wind and rain.

To do that, the work is divided in two main steps, consisting in: (i) modeling the ocean response in clear air and (ii) extending the model in presence of rain. It is essential to determine a reliable model in absence of rain before including any additional effect that contributes to the radar signal, therefore, a big effort is done to define a model in rain-free conditions. In this work, we present a new configuration of the Two-Scale Model (TSM), in the attempt to improve the theoretical modeling of the ocean surface backscattering coefficient at different operating frequencies, i.e., Ku-band (13.4 GHz) and C-band (5.3 GHz). This model is combined with the ocean surface wave spectrum as described by Elfouhaily *et al.*, (1997). Two spectrum parameters are adjusted to improve the ocean response sensitivity to the wind. In particular, the tuning strategy is formulated such that arbitrary values are not included, in order to not limit the generality of the model. The validation of the proposed model is performed at Ku-band frequency by using the empirical geophysical model function derived for the Ku-band NASA QuikSCAT Scatterometer as well as real backscatter measurements collected from the Ku-band SeaWinds scatterometer onboard the Advanced Earth Observing Satellite (ADEOS)-II. At C-band frequency, the validation is performed against the CMOD5.n GMF developed for European scatterometers. Although the model shows remarkable results at Ku-band, it reveals discrepancies at C-band. The reason for such discrepancies as well as a possible way to address them are also discussed. Since we are not accounting for non-Bragg scattering mechanism affecting the horizontal polarization, the results are presented in vertical polarization only. The issue related to the ocean backscattering in horizontal polarization is also presented.

The second step of this research is focused on extending the new proposed spectrum model to properly include the ocean surface modifications induced by the impact of the raindrops, on a theoretical basis. Two main rain effects have been included in this spectrum, such as: the short wave damping according to the theory proposed by Nystuen, (1990) and the generation of the ring waves, as shown by Bliven *et al.*, (1997). The results of the ocean backscatter affected by rain are shown at Ku-band only due to the model reliability in rain-free conditions. The magnitude of the rain effects is validated by comparing the results with the model proposed by Contreras and Plant, (2006). The proposed theoretical model is also validated by using actual measurements collected during the ADEOS-II mission from both the SeaWinds scatterometer and the Advanced Microwave Scanning Radiometer (AMSR). The model shows a slight underestimation of the real data. The reason for such disagreement is discussed.

At the end of this work, we were able to clearly formulate outstanding issues of the theoretical modeling of the ocean backscattering and to devise a path for addressing them, providing a framework for future investigations. In particular, this research has revealed the need for new understanding of the frequency-dependent modeling of the surface backscatter in response to the wind-forced surface wave spectrum.

Chapter I

Introduction

## 1.1. Importance of Ocean Wind Retrievals in Climate Change

Understanding and predicting climate variability and trends is one of the most concerning issues regarding our natural system. Significant improvements of climate models and their predictions have been achieved, however, uncertainties remain large and more accurate information is needed. Over the last two decades, it has been recognized that the ocean plays a very important role in the Earth's climate system. The ocean exchanges with the atmosphere large quantities of heat, carbon dioxide, moisture and momentum and this ocean/atmosphere interaction intrinsically determines the long time scales of climate changes [Bourassa *et al*., 2010(a); Fairfall *et al*., 2010]. However, the dynamics at the ocean-atmosphere interface remain poorly understood, leading to significant errors in their model representation and reducing the accuracy of climate models. Surface winds represent one of the key variables needed to interpret the interaction between the ocean and the atmosphere [Bourassa *et al*., 2010(b); Atlas *et al*., 2011]. Surface winds drive the ocean circulation as well as the ocean transport and they are needed to estimate ocean currents. Ocean currents help the heat redistribution through transport of warm water from the equator toward the poles, and in turn regulate the exchange of heat and momentum affecting the global climate [Cronin *et al*., 2010]. As pointed out in the 2007 National Research Council Decadal Survey of Earth Science, accurate measurements of ocean wind vectors are essential to fully characterize the ocean circulation, ocean heat storage and ocean climate forcing.

To this end, spaceborne scatterometer observations are essential since they provide high-resolution measurements of surface wind speed/direction and they guarantee extensive ocean data coverage over a variety of time scales. As pointed out by the recent work from the Ocean Wind Vector Science Team (OVWST) [Wentz *et al*., 2016], at the present time, more than three decades of ocean wind data from both passive radiometers and active scatterometers are available, as shown in Fig. 1.1. This offers a unique opportunity to merge and inter-calibrate all these wind retrievals into a time series of global ocean winds, namely ocean wind Climate Data Record (CDR), in order to provide a complete and continuous picture of the ocean wind variability, necessary for improving the scientific knowledge of the Earth's climate system.

Different institutions like NASA-*Jet Propulsion Laboratory* (JPL), *Remote Sensing Systems* (RSS) and the *Royal Netherland Meteorological Institute* (KNMI), have put significant effort towards this direction and early versions of ocean winds CDRs are already available [Wentz *et al*., 2013; Verhoef *et al*., 2016], but it is extremely important to keep working on evaluating, improving and extending the current CDRs. The OVWST has already planned activities to improve the current CDRs, consisting in wind retrieval validation through in-

situ buoy measurements, wind speed retrievals inter-calibration by multiple sensors and inter-comparison of the multiple version of current CDRs available from different institutions.

Especially now, in the phase of recent and upcoming new observing systems, it is crucial to establish consistent methodologies that lead to instrument-independent and extended CDRs of the ocean winds. In particular, the ISS-based Ku-band NASA's RapidScat scatterometer mission with its unique non-sun-synchronous orbit, provided for the first time the ability to sample the ocean winds throughout the diurnal cycle, detecting significant diurnal signal. Due to its orbits, the ISS-RapidScat scatterometer also provided a significant increase in the rate at which close collocated data are accumulated, essential for inter-calibrating different instruments. The data from this mission will be soon integrated into the current CDRs, as well as the data from the very-recent Ku-band Scatterometer Satellite-1 (ScatSat-1) mission – data are already disseminated to NASA-JPL – successfully launched on September 2016 by the *Indian Space Research Organization* (ISRO) as follow-on of OSCAT (Oceansat-II) to continue the global ocean wind data acquisition. The complete evaluation will become even more important when incorporating future new wind products that could be available from Ka or L-band scatterometer observations.
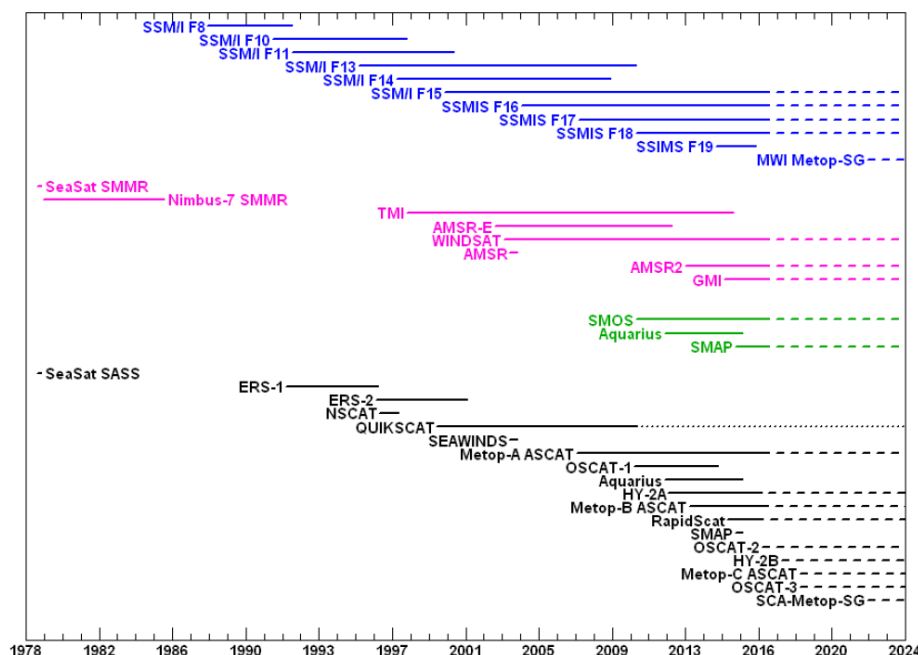
Figure 1.1. Time chart of the past/present/future missions for ocean scatterometry and microwave radiometry. The black lines show the series of microwave scatterometers measuring ocean vector winds. The dotted line extending the QuikSCAT from 2009 onward denotes the non-spinning phase of operation. The blue lines show the SSM/I and SSMIS instruments on the series of DMSP satellite platforms numbered F8 to F20. These sensors only provide ocean wind speed, not direction. The pink lines show the microwave radiometers providing measurements of sea surface temperatures, wind speed, water vapor, clouds, and rain rates. WindSat is the only microwave radiometer that also provides wind direction due to the inclusion of polarimetric channels. The green lines show the L-band radiometers SMOS, Aquarius, and SMAP, suited for measuring high winds in storms [Wentz *et al.*, 2016].

1.2. Current Status of Scatterometer Ocean Surface Wind Retrievals

1.2.1 Principles of Ocean Scatterometry

Spaceborne scatterometers are active instruments designed to measure ocean surface winds by observations over ocean. Several spaceborne scatterometer missions have been launched in the last 38 years, starting from the NASA Seasat-A Satellite Scatterometer in 1978, until 2016 with the very-recent ISRO ScatSat-1 mission, as shown in Fig. 1.1. These scatterometers work at microwave frequencies such as: C-band (~5.3 GHz) for the ESA ERS-1, ERS-2 and ESA/EUMETSAT ASCAT missions, Ku-band (~13.4 GHz) for NASA NSCAT, QuikSCAT, SeaWinds, RapidScat and ISRO ScatSat scatterometers and L-band (~1 GHz) for the Aquarius mission, which is a joint venture between NASA and the Argentinean Space Agency.

Ocean wind scatterometry is based on the assumption that the microwave scatterometer signal is sensitive to those ocean waves, referred to as capillary/gravity-capillary (hereafter capillary) waves, which are directly generated by the surface winds. In particular, the scattering mechanisms from this ocean waves is described by the *Bragg resonance theory* [Wright, 1968; Valenzuela, 1978], which states that the incident electromagnetic waves, characterized by wavelength λ and incident angle θ, are in resonance with those ocean surface waves of comparable wavelength λ_B, that satisfy the Bragg resonance condition expressed in Eq. (1.1) (where n is an integer). At microwave frequencies, the wind-driven capillary waves meet this condition, so that they are responsible for the radar backscattered power.

$$\lambda_B = \frac{n}{2} \frac{\lambda}{\sin \theta} \tag{1.1}$$

The quantity of primary interest in ocean remote sensing, as well as for general remote sensing applications, is the so-called *Normalized Radar Cross Section* (NRCS), also known as *ocean surface backscattering coefficient*, which is derived by the surface backscattered power through the radar equation. This equation describes the relation between the radar transmitted and received power as function of the parameters characterizing the radar system as well as the illuminated target itself. In order to define this relation, let us consider a radar antenna, characterized by gain G, which transmits a power W_t towards a scattering element, whose distance from the antenna is equal to R [m]. The incident power density P_i to this scattering element, is defined as [Stoffelen, 1998]:

$$P_i = W_t G \frac{1}{(4\pi R^2)}. \tag{1.2}$$

The factor $1/(4\pi R_t^2)$ quantifies the spreading loss, which represents the reduction in power density associated with the power spreading over a sphere of radius R surrounding the antenna.

By assuming that:

    (i)   the effective receiving area of the scattering element is a portion of the total area and it is defined as A_{rs};

    (ii)   the scattering element is characterized by a gain G_s toward the receiver;

    (iii) a fraction f_a of the incident power is absorbed by the scattering element;

then the power reradiated by the scattering element can be defined as $P_i A_{rs} G_s (1 - f_a)$. These factors are combined together into one single factor that describes the radar cross section (RCS) σ as [Ulaby *et al.*, 1982]:

$$\sigma = A_{rs} G_s (1 - f_a). \tag{1.3}$$

Therefore, in case of a *monostatic radar*, whose transmitter and the receiver are placed in the same location, by assuming the effective area A_r of the receiver as $A_r = G \lambda^2 / 4\pi$, the power received back to the antenna from a single scattering element is [Ulaby *et al.*, 1982]:

$$W_r = A_r A_{rs} G_s (1 - f_a) P_i = \frac{\lambda^2}{(4\pi)^3} \frac{W_t G^2}{R^4} \sigma. \tag{1.4}$$

As shown in Fig. 1.2, natural surfaces as the ocean surface, can be considered as distributed target composed by several scattering elements and it is reasonable to assume that each illuminated element of area dA acts as single element, which defines a received power dW_r as:

$$dW_r = \frac{\lambda^2}{(4\pi)^3} \frac{W_t G^2}{R^4} d\sigma. \tag{1.5}$$

Therefore for the entire area A_i illuminated by the radar, the total received power is [Stoffelen, 1998]:

$$W_r = \int_{A_i} \frac{\lambda^2}{(4\pi)^3} \frac{W_t G^2}{R^4} d\sigma. \tag{1.6}$$

For such distributed target, the dimensionless radar cross section per unit surface, denoted as $\sigma^0 = \langle \sigma / dA \rangle$, represents the NRCS, which intrinsically contains the physical properties of the illuminated area and it is indirectly connected to those geophysical parameters that contribute to the modification of surface. In case of the backscattered power from the ocean surface, by being generated by the wind-driven capillary waves, the ocean surface NRCS contains information of surface winds. For this reason, ocean scatterometry applications are generally based on forward models, which describe the relationship between σ^0 and surface wind

speed/direction, as well as inverse algorithm to retrieve such parameters from σ^0 measurements. Therefore, it is essential to carefully define both forward and inverse models as well as to perform accurate instrument calibration/validation, in order to reduce the sources of uncertainty in the radar measurements and in the parameters estimations.
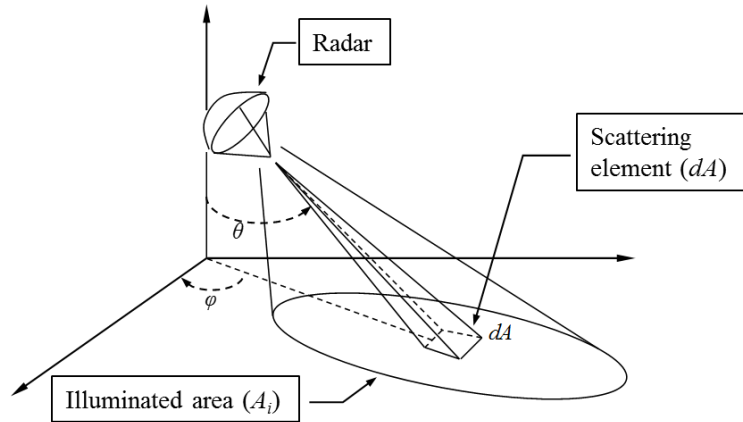
Figure 1.2. Schematic scattering mechanisms from a distributed scatter (natural surface) [credit: Marcantoni D.].

1.2.2 Empirical Ocean Surface Scattering Models

Scatterometer wind vectors are currently derived by retrieval algorithms from empirical Geophysical Model Functions (GMFs), expressed in Eq. (1.7). It describes the relationship between the NRCS ($\sigma°$) and the surface wind speed (ws) and relative wind direction φ_R, which corresponds to the angle between the wind and the radar look direction [Hersbach, 2008; Ricciardulli *et al*., 2015]:

$$\sigma° = f(ws, \varphi_R) \cong \sum_{i=0}^{N} B_i(ws)_{pol} \cos(i\varphi_R). \tag{1.7}$$

Such equation is generally truncated up to the second order. By being a periodic function with respect to φ_R, the GMF retrieval algorithm returns wind direction solutions 180° apart. To derive the correct wind solution, an ambiguity removal algorithm is used along with a quality control to determine the accuracy of each wind retrieval. The coefficients $B_i(ws)_{pol}$ carry information of the surface winds such that: B_0 carries information on wind speed intensity, B_2 describes the upwind ($\varphi_R = 0°$) and crosswind ($\varphi_R = 90°$) asymmetry, which is used to determine the wind direction, while B_1 is used to resolve the remaining 180° ambiguity. These coefficients are defined on empirical basis by correlating the scatterometer $\sigma°$ observations with wind measurements from Numerical Weather Prediction (NWP) models, like the European Centre for Medium-range Weather Forecasting (ECMWF), or other observed winds used as truth such as collocated

radiometer winds and in-situ buoy measurements. By being dependent on the scatterometer dataset, the GMFs are scatterometer-specific model functions, therefore, for different scatterometer frequencies, the corresponding GMF is developed. Several institutions like *NASA-JPL* and *RSS*, *KNMI* and ICM-CSIC (*Institut de Ciences de Mar*) have been intensively working on developing refined GMFs [Verohef *et al*., 2008; Ricciardulli *et al*., 2015], quality control systems [Portabella *et al*., 2001; Portabella *et al*., 2012; Lin, 2015] and ambiguity removal algorithms [Stiles *et al*., 2002; Fore *et al*., 2014], in order to provide accurate estimates of scatterometer ocean surface winds. In addition, these institutions are now working on reconciling the different retrieval functions in order to define a single GMF for each type of instrument [Stoffelen *et al*., 2016].

However, since the GMFs are measurement-dependent, it is difficult to account for all those effects that may compromise the quality of the wind estimates. Indeed, the lack of collocated scatterometer observations and "true" measurements in very high wind conditions and rain events, reduces the accuracy of the GMF, introducing a source of error in the retrieved wind. As an example, the C-band GMF CMOD5.n [Hersbach *et al*., 2007], developed for the ESA ERS-1 and ERS-2 and then adapted to the ASCAT winds by KNMI, reveals an underestimation of the ASCAT wind retrievals at wind speed higher than ~20 m/s with a bias increasing with the wind speed. The *National Oceanic and Atmospheric Administration (NOAA)* has developed an empirical high-wind-speed GMF, named CMOD5.h, with the aim to cover the ASCAT high wind portion [Soisuvarn *et al*., 2013]. Another example is the Ku-band GMF, named Ku-2011, developed by RSS [Ricciardulli *et al*., 2015]. Such GMF has been developed by using the radiometer WindSat wind data in non-rainy conditions, so that the wind retrievals may be largely affected by rain especially at low winds. Furthermore, recent findings show that, besides wind and rain, additional factors play an important role in the backscattered signal from the ocean surface. The work of Lin *et al*. (2015) shows that rain induces wind downbursts on the ocean surface with strong gust fronts, and as such, rain is also associated with enhanced wind variability that may significantly affect the signal. In addition, Wang *et al*. (2016) have shown that the sea surface temperature (SST) variability may also have a strong impact on the ocean backscatter. The SST modulates the ocean surface roughness by inducing a decrease of the dynamic viscosity of the water, causing a redistribution of the wind-driven ocean waves and in turn affecting the backscattering signal. Therefore, all these physical phenomena affecting the radar signal as rain, wind variability and SST, may degrade the quality of the wind retrievals if they are not properly compensated for.

While enhanced rain-flagging techniques as well as improved quality control systems have proved to be a valuable approach to support the inversion algorithms of the GMFs, the impact of these additional factors on $\sigma°$ remains not fully quantified and the physical reasoning is still not entirely understood, making difficult to include these effects in the GMFs and in turn leading to remaining uncertainties in the wind retrievals. In particular, these additional effects have a different impact at different radar frequency, therefore, they need to be carefully compensated in order to guarantee consistency in the scatterometer-specific wind estimates. The recent studies carried out by the Wentz *et al*. (2016) shows that surface winds retrieved with current GMFs from different scatterometers compare differently to reference winds. Figure 1.3 shows two global maps of

wind speed differences for the C-band ASCAT minus the Global Precipitation Mission (GPM) Microwave Imager (GMI) radiometer and the Ku-band NASA scatterometer RapidScat minus the WindSat radiometer during 2014-2015. Here, the radiometer winds are used as a reference. These two maps compare differently and, in addition, they show interesting features consisting in geographical patterns of the scatterometer/radiometer differences. The causes of such differences are still not fully understood and further investigations are already planned, but they reveal that there are still uncertainties in the current wind observations that the current empirical GMFs are not entirely able to address.
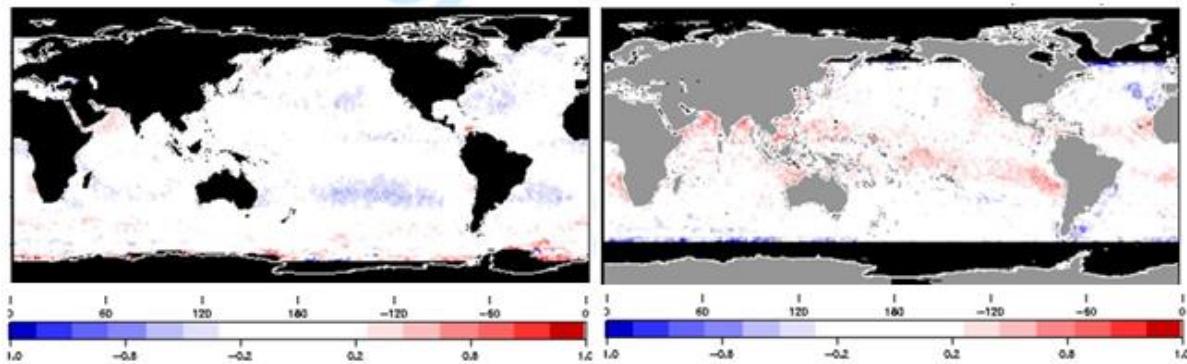
Figure 1.3. Wind speed differences of ASCAT-A minus GMI (left) and RapidScat minus WindSat (right). The ASCAT-A/GMI results are a 2-year average (2014-2015), and the time collocation is 2 hours. The RapidScat/WindSat results are averaged from October 2014 to August 2015 and the time collocation window is1.5 hours. Color scale is in units of m/s [Wentz *et al.*, 2016].

1.3 Goals of the Research: From Empirical to Theoretical Models

Relying entirely on empirical models to address the recent shortcomings seen in the wind retrievals as well as for the design of future scatterometry missions is not advisable. The theoretical models have the big potential to describe the relation between the radar backscattering and the ocean surface wind in a more comprehensible way than empirical models and they also allow the inclusion of additional effects that may compromise such relation. Such model is highly needed by the scientific community. It gives the opportunity to improve the knowledge of the physics of the scatterometer observations, to benefit the understanding of the limits of the current GMFs to quickly develop model functions for new instruments and it is also useful to provide information of the actual surface effects that compromise the scatterometer measurements. Such knowledge is extremely important in the phase of developing extended and consistent CDRs. However, solving the electromagnetic problem of the ocean backscattering by means of theoretical models is an extremely complex problem. It requires a full understanding of the mechanisms regulating the relation between the ocean wind and waves, which in turn affects the relation between surface wind and the ocean surface NRCS. It also requires an

accurate physics-based parameterization of such mechanisms and, as such, an accurate parameterization of the ocean surface itself.

It is generally accepted that the mechanism regulating the backscattering from the ocean surface is described by the Bragg resonance theory [Valenzuela, 1978]. However, it is also recognized that the pure Bragg theory does not fully explain all the effects observed on the radar backscatter. An example is the upwind/downwind asymmetry, which shows that the Bragg waves do not equally act on the NRCS for each pair of opposing radar look directions. Advanced models developed in the past have relied on the theory of Bragg scattering mechanism in combination with quasi-specular scattering [Apel *et al*, 1994] and composite surface theories [Valenzuela, 1978]. To mention an example, the model developed by Donelan and Pierson (1987) leads to a good agreement between their model and scatterometer measurements at Ku-band frequency, proving that defining a calibrated theoretical model for the calculation of the ocean backscatter within the framework of the composite surface theory is a feasible approach. However, their formulation was considered quite complex for general applications and not applicable to a wide range of environmental conditions, radar wavelengths, different polarizations and observation geometries [Fois, 2015]. The optimized composite surface model presented by Romeiser and Alpers, (1997) was one of the first attempts to meet all these requirements. Following the approach of Plant (1986), their proposed model was based on an expansion of the NRCS up to second order, including the upwind/downwind asymmetry of the NRCS by hydrodynamic modulation of the Bragg waves by longer waves. An alternative approach to solve the scattering problem of the ocean surface by using composite surface theory was proposed by Plant (2002), with the idea of coupling the new findings in modeling the ocean backscattering to the speed of modern computers, to compute the mean of the ocean backscattering cross section as the ensemble averages over the stochastically rough facets of long wave surface. However, the above-mentioned models do not account for the non-Bragg scattering mechanisms like rain effects [Contreras *et al*., 2003, Contreras *et al*., 2006], breaking wave phenomena [Kundrayvtzev *et al.*, 2003], SST-induced modifications and dependency on air temperature [Bourassa *et al*., 2010(c)], which instead play a significant role in the ocean backscattering. This makes it difficult to obtain consistent descriptions of the NRCS over a large range of radar frequencies, incidence angles, different polarization states as well as in both clear weather and rain conditions, proving that some inconsistencies in theoretical modeling of the ocean backscattering are still unresolved.

With this background in mind, the goal of this research is to improve the theoretical modeling of the ocean scatterometer backscatter, describing the relation between the NRCS and the surface wind speed/direction base on the interaction between the radar signal and the ocean surface waves, in both clear air and rain condition. The objective is to investigate and account for the different sources that the current sensor-specific GMFs are not able to characterize, such as frequency-specific sensor sensitivity to wind, rain effects and different viewing geometries. In particular, this research has revealed the need for new understanding regarding the frequency-dependent surface backscatter modeling in response to the wind-forced surface wave spectrum. It shows the importance of accurately modeling the equilibrium condition of the ocean waves in order to properly represent

the relationship between the NRCS and the ocean surface winds. These new findings allow a new research path to deeply investigate the ocean surface backscattering coefficient towards a fully optimized multi-frequency theoretical model that will combine the surface effects of wind and rain at different frequencies and viewing geometries.

This work is organized as follows: **Chapter II** introduces the theory of the electromagnetic scattering from ocean surface. The theory of the scattering mechanism from natural rough surfaces is described along with the formulation of both scattering models and ocean surface roughness representations. **Chapter III** describes our approach towards an optimized theoretical model. It firstly summarizes the methodology used in order to develop a reliable ocean surface backscattering model in non-rainy conditions. Then, a new configuration of the ocean surface roughness model is presented and a new tuning strategy is explained. Model validation at Ku-band frequency is also performed with both empirical models and observational scatterometer data. Validation at C-band is also shown. **Chapter IV** describes our approach to include the effects of the rain on the ocean surface backscattering coefficient. We have used the model described in Chapter III as background model, which we have then extended to include the dependence of the rain intensity in a theoretical framework. The rain effects are described, along with the modified model of the ocean surface roughness. Validation of the model at Ku-band frequency is performed and a preliminary evaluation using Ku-band SeaWind Scatterometer actual data, in combination with the Advanced Microwave Scanning Radiometer observations, is also shown. Conclusions and future works are given in **Chapter V**.

Chapter II
Ocean Surface Scattering: Theory and Modeling

2.1 Introduction to Natural Rough Surfaces

When an electromagnetic wave impinges upon a boundary surface between two semi-infinite media, part of the incident radiation is scattered into the upper medium, whereas the rest is transmitted into the lower medium. If the lower medium is non-homogeneous, a portion of the transmitted radiation is scattered by the non-homogeneities and it may cross the boundary layer into the upper medium (*volume scattering*). On the other hand, if the two media are homogenous with respect to the wavelength of the electromagnetic radiation, the volume scattering is not induced and the scattering remains only at the boundary surface (*surface scattering*) [Ulaby *et al*., 1982]. The ocean surface scattering is a typical case of surface scattering, as it occurs at the interface between the ocean and the atmosphere, which can be assumed homogeneous media at the scatterometer frequencies.

As a natural surface, the ocean can be studied from a statistical point of view, by employing the theory of scattering from random natural rough surfaces. Such surfaces are characterized by random irregularities and are usually described in terms of statistical parameters, which quantify the deviation of these irregularities from a smooth "reference surface", as depicted in Fig. 2.1. These irregularities are generated by geophysical variables (e.g. the ocean waves generated by surface wind) and they represent the surface *roughness*, which is quantified with respect to the wavelength of the incident radiation. The degree of roughness is extremely important because it regulates the surface backscattered power.
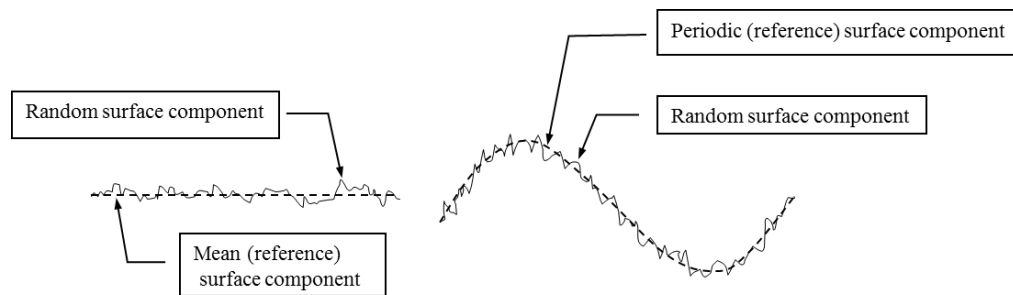
Figure 2.1. Configuration of surface height variation for flat (a) and periodic (b) reference surfaces [credit: Marcantoni D.].

In this section, the statistical parameters generally used to quantify the roughness of natural surfaces are described and the principles of the scattering mechanism are also illustrated. Based on these concepts, several theories have been developed in the past to describe the scattering from the ocean. Such theories along with the corresponding model of the ocean surface backscattering coefficient are explained in Section 2.2. These models

require accurate ocean surface roughness representations, in order to be applicable. The descriptions of the ocean roughness models are illustrated in Section 2.3.

2.1.1 Statistical Properties

In order to understand the meaning of a rough surface and the conditions under which a surface can be considered electromagnetically smooth, two main criteria have been determined in the literature, namely the *Rayleigh* and the *Fraunhofer* criterion [Ulaby *et al*., 1982]. Considering a plane monochromatic wave λ transmitted under an incidence angle θ on a random surface, the phase difference $\Delta\phi$ between two rays reflected by two separated points of the surface is defined as $\Delta\phi = 2h(2\pi/\lambda)\cos\theta$, where h is the standard deviation of the surface height. The *Rayleigh* criterion states that, if $\Delta\phi < \pi/2$, then the surface can be considered as smooth and it is defined by the standard deviation $h < \lambda/8\cos\theta$. The *Fraunhofer* criterion considers a surface as smooth, when $\Delta\phi < \pi/8$ and in turn, the standard deviation becomes $h < \lambda/32\cos\theta$.

Random rough surfaces are described by statistical quantities which essentially define the vertical surface heights spread from the reference surface and the horizontal variation along the surface. By considering $z = z(x, y)$ the random process of the surface heights, the statistical *mean value* is defined as [Ulaby *et al*., 1982]:

$$\overline{z} = \frac{1}{L_x L_y} \int_{-L_x/2}^{L_x/2} \int_{-L_y/2}^{L_y/2} z(x, y)\, dx\, dy\ . \tag{2.1}$$

To determine the mean power of the roughness, it is used the *second order momentum*, which is defined as [Ulaby *et al*., 1982]:

$$\overline{z^2} = \frac{1}{L_x L_y} \int_{-L_x/2}^{L_x/2} \int_{-L_y/2}^{L_y/2} z^2(x, y)\, dx\, dy\ . \tag{2.2}$$

The vertical roughness is generally described by the *standard deviation* σ_{std} (or the corresponding root-mean-square-error), defined as [Ulaby *et al*. 1982]:

$$\sigma_{std} = \sqrt{\frac{1}{L_x L_y} \int_{-L_x/2}^{L_x/2} \int_{-L_y/2}^{L_y/2} (z(x, y) - \overline{z})^2\, dx\, dy}\ . \tag{2.3}$$

On the other hand, to describe the horizontal roughness, the *normalized autocorrelation function $\rho(x')$* is used. For a spatial displacement x' between two points, such function is defined as:

$$\rho(x') = \frac{\int_{-L_x/2}^{L_x/2} z(x)z(x+x')\, dx}{\int_{-L_x/2}^{L_x/2} z^2(x)\, dx}\ , \tag{2.4}$$

where $z(x + x')$ is a point with the spatial displacement from the point x'. The associated quantity is the surface *correlation length* (l), defined as the displacement $x' = l$, such that $\rho(l) = 1/e$ (e: Euler's value ≈ 2.7183). Thus, the correlation length can be interpreted as a quantity describing the horizontal independence of two points on the surface. For smooth surfaces $l = \infty$ [Ulaby *et al*. 1982].

2.1.2 Principles of Surface Scattering Mechanism

The surface roughness regulates the scattering of the incident electromagnetic radiation. When this signal is transmitted upon the boundary surface with incidence angle θ, part of the radiation is reflected while the rest is scattered towards any direction. The rougher the surface, the stronger the scattered component and the smaller the reflected component. A qualitative description of this mechanism is illustrated in Fig. 2.2. For smooth surfaces, Fig. 2.2 (a), the radiation is reflected toward the specular direction, following the Fresnel theory. For slightly-rough surfaces, Fig. 2.2 (b), the radiation is composed by two components: the *coherent component* from the power reflected in the specular direction and the *incoherent component*, which is the power scattered in all directions. As the surface becomes rougher, the specular component becomes negligible so that, in the case of very rough surface, Fig. 2.2 (c), the return power consists only of the incoherent component and the backscattering coefficient varies as $cos^2\theta$.
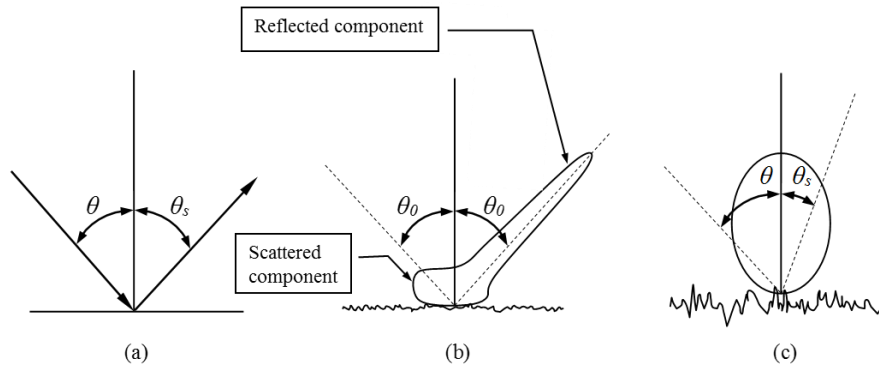
Figure 2.2. Qualitative scheme of the reflected and scattered power component for smooth (a), slightly-rough (b) and very-rough (c) surfaces [credit: Marcantoni D.].

For *monostatic radar*, the return power approaches zero in case of smooth surface, unless the incident angle is close to the normal incidence. This proves that the backscattering coefficient does not only depend on the surface roughness, but it also depends on the radar incident angle. In particular, as the incident angle becomes larger, the backscattering coefficient decreases and for a smooth surface, it decreases more rapidly than for a rough surface. The angular variation of the backscattering coefficient is shown in Fig. 2.3.
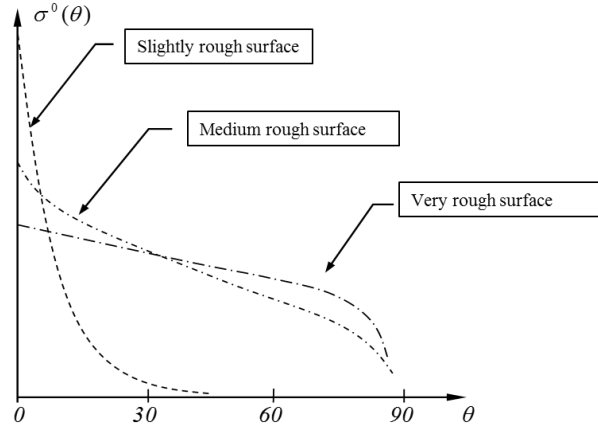
Figure 2.3. Backscattering coefficient trend with respect to the incident angle θ, for different surface roughness degrees [credit: Marcantoni D.].

2.2   Ocean Surface Scattering Models

Past methods based on physical models have been proposed to describe and solve the scattering problem from rough surfaces. However, each model describes the surface scattering mechanism for specific degrees of roughness, so that the corresponding method is applicable only if the characteristics of the surface meet those conditions. The scattering problem of the ocean surface cannot be solved by using only one of these models, since the ocean surface represents a complex rough surface case, where several scales of roughness are superimposed. In this section, the different rough surface scattering models and the corresponding equations of the backscattering coefficient are described. It is also shown how these models are combined in order to obtain a good representation of the ocean surface backscattering coefficient.

2.2.1 Physical Optics

The *physical optics* scattering method, also known as *Kirchhoff approximation*, was widely used to solve scattering problem for surfaces characterized by gentle undulation [Ulaby *et al*., 1982]. To be applicable, this model requires that the horizontal roughness, identified by the correlation length l or the curvature radius ρ_c, is greater than the electromagnetic wavelength λ. The applicability condition of the physical optics was given by Brenhkovskikh (1952), such that $\rho_c k cos^3\theta \gg 1$, with k is the electromagnetic wavenumber and θ the incident angle of the electromagnetic radiation. While this approximation requires a specific condition for horizontal roughness scales, there are not direct restrictions on the vertical roughness. If the correlation length is large enough to preserve acceptable curvature radius, larger surface standard deviation are also tolerated.

In the Kirchhoff approximation, the surface can be approximated as a series of tangent-plane *"facets"* as shown in Fig. 2.4, so that the scattering field at each point of the surface can be computed as the field that would be scattered in presence of a radiation that impinges upon a flat surface.
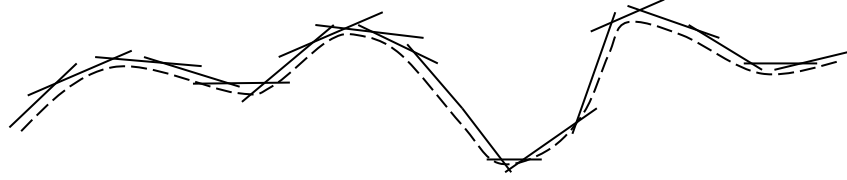
Figure 2.4. Schematic configuration of tangent-plane approximation [Ulaby *et al.*, 1982].

The individual facet can be considered as a single scattering element, whose reradiating pattern depends on the size of the facet with respect to λ. The infinite tangent plane acts as fully specular reflector, whose reradiating patter is described by a Delta function. As the facet size becomes smaller, the reradiating pattern is wider and side lobes appear, but their intensity is lower than the main lobe. The schematic view of the physical optics approximation is shown in Fig. 2.5.
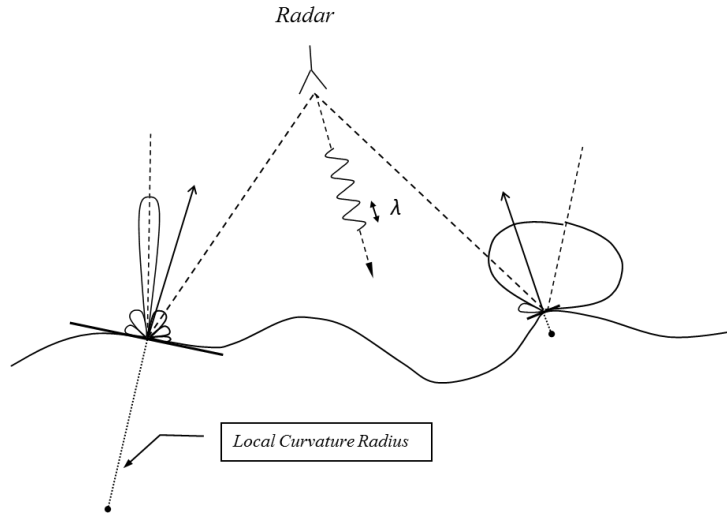
Figure 2.5. Physical optics approximation [credit: Marcantoni D.].

Therefore, the scattered field is locally obtained by specular reflection from the tangent plane to the surface and the electromagnetic far-field is computed as an integral over the entire surface. Under this condition, the surface backscattering coefficient, in *quasi-specular reflection*, is expressed as [Valenzuela, 1978; Ulaby *et al.*, 1982]:

$$\sigma_{sp}^0(\theta) = \frac{|R(0)|^2}{2\sigma_x\sigma_y \cos^4\theta} \exp(-\tan^2\theta/2\sigma_x) \,, \tag{2.5}$$

where $R(0)$ is the Fresnel reflection coefficient, the quantities σ_x and σ_y are the surface slope standard deviation in x and y direction, respectively, and θ the incident angle.

The limitation of this approach is not only established by the roughness of the surface. By being consistent with specular reflection mechanism, for monostatic radar the radiation can only come back for incident angle close to the normal incidence, so that this approximation gives consistent results only for low θ values.

2.2.2 Small Perturbation Method

The scattering from periodic surfaces has been formulated by using the Extended Boundary Condition (EBC) method and solved by the Small Perturbation Method (SPM). The SPM is applicable for *slightly-rough surface* and it is valid when both the correlation length (l) and the standard deviation (σ_{std}) of the surface are small compared to the wavelength of the electromagnetic radiation (with wavenumber k). As shown in Ulaby *et al.*, (1982), these conditions are defined as:

(i) $k\sigma_{std} < 0.3$;
(ii) $\sqrt{2}\sigma_{std}/l < 0.3$.

As mentioned in the previous section, the scattered power from a surface characterized by small-scale roughness is composed by the coherent component due to specular reflection and the incoherent component due to the roughness of the surface. In the SPM theory [Valenzuela, 1978], the total scattered electromagnetic field ($\mathbf{E_s}$, $\mathbf{H_s}$) is expressed as an expanded series, as shown in Eq. (2.6), where the zero-order electromagnetic field ($\mathbf{E}_s^{(0)}$, $\mathbf{H}_s^{(0)}$) is the surface field when the perturbation is absent – that is the flat surface specular component – and the first-order field ($\mathbf{E}_s^{(1)}$, $\mathbf{H}_s^{(1)}$) (and higher) is due to the superimposed small-scale perturbation.

$$\mathbf{E}_s = \mathbf{E}_s^{(0)} + \mathbf{E}_s^{(1)} + \mathbf{E}_s^{(2)} + \cdots \qquad\qquad (2.6\,(a))$$

$$\mathbf{H}_s = \mathbf{H}_s^{(0)} + \mathbf{H}_s^{(1)} + \mathbf{H}_s^{(2)} + \cdots \qquad\qquad (2.6\,(b))$$

As shown by Yueh *et al.* (1988), the EBC/SPM can be used to solve the scattering from randomly perturbed dielectric periodic surface, by assuming the small-scale perturbation as a Gaussian random process and by expanding and solving the scattered field up to the second order. The incoherent backscattering coefficient can be derived from the first-order scattered fields and it is defined as:

$$\sigma_{pq}^0(\theta, \varphi) = 4\pi k^2 \cos^2\theta\, W(2k\sin\theta, \varphi) \left| F_{pq}^{(1)} \right|^2, \qquad\qquad (2.7)$$

17

where $W(\ ,\ )$ is the two-dimensional wavenumber spectral density of the small-scale surface roughness, θ and φ are the incidence and azimuth angles, respectively, $F_{pq}^{(1)}$ represents the first-order scattering coefficient derived by the amplitude of the scattering fields and the indices *p, q* denote the polarization state of the incident and backscattered radiation, respectively. On the other hand, Yueh *et al.* (1994 and 1997), found that the second-order scattered field is coherent and it represents a correction term to the coherent surface reflection coefficient.

2.2.3 Composite-Surface Scattering

The theory of the *composite-surface scattering* was firstly formulated by Wright (1968) for the scattering of the ocean surface. In this model, the ocean surface is assumed as composed by two scales of roughness corresponding to short surface waves superimposed to large waves. The surface is then approximated as an infinite number of slightly-rough patches. The slope of these patches is modified by the underlying long waves in such a way that this *tilting* effect modifies the local plane of incidence of the electromagnetic radiation impinging upon the small-scale patch, Fig. 2.6.
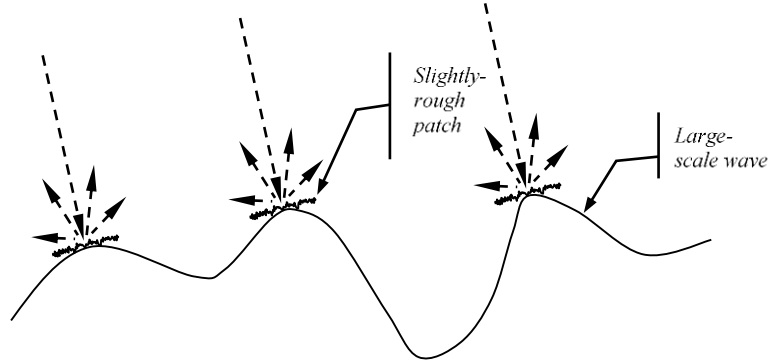
Figure 2.6. Representation of the ocean surface as described by composite-surface theory [credit: Marcantoni D.].

Therefore, the backscattered power – incoherent component – is defined as an average of the power from a single patch, over the distribution of the slope of the long waves. Accordingly, the ocean surface backscattering coefficient σ^0, for the small-scale roughness component, is obtained as the integral of the radiation from the single slightly-rough patch, Eq. (2.7), (hereafter as $\sigma_{pq}^{0(sl)}$), weighted by the probability density function of the long waves slopes $P(S_x, S_y)$, where S_x and S_y represent the surface slopes in the x and y directions, respectively. The total backscattering coefficient is defined as [Valenzuela, 1978]:

$$\sigma_{pq}^0(\theta, \varphi) = \int_{-\infty}^{+\infty} dS_y' \int_{-\infty}^{+\infty} dS_x' \sigma_{pq}^{0(sl)}(\theta, \varphi) P(S_x, S_y) \ . \tag{2.8}$$

2.2.4 Two-Scale Model

It has been recognized that the long waves of the ocean surface meet the applicability condition of the physical optics, so that by combining the *Kirchhoff approximation* with the *composite-surface model*, one can obtain a good approximation of the ocean surface backscattering coefficient that accounts for both long and short waves. Such model is known as *Two-Scale Model* of the ocean surface scattering [Wright, 1968; Valenzela, 1978; Durden and Vesecky 1985] and it can be defined as:

$$\sigma_{pq}^0(\theta, \varphi) = \sigma_{pq}^{0(0)}(\theta, \varphi) + \sigma_{pq}^{0(1)}(\theta, \varphi) \,, \tag{2.9}$$

where $\sigma_{pq}^{0(0)}$ represents the quasi-specular backscattering coefficient for the large-wave component of the ocean surface, obtained by Eq. (2.5), while $\sigma_{pq}^{0(1)}$ represents the contribution from the small-scale waves tilted by the long-wave slope as shown in Eq. (2.8). To be applicable, this model requires the definition of the probability density function $P(S_x, S_y)$ of the long-wave slope. Different studies have been carried out to properly define this function [Cox and Munk, 1954; Fung and Lee, 1982]. In the linear wave theory, which ignores the non-linear effects of ocean waves, the slope distribution of a non-isotropic surface is assumed Gaussian as shown in Eq. (2.10):

$$P\big(S_x, S_y\big) = \frac{1}{2\pi\sigma_u\sigma_c}\exp\left[-\frac{1}{2}\left(\frac{S_x{}^2}{\sigma_u{}^2}\frac{S_y{}^2}{\sigma_c{}^2}\right)\right], \tag{2.10}$$

where the terms σ_u and σ_c represent the variance of the long-wave slope distribution, in upwind – radar observation in the direction of the wind – and in crosswind direction – radar observation normal to the direction of the wind. For higher order approximation, the Gram-Charlier distribution [Cox and Munk, 1954] is used, which accounts for the distribution peakedness and the skewness due to the non-linear wave-wave interactions. However, as pointed out by Liu *et al.*, (1997), the Gram-Charlier distribution is suitable only for slopes that are less than 2.5 times the standard deviation of the surface slope. Therefore, according to Pierdicca and Pulvirenti (2008), a Gaussian slope distribution can be used along with a correction term that accounts for the observed asymmetry between the ocean responses in upwind and downwind directions. This asymmetry is induced by the non-linear hydrodynamic modulation, which causes an increase of the concentration of the small-scale waves on the leeward sides of the longer waves. In Pierdicca and Pulvirenti, (2008) this effect is modelled according to the approach proposed by Yueh *et al.*, (1997), who developed an hydrodynamic modulation function that modulates the spectral density of the small-scale waves.

The two-scale model (TSM) is probably the most widely used method to compute the microwave backscattering coefficient from the ocean surface [Bourlier *et al.*, 2005]. Several studies exist in the literature

that exploit the TSM for studies and analysis of the ocean scattering as well as ocean surface emission [Sobiesky *et al.*, 1991]. This model is easy to apply, however the main issue to derive such model is that it strongly relies on the representation of the ocean surface roughness. The model of the backscattering coefficient $\sigma_{pq}^{0(sl)}$ for slightly rough surfaces, depends on the density power of the surface height W, also known as wave spectrum, which represents a statistical parameterization of the ocean surface. In addition to the possible inaccuracy and uncertainty of the spectrum models, the TSM is based on an arbitrary parameter k_d that divides the small-scale wave component from the large-scale waves of the sea surface and this arbitrariness may represent a critical point. To overcome this problem, other theoretical models for the radar cross section have been developed, such as the small slope approximation (SSA) model proposed by Voronovich and Zavorotny (1994, 2001) and its enhanced version proposed by Fois, (2015) to include also the Doppler signature of the sea surface. However, it has not been completely assessed if one method (SSA/TSM) is superior to the others [Johnson, 2006] and, as also shown in the results of Voronovich and Zavorotny (2001), the 2nd-order SSA and the TSM may lead to similar results for incidence angle greater that 25°, which are those angles mostly used in ocean scatterometry. Furthermore Johnson, (2005) has pointed out that the discrepancies due to uncertainties in the sea surface spectrum model may overcome those due to approximations in any electromagnetic scattering model. Indeed, the work proposed by Pierdicca and Pulvirenti, (2008) demonstrates that, by refining the spectrum model, the TSM is able to represent the ocean backscattering in both C-band and Ku-band radar frequencies. However, such refinements are often derived by either fitting empirical measurements or actual data, limiting the physical reasoning of the theoretical model.

2.3 Modeling the Ocean Surface Roughness

2.3.1 Ocean Surface Wave Spectrum

The privileged formulation to describe the ocean waves is the spectral density of the ocean surface height, known as *ocean surface wave spectrum*, which describes the distribution of the wave energy over the different wave components identified by their wavenumber k (or frequency f). As discussed in the previous section, due to the complicated nature of the ocean surface, the ocean surface can be generally assumed to be composed by two scales of roughness, such as: long waves (characterized by low k-values) and short waves (characterized by high k-values).

The wind-driven short waves are those of major interest in a wide range of studies and defining a reliable statistical description is needed to improve the understanding of the processes characterizing the ocean/atmosphere interface. While the precise knowledge of the short-scale roughness has been considered the

prime requirement, a full representation of the spectrum model is fundamental to represent the ocean scattering, due to the coupling of short and long waves.

The ocean wave spectrum consists of a directional contribution, referred to as the *spreading function* ($\Phi(k,\varphi)$), which accounts for the wind direction (φ) and an omnidirectional *elevation spectrum* ($S(k)$) accounting for the wind speed. The elevation spectrum is related to the corresponding *curvature spectrum* (B(k)) by B(k)=k^4S(k). This quantity is mainly used to represent the ocean surface roughness.

According to the formulation of Durden and Vesecky, (1985), the general spectrum formulation can be written as:

$$W(k,\varphi) = \frac{1}{2\pi k^4} S(k)\Phi(k,\varphi) \ . \tag{2.11}$$

It can be also expressed as the two roughness components, corresponding to higher wavenumbers (h) and lower wavenumbers (l), such that:

$$W(k_x, k_y) = \begin{cases} W_h(k_x, k_y), & k \geq k_d \\ W_l(k_x, k_y), & k < k_d \end{cases}, \tag{2.12}$$

where k_x and k_y are the rectangular components in the wavenumber space, $k = \left(k_x^2 + k_y^2\right)^{1/2}$ and $k_d = k_0/5$ (k_0 is the electromagnetic wavenumber) [Pierdicca and Pulvirenti, 2008].

The wave spectrum comes from the equation describing the evolution of the ocean waves, mainly regulated by three "source" terms [Thomson *et al.*, 2013] such as, wind input (S_{in}), non-linear wave-wave interactions (S_{nl}), and dissipation (S_{dis}), the latter is mostly due to water viscosity, breaking wave phenomena and generation of parasitic capillary waves. The equation of the action-wave spectrum is defined as [Elfouhaily *et al.*, 1997]:

$$\frac{\partial}{\partial t}(\mathcal{A}) + c_g \cdot \nabla(\mathcal{A}) = S_{in} + S_{nl} + S_{dis} \ , \tag{2.13}$$

where $\mathcal{A}(k,\varphi) = c\,W(k,\varphi)$ is the action-spectral density, with c the phase speed and c_g is the group velocity. As postulated by Phillips, (1985), at small-scale roughness range, the wave growth is assumed to be slow and flux divergence to be negligible, so that the left-hand side of Eq. (2.13) is zero. Therefore, the corresponding wave spectrum is in equilibrium, such that the source terms on the right-side of the wave-action equation are equally balanced. This leads to $S_{in} + S_{nl} + S_{dis} = 0$ for small-scale waves, so that, by defining the source/dissipation contribution terms, the short-wave spectrum can be derived.

2.3.2 Overview of Existing Spectrum Models

Based on the wave energy equilibrium concept, several spectrum models have been proposed over the years. A model largely discussed in the literature is the one proposed by Donelan and Pierson, (1987) (hereafter DP). They described the ocean wave spectrum in the whole ocean waves regime, by identifying the short waves as those having wavenumber values k greater than ten times the wavenumber of the spectral peak k_p. Because of their attention to the formulation for the short wave component, this model has been largely used in radar scattering studies. The full curvature omnidirectional spectrum is defined as:

$$B(k)^{DP} = \begin{cases} B(k)_l^{DP} & \text{for } k < 10k_p \\ B(k)_h^{DP} & \text{for } k < 10k_p \end{cases}.$$
(2.14)

The corresponding large wave component is described as:

$$B(k)_l^{DP} = \frac{1}{2}\alpha_p L_{PM} J_p \sqrt{k/k_p},$$
(2.15)

with α_p the long waves equilibrium range parameter defined by Phillip-Kitaigorodskii, L_{PM} the Pierson-Moskowitz shape spectrum and J_p is the peak enhancement factor introduced by Hasselmann *et al.*, (1973). The short wave contribution was derived based on the propagation theory proposed by Hasselmann *et al.*, (1973). It accounts for the equilibrium condition among the surface wave growth induced by the wind $\beta(k)$, the dissipation due to the water viscosity $D(k)$ and the dissipation induced by the wave breaking. By assuming the contribution of the non-linear interactions as negligible, the DP omnidirectional curvature spectrum, for high wavenumber, becomes:

$$B(k)_h^{DP} = \frac{1}{\phi_{max}} \sqrt[n]{\left|\frac{\beta(k)-D(k)}{\alpha\omega}\right|},$$
(2.16)

where α is a function of k, ϕ_{max} is the maximum of the applied spreading function and ω the radian frequency.

Generally, the spreading function accounts for the asymmetry $\Delta(k)$ between the upwind ($\varphi = 0°$) and the crosswind ($\varphi = 90°$) directions and in turn, it changes according to the definition of $\Delta(k)$ as expressed in Eq. (2.17):

$$\Phi(k,\varphi) = [1 + \Delta(k)\cos 2\varphi],$$
(2.17)

so that the upwind/crosswind ratio is defined as $\Delta(k) = \left(\Phi(k,0) - \Phi\left(k,\frac{\pi}{2}\right)\right) \Big/ \left(\Phi(k,0) + \Phi\left(k,\frac{\pi}{2}\right)\right)$.

For the DP spectrum, the spreading function is based on the previous work of Donelan *et al.*, (1985) and it is defined as an hyperbolic secant, whose argument depends on a continuous function $h = h(k/k_p)$, so that the upwind/crosswind asymmetry is defined as:

$$\Delta(k)^{DP} = \frac{1-\text{sech}(h\pi/2)}{1+\text{sech}(h\pi/2)} . \tag{2.18}$$

The above omnidirectional and directional spectrum formulations are expressed as shown in Elfouhaily *et al.*, (1997). For details the reader can refer to that paper.

One of the most used spectrum models for ocean applications is the spectrum proposed by Elfouhaily *et al.*, (1997) (hereafter E). They proposed a unified omnidirectional curvature spectrum $B(k)$, in equilibrium condition and for a fully developed sea, as the sum of the contributions from the long waves $B(k)_l$ and short waves $B(k)_h$, such that:

$$B(k)^E = B(k)_l^{\ E} + B(k)_h^{\ E} . \tag{2.19}$$

The two components are defined as:

$$B(k)_l^{\ E} = \frac{1}{2}\alpha_p\left(c_p/c\right)F_p , \tag{2.20}$$

$$B(k)_h^{\ E} = \frac{1}{2}\alpha_m(c_m/c)F_m , \tag{2.21}$$

where α_p and α_m are the generalized equilibrium range parameters defined by Phillip-Kitaigorodskii for long and short waves, respectively. α_p is dependent on the dimensionless inverse wave age $\Omega \approx U_{10}/c_p$, with U_{10} the surface wind speed at 10 m height and c_p the phase speed at the long waves spectral peak $k_p = \Omega^2(g/U_{10})$. For fully developed sea, the Ω value is known to be close to 0.84. By being c the wave phase speed, depending on the ocean wave wavenumber k and defined as $c = c(k) = \sqrt{g(k_m^2 + k^2)/(k \cdot k_m^2)}$, then the phase speed c_p is defined as $c_p = c(k_p)$. α_m is dependent on the dimensionless parameter (u_*/c_m), where $c_m = c(k_m) = 0.23$ m/s is the phase speed calculated at the short waves secondary peak $k_m = 370$ rad/m and u_* is the friction velocity (discussions about the α_m parameter are given in Chapter III). u_* is related to the surface wind speed, at any elevation z and for the roughness length Z_0, through the following equation $U(z) = (u_*/0.4)\ln(z/Z_0)$ [Yueh *et al.*, 1994]. F_p and F_m are the cutoff factors concentrating the energy at the long and short ocean waves ranges, defined in Eq. (32) and Eq. (41) of Elfouhaily *et al.*, (1997), respectively.

The corresponding spreading function is described as a hyperbolic tangent, such that the upwind/crosswind ratio is defined as:

$$\Delta(k)^E = \tanh\left\{\alpha_0 + \alpha_p^E (c/c_p)^{2.5} + \alpha_m^E (c_m/c)^{2.5}\right\}, \tag{2.22}$$

where $\alpha_0 = \ln(2)/4$, whereas α_p^E and α_m^E are function of U_{10}/c_p and u_*/c_m, respectively. These parameters differ from the corresponding one in the omnidirectional component and they are defined in the E spectrum as $\alpha_p^E = 4$ and $\alpha_m^E = 0.13\, u_*/c_m$. The advantage of the E spectrum model is that its form is relatively simple and it can be easily applied. However, the spectrum model was developed only from in situ or tank measurements, without the use of any radar data, so that adjustments are needed for radar applications. This will be discussed in Chapter III.

A wave spectrum that proved to give good results in radar applications is the model described by Pierdicca and Pulvirenti, (2008) (hereafter PP). They combined the omnidirectional contribution proposed by Durden and Vesecky, (1985) with the spreading function described by Elfouhaily. They performed an extensive comparison between simulations of the ocean surface backscattering/emission and the empirical geophysical model functions at both C and Ku-band radar frequencies and they proposed a modified spectrum for both the omnidirectional and directional components. Their new omnidirectional spectrum in both long and short waves' regimes is summarized as:

$$B(k)^{PP} = \begin{cases} 0.007 \exp\left\{-0.74\left[\left(g/U_{19.5}^2\right)/k\right]^2\right\}, \text{ for } k < 3 \\ 0.007(1.25ku_*{}^\beta/g_*)^{0.225\log(k/3)}, \quad \text{for } k \geq 3 \end{cases}, \tag{2.23}$$

where β and g_* are tuned functions, whose explicit formulations can be found in Eq. (19) and Eq. (22) of Pierdicca and Pulvirenti, (2008). The parameter g is the gravitational acceleration and $U_{19.5}$ is the wind speed at 19.5 m above the mean ocean surface.

The spreading function is a modification of the E model so that the upwind/crosswind asymmetry is still a hyperbolic tangent with the same form of the E model, but the argument has been tuned such that:

$$\Delta(k)^{PP} = \tanh\{g_1{}^{PP} + \alpha_m{}^{PP}(c_m{}^{PP}/c)^q\}. \tag{2.24}$$

The function $c_m{}^{PP}$ is expressed as $c_m{}^{PP} = c\left(k_m{}^{PP}\right) = \sqrt{2g/k_m{}^{PP}}$, where $k_m{}^{PP}$ was tuned to fit the GMFs as well as $g_1{}^{PP}$, q and $\alpha_m{}^{PP}$, which are all functions of the friction velocity u_*. To develop their model, Pierdicca and Pulvirenti, (2008) adopted the relation between u_* and the surface wind speed as defined in Yueh *et al.*, (1994). The complete formulations of these parameters are described in the corresponding paper by Eq.

(13), Eq. (12), Eq. (14), Eq. (15), respectively. This spectrum is the result of a tuning approach at C and Ku-band frequencies and it yields a fairly good agreement with the GMFs' data for both active and passive measurements. It also proves that the disagreement between empirical and theoretical ocean backscattering models may be ascribed to poor ocean surface roughness representation.

Comparisons between the DP, E and PP omnidirectional components $B(k)$ as well as the corresponding directional $\Delta(k)$ functions are shown in Fig. 2.7 and Fig. 2.8 respectively, at three different wind speeds (5 m/s, 10 m/s and 15 m/s). In general, the representation of $\Delta(k)^{DP}$ is quite challenging due to the difficulties in properly defining the $h = h(k/k_p)$ function. Several expressions are available in the literature [Donelan and Pierson, 1987; Jelenak *et al.*, 1998; Plant, 2002] and they all describe *h* as a continuous function composed by a different equation for each *k*-range. However, the transition between these *k*-ranges is not always smooth, causing discontinuity in $\Delta(k)^{DP}$. The function $\Delta(k)^{DP}$ is illustrated in Fig. 2.8 by assuming the *h* function as proposed by Plant, (2002). Despite the use of a patching function to combine long and short wave spectra, a discontinuity is seen around $k = 300$ rad/m, due to the discontinuity in the definition of *h*.

In addition to these models, many attempts have been made in the past to derive accurate representations of the surface wave spectrum (e.g. Durden and Vesecky, 1985; Donelan *et al.*, 1985; Apel, 1994; Kundryavtsev *et al.*, 1999, 2003; Plant, 2002; Hwang *et al.*, 2013). All these spectrum descriptions differ from each other, since they are based on different analysis, investigations and interpretations performed by the different authors. While these studies have advanced the knowledge in this field, a variety of parameters need to be accounted for and the physical mechanisms/factors that regulate the ocean waves are still not fully understood, so that a "standard" formulation is still under investigation.
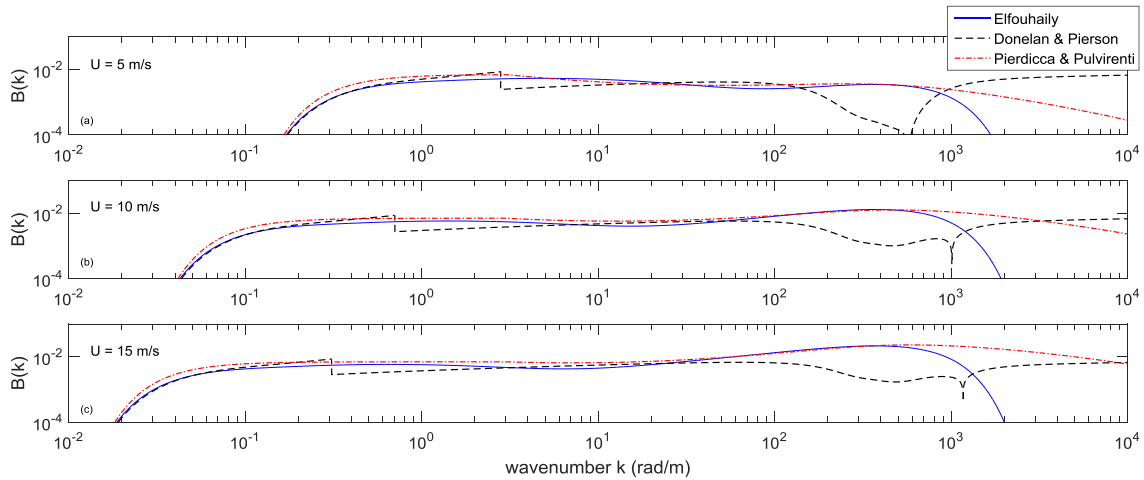
Figure 2.7. Omnidirectional component of the ocean surface wave spectrum for wind speed of 5m/s (a), 10 m/s (b) and 15 m/s (c). Comparisons between the model proposed by Elfouhaily *et al.*, (1997) (solid-blue), Donelan and Pierson, 1987 (dashed-black) and Pierdicca and Pulvirenti, (2008) (dotted-dashed-red) are shown.
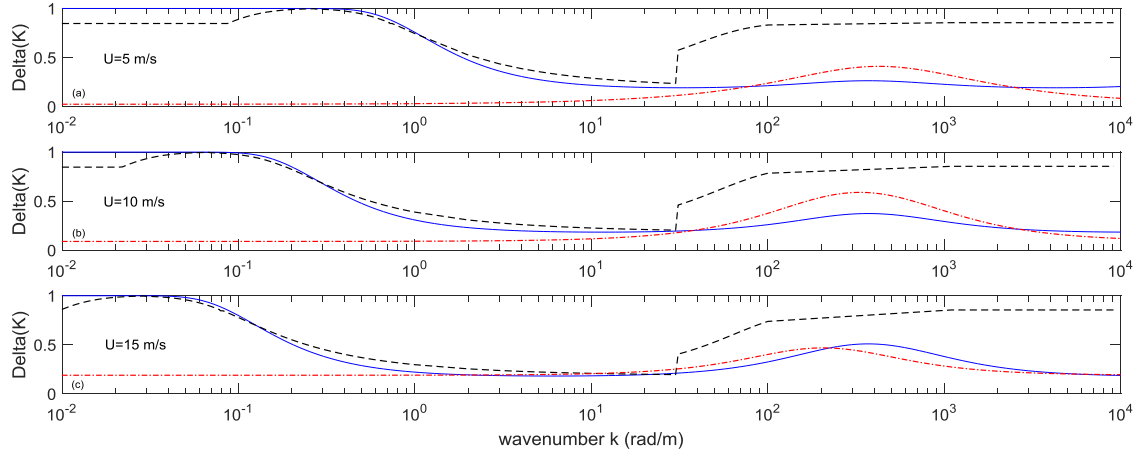
Figure 2.8. Directional component of the ocean surface wave spectrum ($\Delta(k)$) for wind speed of 5 m/s (a), 10 m/s (b) and 15 m/s (c). Comparisons between the model proposed by Elfouhaily *et al*., (1997) (solid-blue), Donelan and Pierson, 1987 (dashed-black) and Pierdicca and Pulvirenti, (2008) (dotted-dashed-red) are shown.

Chapter 3

Towards an Optimized Theoretical Model in Clear Air

3.1   Problem Overview

As mentioned in the Introduction, wind vectors are retrieved by inversion techniques of geophysical model functions describing the relationship between the backscattered signal and the wind parameters. Such relation is defined on empirical basis by correlating the scatterometer observations with numerical weather models as well as with other measurements used as truth [Hersbach *et al*., 2007; Verhoef *et al*., 2008]. However, the empirical GMFs may fail in properly representing the backscattered signal in particular weather circumstances, such as in extreme wind events and rain conditions [Soisuvarn *et al.*, 2013; Ricciardulli *et al*., 2015]. The rain effects have been largely discussed in the literature [Contreras *et al*., 2003; Draper and Long, 2004; Tang *et al*., 2013], and several semi-empirical techniques have been already developed to address the rain impact on scatterometer wind retrievals [Weissman *et al*., 2012], but a theoretical model describing the scatterometer backscattering coefficient in presence of wind and rain is still an open issue. Such model would represent a valuable contribution for several applications such as: studying the rain signature on the scatterometer observations, analyzing the uncertainty of the wind retrievals due to the rain and further providing the opportunity to jointly estimate wind and rain. However, in order to accurately combine the effects of wind and rain, the first main step is the development of a reliable multi-frequency theoretical model in presence of wind only. Such multi-frequency model is needed by the scientific community not only for rain applications. Over the past decade, the Ocean Wind Vector Science Team (OWVST) has reached high confidence in the existing empirical model functions and wind vector estimations, so that the exploitation of reliable theoretically-derived simulations allows for a full understanding of the observations' physics as well as of the differences seen in the ocean surface winds retrieved by scatterometers operating at different frequencies. The inconsistencies among the wind retrievals obtained by different scatterometers may have important implications in the development of consistent ocean wind climate data records.

However the main issue in deriving such model is the definition of an accurate representation of the ocean wind wave spectrum, allowing the model to work at different radar frequencies. We have analyzed some of the most frequently used models available but, once they are ingested in the electromagnetic model of the surface backscattering, they appear not capable of accurately reproducing the existing GMFs. For this reason, the main effort of this work has been focused on the definition of an accurate representation of the ocean wave spectrum with the aim of properly modeling the ocean surface backscattering coefficient at different frequencies. To do that, we have first identified the spectrum parameters that have major influence on the surface backscattering coefficient and we have then derived a new configuration of these parameters by avoiding any fitting approach

of empirical values that could restrict the model to work only for a particular condition or frequency. In this work, we have focused on the vertical polarization (V pol.) only, since we are not considering the non-Bragg scattering mechanisms that mainly affect the horizontal polarization (H pol.) [Kudryavtsev *et al.*, 2003; Fois, 2015]. To model the vertical polarization, we have analyzed the C-band and Ku-band frequencies. Comparisons between the proposed theoretical model of the ocean response and existing empirical model functions demonstrate that this new proposed spectrum yields a remarkable agreement at Ku-band along with a good agreement at C-band. The different level of agreement between these two frequencies is mainly due to the different sensitivity to the wind. The empirical model functions clearly show that the ocean responses obtained at C-band and Ku-band have a different modulation with the wind speed as well as with the wind direction. Such diversity cannot be modeled with the standard numerical formulation of the well-known theoretical models. Therefore, in this work an inter-comparison between the two frequencies is also performed, with the aim of showing the limitation of the numerical formulation along with the proposed corrections to improve the theoretical model in identifying this different sensitivity, which is essential to define a multi-frequency model.

3.2   Methodology

To model the ocean surface backscattering coefficient we have decided to rely on the Two-Scale Model, as described in Section 2.2.4. Over the past twenty years, other theoretical models of the radar cross section have been extensively developed [Voronovich and Zavorotny, 2001; Plant, 2002; Fois, 2015], but we have decided to rely on the TSM since it has proved to be able to fairly reproduce the ocean response once the ocean surface roughness is well represented [Pierdicca and Pulvirenti, 2008]. The modeled backscattering coefficient accounts for the contribution of specular reflection (coherent component) of the incident radiation from the plane facets locally approximating the long wave, as well as the contribution of the backscattered radiation (incoherent component) from the small scale waves. The latter is the main contribution at incidence angle higher than 30° and it is described in terms of the Bragg resonance mechanism [Valenzuela, 1978]. We have also accounted for the effects of the hydrodynamic modulation (described in Section 2.2.4) as suggested by Pierdicca and Pulvirenti, (2008). We have assumed a Gaussian distribution of the surface slopes, but we have included the observed upwind/downwind asymmetry through a function that modulates the spectrum of the small-scale waves. Details of the numerical formulation of hydrodynamic modulation can be found in Eq. (17) and Eq. (18) of Pierdicca and Pulvirenti, (2008).

To model the ocean surface roughness, we have examined three models available in the literature as the benchmark of our analysis, based on the fact that these expressions are all suitable to be modified to include the rain effects. Rain mostly affects the short waves, therefore it is essential to have a clear separation between the spectrum formulations of the short and the long wave ranges to properly introduce the rain-induced

modifications. We have started from the model proposed by Donelan and Pierson, (1987) (hereafter DP) which proposed an omnidirectional spectrum as a function of the ocean wavenumber. As described by Eq. (2.14) the formulation of the long and short waves is separated by the wavenumber of the spectral peak k_p such that the contribution of the short waves corresponds to wavenumbers higher than 10 times k_p and the contribution of long waves corresponds to wavenumbers up to 10 times k_p. Another formulation is given by Pierdicca and Pulvirenti (hereafter PP), as shown by Eq. (2.23) and (2.24). Their results show that the proposed spectrum model has a good impact on the backscattering models especially in the directional contribution. For our analysis, the other used formulation is given by Elfouhaily *et al.* (1997) (hereafter E), who derived a unified law by assuming the omnidirectional spectrum as the sum of the two roughness components, Eq. (2.19). However, several studies have demonstrated that their directional component, Eq. (2.22), is not suitable to model the backscattering coefficient. Voronovich and Zavoronotny, (2001) as well as Voronovich *et al.*, (2000) have found that the directional part of the E spectrum overestimates the spectral density of shorter waves, introducing an inconsistency on the backscattering coefficient in the crosswind direction. In addition, Bourlier and Berginc, (2002) have included a correction term in the equation of the omnidirectional short wave spectrum due to an anomaly in the results when trying to replicate the E spectrum. Since we have experienced these same anomalies, in our analysis a preliminary tuned E model (hereafter Et model) has been used rather than the E model and it accounts for the modification introduced by Bourlier and Berginc as well as the modified directional contribution proposed by Pierdicca and Pulvirenti. With this modification, the Et and PP models share the same spreading function, but they differ in the omnidirectional component.

The ocean surface backscattering coefficient has been simulated by using the SEAWIND2 software, where the TSM is implemented [Pierdicca and Pulvirenti, 2008]. We have adjusted this software in order to include the DP spectrum model (TSM-DP), the Et model (TSM-Et) as well as the PP model (TSM-PP) and the results have been compared to the Ku-band and C-band GMFs. In particular, at Ku-band we have used the GMF from the SeaWinds instrument on board the Ku-band NASA QuikSCAT scatterometer. Such GMF has been kindly provided by NASA-*Jet Propulsion Laboratory*. At QuikSCAT incidence angles, this GMF corresponds to the Ku-2011 GMF developed by *Remote Sensing Systems* (RSS), using 10 years QuikSCAT backscatter measurements, whereas, to extend the GMF to a wide range of incidence angles, the NASA Scatterometer (NSCAT) dataset was used [Ricciardulli and Wentz, 2015]. At C-band, the CMOD5.n GMF developed for the C-band scatterometers onboard the ERS satellite [Hersbach , 2008] has been used. The validation has been also performed by using the Ku-band SeaWinds scatterometer data collected from the ADvanced Earth Observation Satellite-II (ADEOS-II), during 2003.

The impact of the different spectrum models have been firstly studied by analyzing the Ku-band NRCS ($\sigma°$) derived in upwind ($\varphi = 0°$) and crosswind ($\varphi = 90°$) directions (where φ indicates the direction of the wind). These values have been computed for incidence angles of 54° and 46°, in order to be consistent with the angle used by the QuikSCAT scatterometer for vertical and horizontal polarization, respectively. We have

firstly investigated the H polarization. Compared to the GMF, the TSM NRCS shows a bias which does not depend on the representation of the ocean wave spectrum. The TSM-PP, TSM-Et and TSM-DP show the same trend, which consists in a bias, with respect to the GMF, that increases with the wind speed as shown in Fig. 3.0. As previously mention, it is known that the H polarization is also sensitive to scattering mechanisms, which do not considerably affect the V polarization, like steep breaking waves. These waves specularly reflect the incident radiation, resulting in an additional contribution to the ocean surface backscattered power. Thus, the observed bias can be ascribed to the fact that we are not accounting for these non-Bragg scattering contributions at this stage, so that the H polarization would not be properly modeled. For this reason, we have decided to focus on the V polarization only. Modeling the H pol. will be the goal of future investigations.
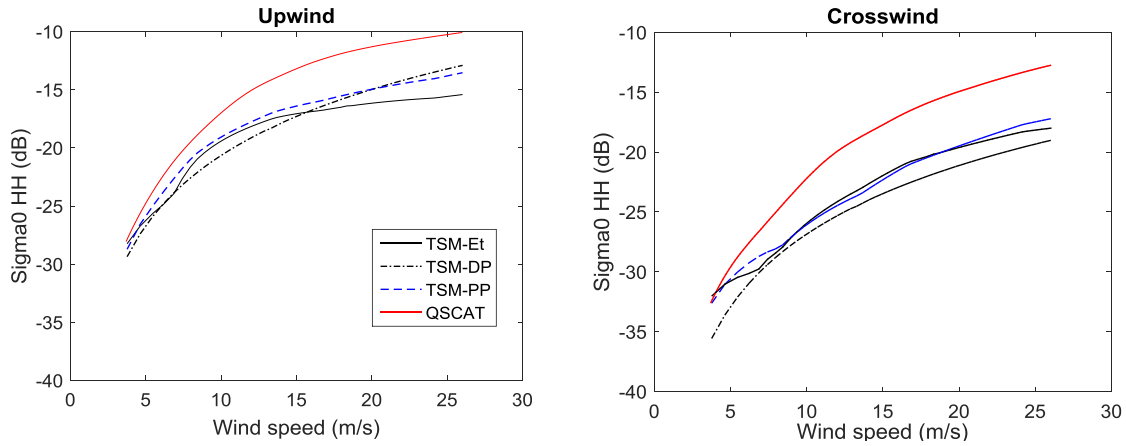
Figure 3.0. Ku-band horizontally polarized σ^0 (Sigma0) in upwind (left) and crosswind (right) direction at at $\theta = 46°$. Comparisons between the modeled σ^0 including the tuned Elfohuaily (TSM-Et) (solid back), Pierdicca and Pulvirenti (TSM-PP) (dashed blue) and Donelan and Pierson (TSM-DP) (dashed black) spectrum models are shown. The QuikSCAT (QSCAT) GMFs (solid red) is used for validation.

For vertical polarization, comparisons among TSM-DP, TSM-E and TSM-PP have been performed as well as among TSM-DP, TSM-Et and TSM-PP in order to verify the effect of the modified spreading function in the E model. As shown in Fig. 3.1, the DP spectrum has demonstrated to underestimate $\sigma°$ in crosswind direction and the disagreement with the QSCAT GMF is the worst amongst the other models. In addition, compared to the E model, the Et model gives a better agreement at both upwind and crosswind directions. Therefore, based on these results, we have decided to not use the DP model as a reference and to use the Et model rather than the directional E spectrum formulations.
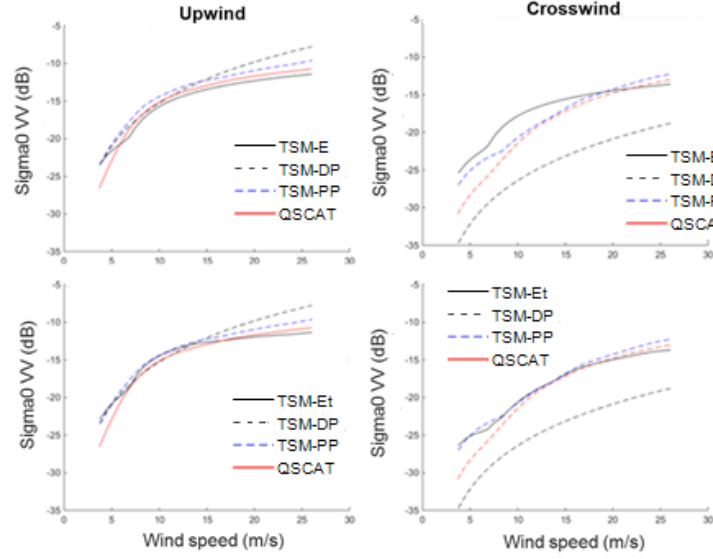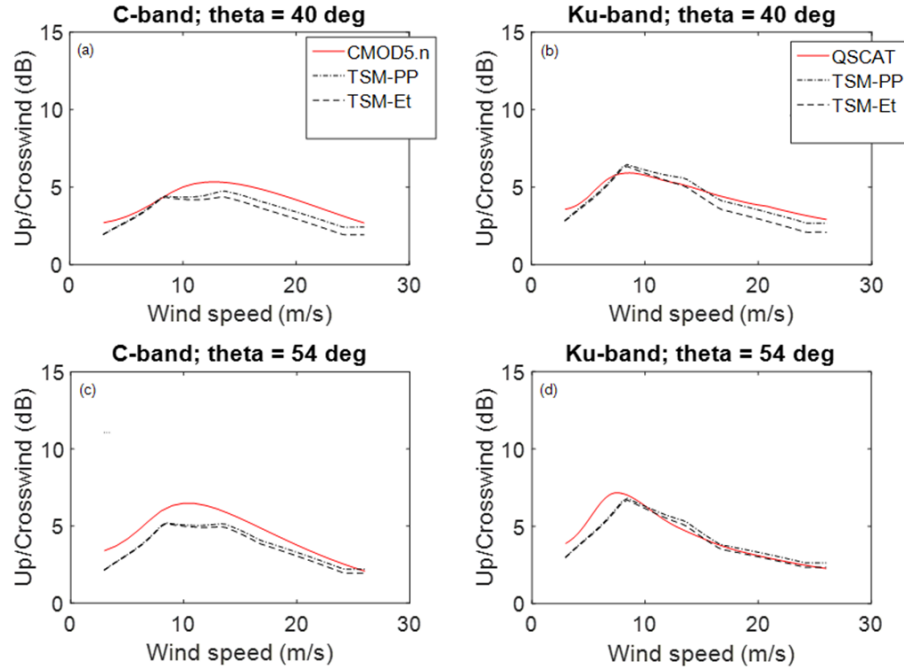
Figure 3.1. Ku-band σ^0 in upwind (left) and crosswind (right) directions versus wind speed at $\theta = 54°$. Top: comparisons amongst Elfohuaily (TSM-E, solid-black), Donelan and Pierson (TSM-DP, dashed-black) and Pierdicca and Pulvirenti (TSM-PP, dashed-blue) spectrum models. Bottom: same as before but with the tuned Elfohuaily (TSM-Et) rather than the original E spectrum. QuikSCAT GMF (QSCAT, red) is used for validation.

The most appropriate spectrum between Et and PP has been selected by analyzing the ratio between the ocean surface backscattering coefficients in upwind and crosswind directions. This ratio has been computed at both Ku-band and C-band, for two incidence angles, 40° and 54°. We have decided to focus on these two incidence angles starting from an analysis at Ku-band. Since we have focused on V pol. only, we have decided to use 40° rather than 46° (used for H pol) in order to not overlap the two polarizations. These two angles have been also chosen according to the results shown in Pierdicca and Pulvirenti, (2008), with the aim of testing the validity of our adapted software by reproducing their results at both C- and Ku-band (not shown here). The results are shown in Fig. 3.2. Both the Et and PP spectra are able to reproduce the shape of the GMF by showing that the used spreading function is able to predict the asymmetry between the ocean responses in upwind and crosswind directions, whatever is the definition of the omnidirectional component. However, both models show discrepancies with the GMFs with respect to the wind speed. In particular, at 54°, the Ku-band upwind/crosswind asymmetry is underestimated at low winds, whereas at C-band the same behavior occurs across all wind speed ranges. At 40°, the Ku-band is slightly underestimated at higher winds and this is especially evident in C-band. These differences over the wind speed ranges can be attributed to the representation of the omnidirectional component, which contains most of the sensitivity to the wind speed.

Then, the selection between the Et and the PP models has been based on the formulations of their omnidirectional spectrum. We have therefore concluded that a more consistent approach to correct the spectrum-based disagreement between the TSM and the GMF is to identify and correct the parameters of a spectrum not already modified to match the GMFs. Since the PP model is the result of a tuned omnidirectional

contribution, whose TSM-GMF disagreement is comparable to the one seen when using the Et model, we have decided to rely on the Et model, whose omnidirectional component is based directly on the Elfouhaily spectrum.

Figure 3.2. C-band (right) and Ku-band (left) σ⁰ ratio between upwind and crosswind directions versus wind speed at $\theta = 40°$ (a-b) and $\theta = 54°$ (c-d), for Pierdicca and Pulvirenti (TSM-PP) spectrum (dashed-dotted black), tuned Elfohuaily spectrum (TSM-E$_t$) (dashed black) and Donelan and Pierson (TSM-DP) spectrum (dotted black). QuikSCAT (QSCAT) and CMOD5.n GMFs (red solid) are used for validation at Ku-band and C-band, respectively.

3.3 New Spectrum Model

3.3.1 Background Model Description

The Et wind wave spectrum relies on the E spectrum as presented in Section 2.3.1 with a modified directional component described in Eq. (2.24) as proposed by Pierdicca and Pulvirenti.

As shown by Eq. (2.19), the complete omnidirectional component of the E spectrum is expressed as the sum of the contributions of short waves $B(k)_h{}^E$ (higher wavenumbers) and long waves $B(k)_l{}^E$ (low wavenumbers) whose formulation is given in Eq. (3.1) and Eq. (3.2), respectively:

$$B(k)_l{}^E = \frac{1}{2}\alpha_p\big(c_p/c\big)F_p \,, \tag{3.1}$$

$$B(k)_h{}^E = \left[\frac{1}{2}\alpha_m(c_m/c)F_m\right]\left\{\exp\left[-1.25(k_p/k)^2\right]\right\}, \tag{3.2}$$

where α_p and α_m are the generalized equilibrium range parameters defined by Phillip-Kitaigorodskii for long and short waves, respectively. The parameter $c_m = 0.23$ m/s is the phase speed calculated at the short waves secondary peak $k_m = 370$ rad/m as suggested by Elfouhaily. F_p and F_m are the cutoff factors concentrating the energy at the long and short ocean waves ranges defined in Eq. (32) and Eq. (41) of Elfouhaily *et al.*, (1997), respectively. As previously mentioned, $B(k)_h{}^E$ accounts for an additional term, shown in the right side of Eq. (3.2), as stated in Bourlier and Berginc. c_p is the phase speed calculated at the long waves spectral peak $k_p = \Omega^2(g/ws_{10})$ with the inverse wave age $\Omega = 0.84$ valid for a fully developed sea and ws_{10} is the surface wind speed at 10 m height. We have assumed a fully developed sea, which means that the wind blows for long time over a long distance with constant speed and direction such that the ocean surface equilibrium state is reached. In this situation, the ocean wave spectrum is entirely related to the wind vector only. Although such assumption does not represent the general case of open ocean, the wind vector alone is sufficient to represent the spectrum of wind-generated waves [Lemaire *et al.*, 1999]. Generally, the wind energy is assumed as instantaneously transferred to small-scale waves through friction stresses, so that the wave spectrum at high wavenumber is only related to the local wind friction velocity. Therefore, since wind-generated waves are those directly involved in the ocean response, as first approximation we have accounted for the wind effect only in the wave spectrum. The impact of other parameters (like wind action time, wave age and fetch) is left for future investigations.

At higher incidence angles the incoherent component is the main contribution of the backscattering coefficient and it strongly depends on the spectrum of the short waves, therefore, in this work, we have focused on properly modifying the spectrum $B(k)_h{}^E$ to correct the disagreement shown in Fig. 3.2, with respect to the wind speed. $B(k)_h{}^E$ depends on the wind speed through the equilibrium range parameter α_m, which is defined as a two-range logarithmic law in the original formulation of the Elfouhaily model, as described in Eq. (3.3) according to Eq. (44) of Elfouaily *et al.*, (1997):

$$\alpha_{m\_log} = 10^{-2}\begin{cases} 1 + \ln(u^*/c_m) & \text{for } u^* \leq c_m \\ 1 + 3\ln(u^*/c_m) & \text{for } u^* > c_m \end{cases}. \tag{3.3}$$

Therefore, the TSM-σ^0 sensitivity to the surface wind speed (ws) is mostly driven by this parameter, so that to understand the relation between the σ^0 sensitivity and α_m, we have compared the trend (σ^0 vs. ws) to the trend (α_{m_log} vs. ws). For very low winds α_{m_log} is negative, leading to erroneous results. Thus, being $c_m = 0.23$ m/s, α_{m_log} is valid for u^* higher than 0.085 m/s. We have then performed the analysis by starting from $u^* = 0.11$ m/s, corresponding to wind speed of 3 m/s. Fig. 3.3 shows the TSM-Et azimuthally-averaged σ^0 at 40° (TSM-Et-40) and 54° (TSM-Et-54) versus the wind speed, compared to α_{m_log} trend (am_log).
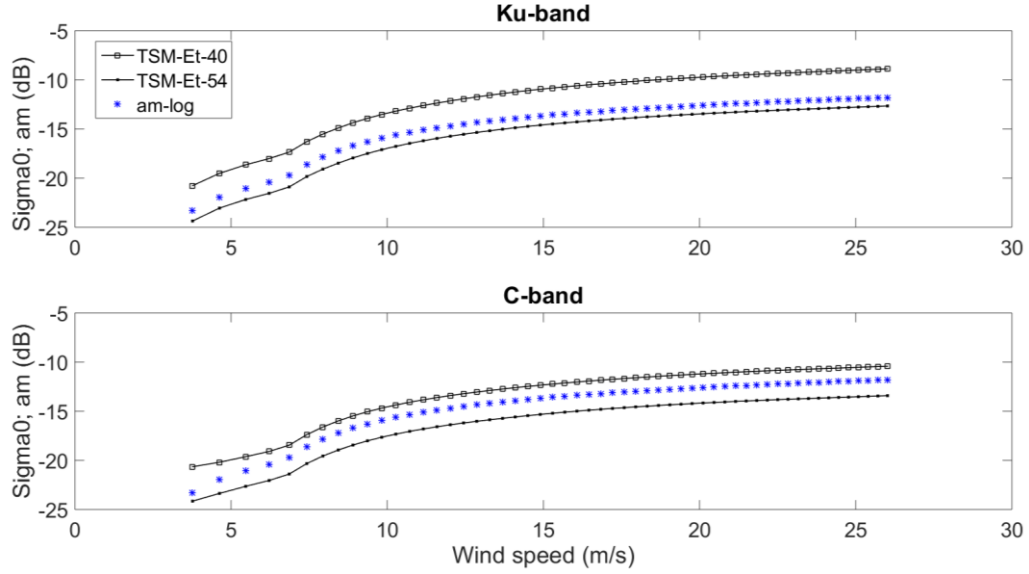
Figure 3.3. Ku-band (top) and C-band (bottom) azimuthally-averaged σ⁰ (Sigma0) modeled by TSM-Et at $\theta = 40°$ (TSM-Et-40/solid-square black) and $\theta = 54°$ (TSM-Et-54/solid-dotted black). The σ⁰ average at upwind, crosswind, and downwind directions is computed. The σ⁰ trend is compared to the trend of the short wave spectrum equilibrium range parameter α_m, described as a two-range logarithmic function of the wind speed in the Et model (am-log/star blue).

The σ^0 mean values have been calculated by averaging the σ^0 in upwind, crosswind and downwind directions. It is possible to notice that at both frequencies as well as both incidence angles, the TSM-Et has the same trend of α_{m_log}. Moreover both the TSM-Et-40 and TSM-Et-54 show a discontinuity around 7 m/s, corresponding to $u^* = c_m$ where the α_{m_log} limit between low and high wind speed regimes is set, according to Eq. (3.3). This confirms the strength of the impact of the equilibrium range parameter on σ^0 and it also reveals that any modification on this parameter will be reflected on σ^0 itself. Therefore, in order to properly correct the disagreement between the TSM-Et and the GMFs in all wind regimes, it is necessary to properly modify the equilibrium range parameter. This can be physically explained by considering α_m as a parameterization of the equilibrium condition among non-linear wave-wave interactions, wind forcing and water viscosity. In steady state regime, this equilibrium conditions drives the relationship between surface wind and small-scale waves, and in turn it plays an important role in the definition of the ocean surface response σ^0.

3.3.2 A New Tuning Strategy

The main goal of our tuning strategy, is to modify the ocean surface wind wave spectrum such that the TSM is able to reproduce the ocean response at all wind regimes and directions for different frequencies.
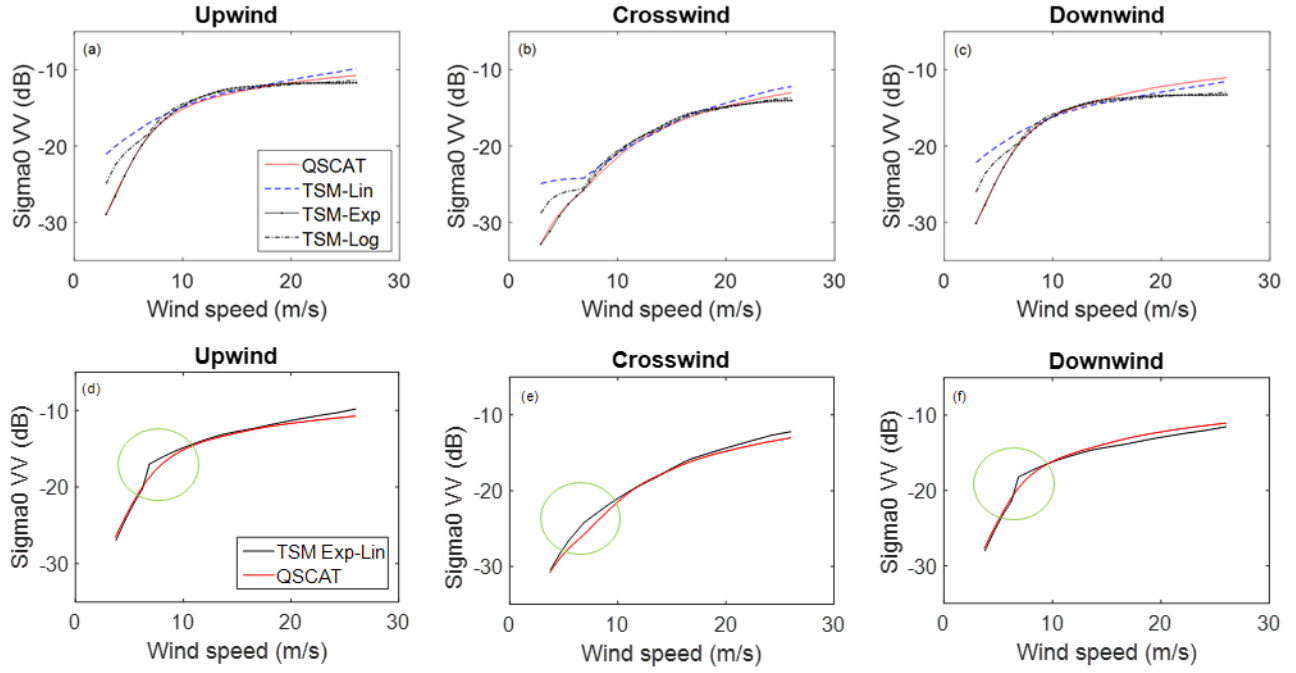
Figure 3.4. Ku-band upwind (a-d), crosswind (b-e) and downwind (c-f) co-polar σ^0 (Sigma0) at vertical polarization for $\theta = 54°$, versus wind speed. Top: the TSM-Et for the linear equilibrium range parameter α_{m_lin} (TSM-Lin, dashed blue), the exponential α_{m_exp} (TSM-Exp, solid-dotted black) and the logarithmic α_{m_log} (TSM-Log, dashed-dotted black) are compared. The QuikSCAT GMF (QSCAT, solid red) is used for comparison. Bottom: TSM with the two-range exponential-linear equilibrium range parameter (TSM Exp-Lin, solid black) is compared to QSCAT GMF. The green circle highlights the discrepancy around 7 m/s due to the two-range law.

For this reason, we have avoided using any empirical parameters or defining any empirical relation which may restrict the model applicability. To properly model the equilibrium range parameter, we have started by analyzing the formulations available in the literature. For this parameter, three different relations are described in Elfouhaily *et al.*, (1997), a linear law with the friction velocity (here as α_{m_lin}), their proposed two-regime logarithmic trend described in Eq. (3.3) and an exponential law (here as α_{m_exp}). The latter is derived by the curvature spectrum level computed at a secondary peak of $k_m = 750$ rad/m, as proposed by Apel, (1994). In particular, we have derived α_{m_exp} by assuming the Elfouhaily curvature spectrum level, computed at a secondary peak of $k_m = 370$ rad/m, equal to the value proposed by Apel, (1994) as presented in Eq. (20) of Elfouhaily *et al.*, (1997). We have decided to keep a secondary peak as proposed by Elfouhaily since they explained that, in the frequency domain, this secondary peak is observed at 31 Hz, but such frequency value is not related to the wavenumber by simply inverting the dispersion relation, as presented by Apel, (1994). This simple conversion does not lead the frequency spectrum and the wavenumber spectrum to preserve the total energy, so that the derivative of the group velocity has to be involved. For this reason, they placed the secondary spectral peak at 370 rad/m rather than 750 rad/m. Eqns. (3.4) and (3.5) describe α_{m_exp} and α_{m_lin} respectively, the latter is defined as presented in (43) of Elfouhaily *et al.*, (1997):

$$\alpha_{m\_exp} = 2 \cdot 10^{\{-4.95+3.45[1-\exp(-ws_{10}/4.7)]\}} , \tag{3.4}$$

$$\alpha_{m\_lin} = 0.014\, u^*/c_m , \tag{3.5}$$

where ws_{10} is the wind speed at 10 m above the surface.

To properly choose the equation to be included in the omnidirectional spectrum, three different simulated trends of the backscattering coefficient have been compared to the GMF: the TSM when the linear α_{m_lin} is included (TSM-lin), the TSM with the exponential α_{m_exp} (TSM-exp) and finally, the TSM with the two-range logarithmic α_{m_log} (TSM-log). The simulations have been performed for the whole wind speed range in upwind, crosswind and downwind directions. The results are shown in Fig. 3.4 (a-c) and they represent the Ku-band backscattering coefficient at incidence angle of 54°. The comparison shows that the TSM-log is in good agreement at higher winds, but it shows major disagreements with the GMF at lower winds. Moreover, as previously discussed, it is also characterized by a discontinuity around 7 m/s, due to the two-range law regulating α_{m_log}. On the other hand, the TSM-exp agrees to the GMF at low winds, whereas TSM-lin agrees at higher winds. Therefore, we have decided to replace the logarithmic expression with the exponential trend at low winds and the linear trend at higher winds. However, this new two-range exponential-linear expression still shows a discontinuity around 7 m/s as highlighted by the green circle in Fig. 3.4 (d-f). This suggests that a two-range function does not match the GMF behavior. Therefore, we propose a unified law, as described in Eq. (3.6), where the two wind regimes are patched together by a new function of the friction velocity $h = h(u^*)$ described in Eq. (3.7). The constant $u_0^* = 0.11$ m/s is used as starting value.

$$\alpha_{m\_NEW} = (1 - h)\alpha_{m\_exp} + h\alpha_{m\_lin} , \tag{3.6}$$

$$h(u^*) = \tanh(u^* - u_0^*) . \tag{3.7}$$

To summarize, here we propose a spectrum model (hereafter "New") relying on the Et spectrum, whose equilibrium range parameter in the short waves' omnidirectional component is replaced with α_{m_NEW}. The results of the new omnidirectional spectrum model (not shown here) computed at different wind speeds from 3 m/s to 21 m/s do not show significant difference with the Elfouhaily model (Fig. 8 of Elfouhaily *et al.*, (1997)). However, even small modifications in the spectrum have a direct and significant impact on the ocean surface backscattering coefficient due to its direct proportionality, especially when the contribution of long waves is negligible. The modification of the equilibrium range parameter represents a more suitable formulation to describe the interaction between surface waves and wind speed, so that the sensitivity of the ocean surface backscattering coefficient can be properly modeled.

3.4   Validation at Ku-band

3.4.1 Comparison Using Empirical Model

The TSM with our new spectrum (TSM-New) has been validated at Ku-band at $\theta = 40°$ and $\theta = 54°$. The dependency of TSM-New to the wind speed has been tested by computing the ocean surface backscattering coefficient at wind speeds ranging between 4 m/s to 25 m/s. Figure 3.5 illustrates that TSM-New is in agreement with the QSCAT GMF over the entire wind speed range and it also improves the disagreement shown by TSM-Et and TSM-PP at winds speeds lower than 10 m/s. It is also worth noticing that, compared to TSM-Et, the proposed TSM-New smoothes the inconsistency of the backscattering coefficient at 7 m/s, proving that the proposed unified α_{m_NEW} law, expressed in Eq. (3.6) corrects such behavior. Figure 3.6 shows the dependency of TSM-New on the wind direction at 4 m/s, 10 m/s and 16 m/s covering the range of low, medium and high winds, respectively. As expected, at low winds the agreement between TSM-New and GMF is significantly improved, compared to TSM-Et and TSM-PP, due to the exponential contribution in the equilibrium range parameter, whereas the directional trend is slightly improved since the spectrum models share the same spreading function. It is worth noticing that at $\theta = 54°$ the TSM-New is extremely close to the GMF. This is particularly important since this incidence angle represents an operational angle of the SeaWinds scatterometer. This demonstrates the validity of the proposed correction of the equilibrium range parameter and it also allows us to make comparisons with actual data.
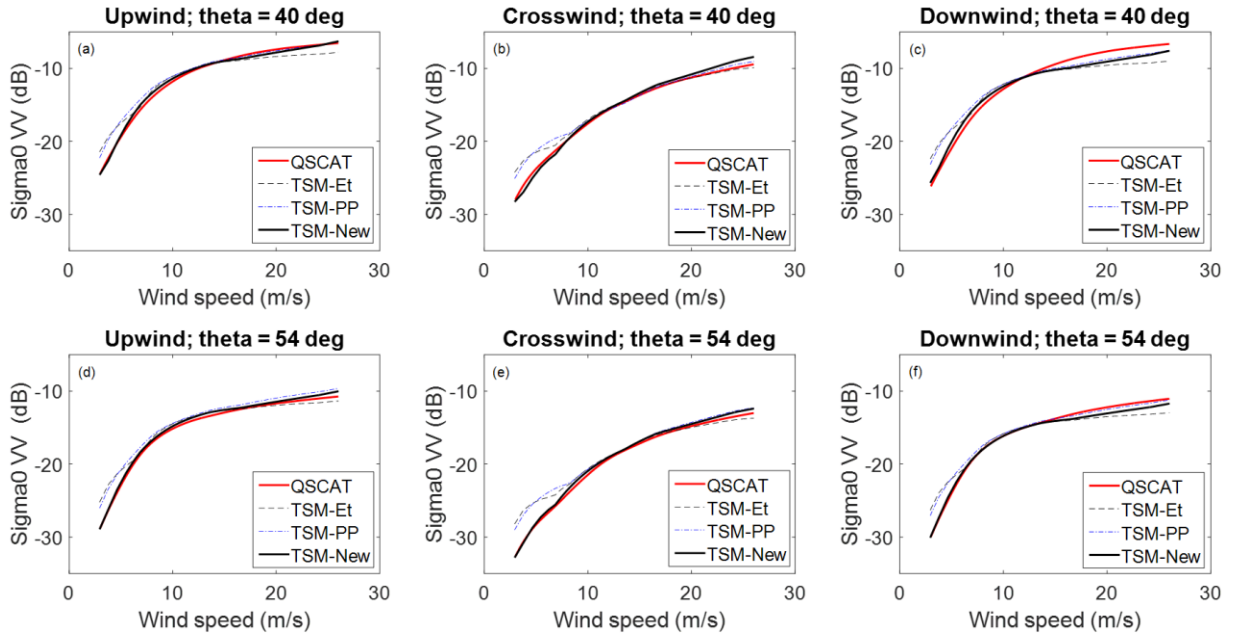

Figure 3.5. Ku-band co-polar σ^0 (Sigma0) at $\theta = 40°$ (a-c) and $\theta = 54°$ (d-f), for upwind (left), crosswind (middle), and downwind (right) versus wind speed. TSM-New (solid black) results are compared to the TSM-Et (dashed black), the TSM-PP (dashed-dotted blue) and QuikSCAT (QSCAT) GMF (solid red).
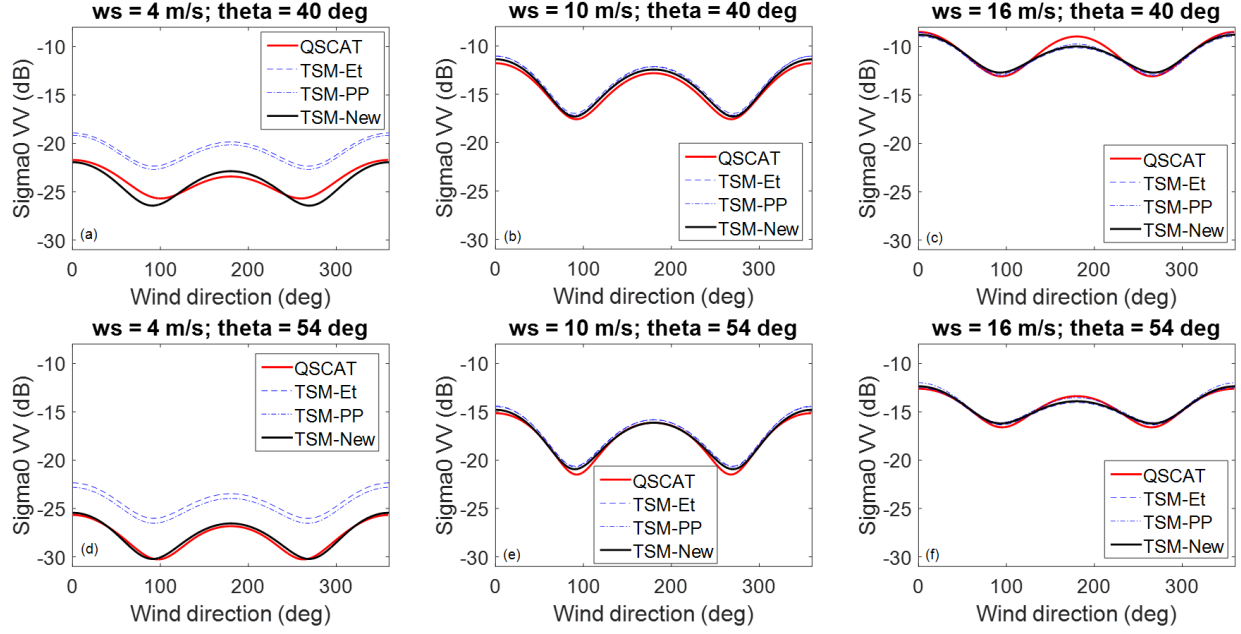
Figure 3.6. Ku-band co-polar σ^0 (Sigma0) at $\theta = 40°$ (a-c) and $\theta = 54°$ (d-f), for 4 m/s (left), 10 m/s (middle), and 16 m/s (right) versus wind direction. TSM-New (solid black) results are compared to the TSM-Et (dashed blue), the TSM-PP (dashed-dotted blue) and QuikSCAT (QSCAT) GMF (solid red).

3.4.2 Comparison Using Actual Data

The validation using the GMF shows a remarkable agreement but it has been performed by analyzing only particular wind regimes (low, medium and high winds) and wind directions (upwind, downwind and crosswind), so that it does not take into account wind conditions outside these ranges. The validation performed with actual data allows us to test the model in a large variety of real wind combinations and also to directly account for the observation geometries with the look and the azimuth angles. Here, we refer to the data from the SeaWinds scatterometer operating at 13.4 GHz, collecting global ocean surface wind vectors. Starting from the SeaWinds onboard QuikSCAT launched on June 19th, 1999 to quickly recover the loss of data from the NASA Scatterometer (NSCAT) in 1997, it was followed by the SeaWinds instrument onboard ADEOS-II, which was launched on December 14th, 2002 and it operated until October 2003. The ADEOS-II mission carried both SeaWinds and AMSR allowing for the simultaneous observation of near-surface winds and rain conditions. SeaWinds uses a rotating dish antenna with two beams: the H pol inner beam with an incidence angle of 46° and the V pol outer beams with an incidence angle of 54°. Each beam has fore and aft looking directions in order to ensure azimuthal diversity.
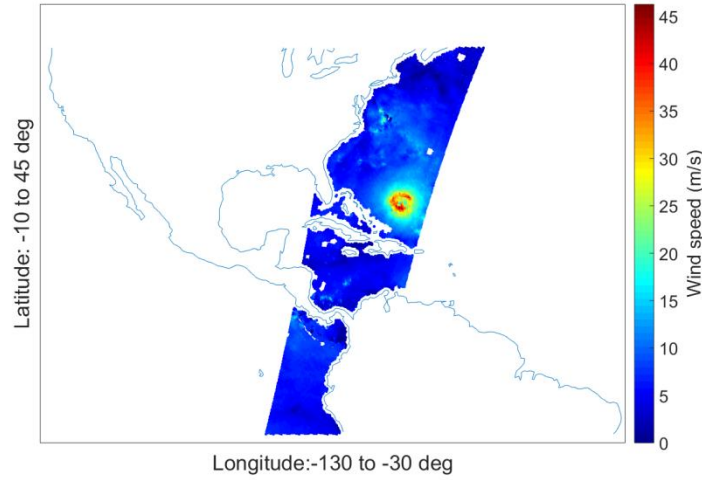
Figure 3.7. Wind speed field as measured by SeaWinds scatterometer on-board ADEOS-II satellite. The Hurricane Isabel on September 2003 presented as the area of very high wind (yellow to red area) is shown. The obit displayed refers to orbit n. 3927 corresponding to Sept. 15th 2003.

We have exploited the ADEOS-II dataset since it also carries the rain measurements, which will be used in the second part of this work (Chapter IV). At this stage, we have focused on the SeaWinds rain-free data only. Here, we refer to the case study of the Hurricane Isabel, which was one of the strongest hurricanes occurred in 2003 during the Atlantic Ocean hurricane season. It formed on September 6th near Cape Verde Island and it reached its highest intensity between September 11th and September 14th after which it started weakening. Data from two different processing levels, called L2A and L2B, have been used in this analysis, corresponding to the measured σ^0 and the retrieved wind speeds/directions, respectively. The data are organized as 25 km × 25 km wind vector cells (WVC) such that 72 WVCs across-track cover the full swath. The WVCs with latitude ranging between 20° to 33° and longitude between 275° to 330° have been selected, corresponding to the area around the cyclone. The L2B wind speeds and directions have been used to compute the TSM-New-simulated σ^0 (σ^0_s) to be compared with the corresponding SeaWinds-measured σ^0 (σ^0_m). To select the wind direction, we have used the solutions processed by the Directional Interval Retrieval (DIR) algorithm, which is used to enhance the solution obtained by the ambiguity removal algorithm [Stiles *et al*., 2002]. We have analyzed the orbit number 3927 and 3941 corresponding to September 15th from 1429 to 1611 UTC and September 16th from 1404 to 1545 UTC, respectively. The data from the first orbit are shown in Fig. 3.7. For each orbit, we have selected those data from the outer beam (V pol), characterized by acceptable signal-to-noise ratio and acquired in the operating wind observation mode. Data over land and data affected by rain have been discarded. This selection has been achieved by using the corresponding data flags available in the wind data products [Dunbar *et al*., 2006].
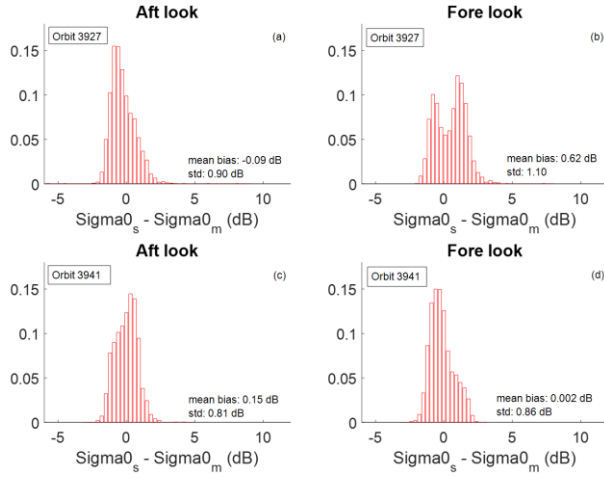
Figure 3.8. Normalized histogram of the difference between σ^0 simulated by the TSM-New (Sigma0$_s$) and σ^0 measured by the SeaWinds scatterometer on-board ADEOS-II satellite (Sigma0$_m$). The orbits n. 3927 (a-b) and n. 3941 (c-d) are shown, along with the aft look (left) and fore look (right).The corresponding values of the mean bias and standard deviation are illustrated.
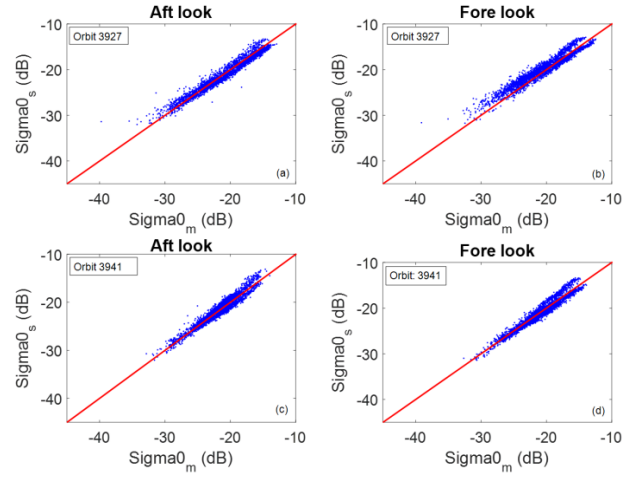
Figure 3.9. Scatterplot between σ^0 simulated by the TSM-New (Sigma0$_s$) and σ^0 measured by the SeaWinds scatterometer on-board ADEOS-II satellite (Sigma0$_m$). The orbits n. 3927 (a-b) and n. 3941 (c-d) are shown, along with the aft look (left) and fore look (right).

The retrieved wind speed ranges between 3 m/s to 22 m/s and the wind directions cover the entire range between 0° to 360°. Figure 3.8, shows the normalized histograms of the difference between σ^0_s (Sigma0$_s$) and σ^0_m (Sigma0$_m$), with the corresponding mean bias and standard deviation, for both orbits and both viewing geometries. The results show that TSM-New is able to reproduce the actual data in rain-free conditions. Both the processed orbits show a very good agreement between SeaWinds and the proposed model. The mean bias range between -0.09 dB and 0.6 dB with a standard deviation between 0.9 dB and 1 dB. The good agreement is also shown by the scatterplot depicted in Fig. 3.9. Very good correspondence can be seen between σ^0_s and the σ^0_m with a slight overestimation of the model for the fore look. This confirms that with this more realistic wind scenario, where also different observation geometries are directly accounted for, the agreement with the proposed model is still very good. However, the spread of the distributions shown in Fig. 3.8 is slightly higher compared to the SeaWinds backscatter accuracy, which is ~0.2 dB [Spencer *et al*., 2000]. This can be justified as we are referring here to two separated orbits and this may cause an increase of the mean standard deviation of each distribution, due to the limited points per orbit. We expect that, by combining more obits together, the distribution spread decreases.

3.5 Validation at C-band

3.5.1 Analysis of the Upwind/Crosswind Asymmetry

The validation at C-band has been performed at incidence angles of 40° and 54° in order to be consistent with the angles used above, at Ku-band. This allows us to consistently analyze the differences between the two frequencies. In Figure 3.10, the C-band σ^0 trend, with respect to the wind direction, is shown as Fig. 3.6.

An overall agreement in terms of wind speed is shown at medium-high wind regimes, using TSM-New. Main discrepancies at 54° at 10 m/s are present and they are due to an overestimation in crosswind direction, which compromises the whole wind direction range. At 4 m/s the TSM-Et model seems to better match the GMF, but as shown in Fig. 3.11, where σ^0 azimuthally-averaged has been computed to account for the wind sensitivity, the TSM-Et does not match the σ^0 trend for increasing wind speeds. The TSM-Et overlaps the GMF at 4 m/s and this explains why there is a perfect agreement at that wind speed, but the overall trend is not consistent with the one shown by the GMF, since it still shows an inconsistency at 7 m/s due to the two-range logarithmic equilibrium parameter. It also saturates at wind speeds much lower than the CMOD5.n and this causes a bias of about 2 dB at higher winds. The TSM-New instead, slightly better agrees with the GMF trend, especially for wind speeds higher than 8 m/s, but in both the wind speed sensitivity and directional modulation, the agreement in Ku-band is much better than the C-band case.
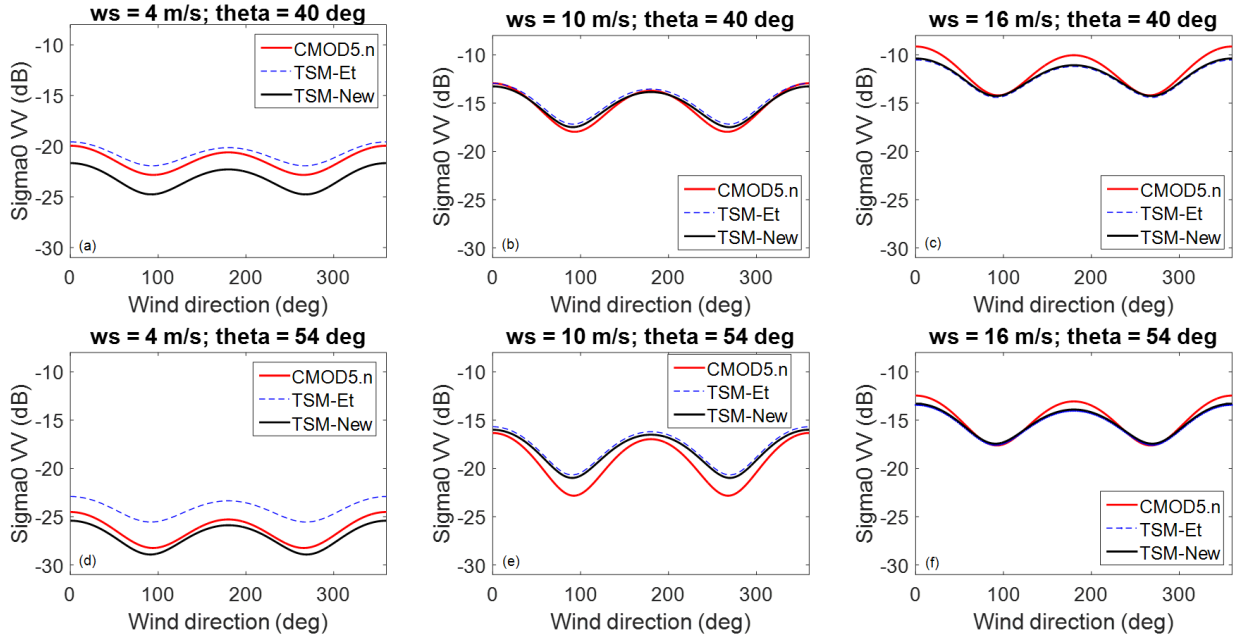
Figure 3.10. C-band V pol σ^0 (Sigma0) at $\theta = 40°$ (a-c) and $\theta = 54°$ (d-f), for 4 m/s (left), 10 m/s (middle), and 16 m/s (right) versus wind direction. TSM-New (solid black) results are compared to the TSM-Et (dashed blue), and the CMOD5.n GMF (solid red).
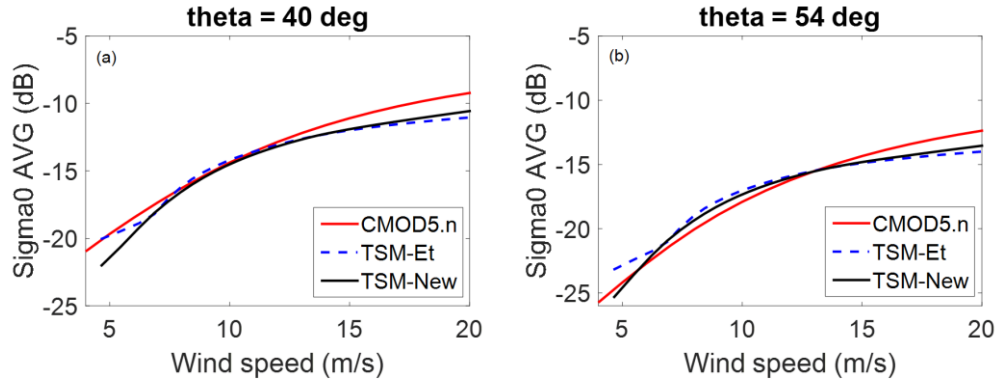
Figure 3.11. C-band azimuthally-averaged σ^0 (Sigma0 AVG) modeled by TSM-New (solid black), TSM-Et (dashed blue) and the C-band CMOD5.n GMF (solid red), for $\theta = 40°$ (a) and $\theta = 54°$ (b).

Two main results arise from our analysis at C-band: At medium-high winds the TSM shows that the modulation with the wind direction is underestimated and in addition to that, the TSM does not perfectly represent the sensitivity to the wind speed as predicted by the CMOD5.n. These results can be handled by making an inter-comparison between the Ku-band and the C-band frequencies. In this sub-section we address the discrepancies in the directional modulation, the issue with the sensitivity to the wind speed is addressed in the next sub-section.

In order to analyze the behavior of the upwind/crosswind asymmetry, we have focused on the σ^0 at wind speeds of 12 m/s, 14 m/s and 16 m/s and incidence angle of 54° because, as shown in Fig. 3.11, in these cases the C-band TSM-σ^0 is almost equal to the GMF. In this way, the possible discrepancies seen with respect to the wind direction, will not be compromised by a disagreement due to the wind speed, i.e. to the omnidirectional component of the spectrum. We have focused on a shorter wind directions range, that is between $\varphi = 0°$ and $\varphi = 180°$, with the aim of analyzing only the upwind/crosswind asymmetry. In Figure 3.12, the three σ^0 trends as predicted by the C-band GMF are compared to the trends obtained with the Ku-band GMF. The results are then compared to the corresponding σ^0 trends modeled by TSM-New$_C$ and TSM-New$_{Ku}$ for C-band and Ku-band, respectively. The two GMFs clearly show that the upwind/crosswind asymmetry behave differently. To quantify this diversity, we have computed the difference between $\sigma^0(\varphi = 0°)$ and $\sigma^0(\varphi = 90°)$ using the GMFs. At C-band the asymmetry is about 1.2 dB higher than at Ku-band. On the other hand, by looking at the results of the TSM, the TSM-New$_C$ σ^0 has almost the same trend of the TSM-New$_{Ku}$ σ^0 between $\varphi = 0°$ and $\varphi = 90°$, therefore, it is clear that the modeled upwind/crosswind asymmetry is not able to describe the difference predicted by the GMFs. The values of the asymmetry modeled by $\Delta(k)^{PP}$, as shown in Eq. (2.24), match the Ku-band case, but they underestimate the C-band, therefore some modifications need to be included such that they do not change the Ku-band but they increase the asymmetry in C-band. Therefore, we have decided to modify Eq. (2.24) such that the C-band Bragg wavenumbers are placed around the spectral peak k_m of the directional component. This has been performed by reducing the k_m values – it defines c_m as $c_m =$

$c(k_m)$ in Eq. (2.24) – by a scaling factor $\alpha = k_{ku}^0/k^0$ representing the ratio between the radar wavenumbers at Ku-band (k_{ku}^0) and C-band (k_0). This scaling factor has been defined such that it represents the deviation between the radar frequency (or radar wavenumber) at C-band and Ku-band. The latter is used here as a reference, due to the good agreement obtained with the GMF. Therefore, such ratio is equal to 2.53 at C-band, whereas it is equal to 1 when the radar frequency corresponds to the Ku-band. Such modification also leads to modification of the contribution of the long waves term g_1 in Eq. (2.24), which has been increased of the same factor. Hence, the new formulations to account for this parameterization are $k_m' = \frac{1}{\alpha}k_m$ and $g_1' = \alpha(g_1)$, respectively. By applying this correction, the contribution computed at C-band Bragg wavenumbers becomes higher with respect to the previous case, without modifying the Ku-band case. The results with the modified spreading function are shown in Fig 3.12 in TSM-New$_C$-sp ("sp" indicates the inclusion of the new parameterizations in the spreading function). As expected, the modeled asymmetry has been increased and it better fits the GMF trend at C-band, especially at 14 m/s. Although this correction is not intended as a final configuration of the spectrum, it suggests two new features, which the shape of the upwind/crosswind asymmetry has to account for to better match both frequencies: $\Delta(k)^{PP}$ needs to have higher values in the C-band Bragg wavenumber range, and the increasing values for $\Delta(k)^{PP}$ should be related to the values of the deviation between the two frequencies.

This analysis also proves that to develop a multi-frequency theoretical model, the diversity in the radar sensitivity to the wind direction must be accounted for and this sensitivity is mostly enclosed in the upwind/crosswind asymmetry.
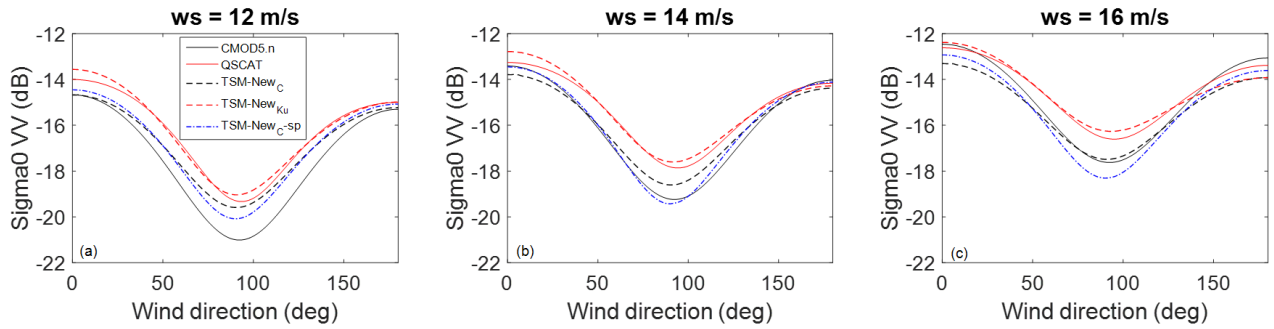
Figure 3.12. Comparison between the C-band (black) and Ku-band (red) σ^0 versus wind direction ranging between $\varphi = 0°$ and $\varphi = 180°$, at $\theta = 54°$, for 12 m/s (a), 14 m/s (b) and 16 m/s (c). The C-band (CMOD5.n) GMF (solid black) upwind/crosswind asymmetry is about 1.2 dB higher than the Ku-band QuikSCAT (QSCAT) GMFs (solid red). The corresponding TSM-New$_C$ (dashed black) and TSM-New$_{Ku}$ (dashed red) have almost the same asymmetry. TSM-New$_C$-sp (dashed-dotted blue) accounts for an enhanced asymmetry at C-band, without changing the Ku-band, considering a spreading function modified accordingly.

3.5.2 Analysis of the Sensitivity to Wind Speed

As shown in Fig. 3.13 for 40° and 54° incidence, by comparing the σ^0 azimuthally-averaged at C-band and Ku-band as predicted by the GMFs, it is clear that at wind speeds ranging between 4 m/s to 8 m/s, the Ku-band increases more rapidly with the wind speed, proving that the C-band is less sensitive to the wind speed in this wind range. Looking at the sensitivity shown by the proposed TSM-New, at both frequencies it clearly follows the wind speed trend of the α_m equilibrium range parameter as previously discussed. However, the α_m trend proves to perfectly match the predicted Ku-band sensitivity, but it does not fit that of C-band. Indeed, the TSM-New-C tends to follow the Ku-band GMF, especially at wind speeds lower that 10 m/s.
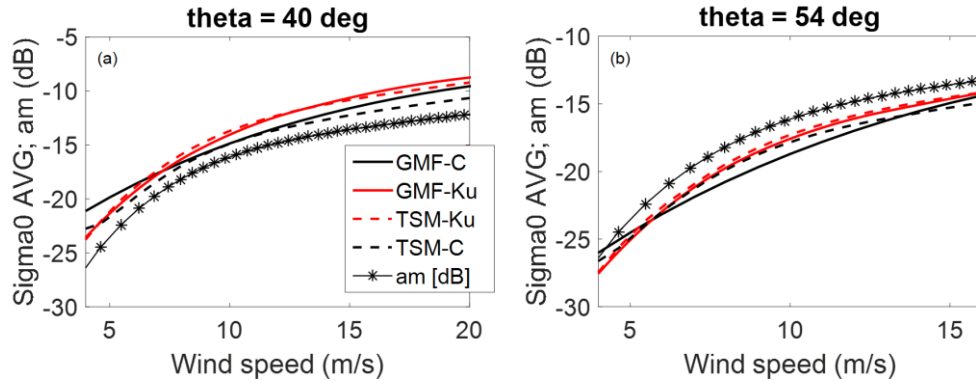
Figure 3.13. C-band (black) and Ku-band (red) azimuthally-averaged σ^0 (Sigma0) as predicted by the corresponding GMFs (solid) and modeled by TSM-New (dashed) at $\theta = 40°$ (a) and $\theta = 54°$ (b). The average of σ^0 at upwind, crosswind, and downwind directions is computed. The equilibrium range parameter α_{m_NEW} values (am) versus the wind speed are also shown (solid star) as proof of its influence in the TSM model.

The diversity predicted by the GMFs can be physically justified by taking into account the effects of the non-linear wave-wave interactions. As discussed by Fois *et al.*, (2015), these non-linear interactions have a strong impact on the ocean backscattering. The modulation induced by longer waves may change the statistics of the short wave components and in turn their interaction with the wind. Therefore, it is reasonable to assume that, if the interaction with the wind changes amongst the short wave components (specifically the Bragg wave components), then a diversity in the ocean responses sensitivity will occur when using different radar frequencies. In our model, these effects have been addressed by the inclusion of the hydrodynamic modulation function, but this term appears to not fully represent all the effects induced by the non-linear modulation as the different sensitivity to the wind. In order to properly model that in the TSM, the equilibrium range parameter needs to be able to change according to the observed ocean Bragg wave component, i.e. to the radar frequency, otherwise the same sensitivity to the wind speed is modeled for any Bragg wavenumber, as shown in Fig. 3.13. This suggests an important contribution: the short wave spectrum equilibrium range parameter cannot be only a function of the wind speed (or friction velocity), but it may also include a relation with the ocean wavenumber,

yielding a dependence on the Bragg wavenumber and, in turn, on the radar frequency.

With the results of this analysis, we want to point out that, as for the case of the upwind/crosswind asymmetry, besides the physics of the ocean, it is essential to account for what the radars are sensitive to and then adjust the shape of the spectrum such that the ocean response is adapted to the Bragg wave component observed at a specific frequency. Next studies will be focused on investigating the modeling of this relation between the equilibrium range parameter and the ocean wave wavenumber, in order to optimize the agreement at C-band and also at other operational frequencies.

3.6   Conclusion

Several empirically-derived functions already exist to describe the relation between the ocean surface and the scatterometer signal to retrieve surface winds. However, they describe the ocean backscattering at a single frequency, they do not account for the physical interaction between the radar signal and the physics of the ocean and they may also fail in extreme wind conditions and rain events. A model able to reproduce, on a physical basis, the ocean response at any operational frequency represents an important contribution in the scientific community. Our goal is the definition of this theoretical model starting from two of the most frequently used frequencies in scatterometry, such as C-band and Ku-band. In this work, we have analyzed the parameters having major impact on the ocean response, we have derived a new configuration for them and we have discussed the main issues arising when trying to define a multi-frequency model.

The proposed model is based on the well-established Two-Scale Model (TSM), which strongly depends on the representation of the ocean surface wind wave spectrum. Our spectrum model relies on the Elfouhaily model for the omnidirectional component and on the Pierdicca and Pulvirenti model for the spreading function. From our analysis, the sensitivity of the ocean surface backscattering coefficient σ^0 to the wind speed is mostly driven by the equilibrium range parameter α_m, introduced in the omnidirectional spectrum of the short waves. This parameter establishes the relationship between the wind speed, the wave spectrum and in turn with σ^0, so that to properly model this sensitivity, it is essential to accurately define this parameter. We have started by analyzing the Ku-band and we have defined a new functional relationship of α_m with respect to the wind speed, where an exponential law at low winds and a linear law at high winds are patched together with a new patching function, to define a unified law for the whole wind speed range. The proposed new unified expression has been defined such that no frequency-based constraints have been included, that may prevent the model to work at different frequencies. This configuration yields a remarkable agreement with the Ku-band QuikSCAT scatterometer empirical model function as well as with the actual data with a mean bias ranging between -0.09 dB and 0.6 dB and a standard deviation between 0.9 dB and 1 dB. It also corrects the σ^0 misbehavior induced by the two-range logarithmic formulation presented by the Elfouhaily model. However, while such corrections are still valid when the proposed model is compared to the C-band empirical model, the agreement at C-band is not as good as for the Ku-band frequency. To further investigate the not-optimal agreement at C-band, we

have compared the ocean responses predicted by the C-band and Ku-band GMFs. The results demonstrate that, at these two frequencies, the σ^0 trends with respect to the wind speed behave differently. In particular at wind speeds lower than 10 m/s the C-band is less sensitive than the Ku-band. This is probably due to the different ocean Bragg wave components, which are regulated by different wind relations due to the non-linear wave-wave interactions and this leads to different ocean responses. Moreover, the predicted upwind/crosswind σ^0 asymmetry at C-band is about 1.2 dB higher than the Ku-band, especially at medium-high wind regimes. These diversities make the definition of a multi-frequency theoretical model even more complicated: this model should be able to not only describe the interaction between the radar signal and the ocean physics but, it also needs to account for the different sensitivity to the wind in both speed and direction, when using different radar frequencies. Our analysis reveals that by exploiting the relationships available in the literature, an equilibrium range parameter depending only on the wind speed as well as an upwind/crosswind asymmetry ($\Delta(k)_{PP}$), is not able to reproduce the diversity of the ocean response seen at different radar frequencies. The GMFs clearly show that there is a dependence on the radar frequency, suggesting that additional relations should be included in those parameters. Our test suggests that $\Delta(k)_{PP}$ needs to have higher values in the C-band Bragg wavenumber range, and the increasing values for $\Delta(k)_{PP}$ should be related to the values of the deviation between the Ku-band and C-band frequencies. On the other hand, the equilibrium range parameter should include not only a relation with the wind speed (or friction velocity) but it should also account for the ocean wavenumber, which would lead to a dependence on the Bragg wavenumber and then on the radar frequency.

It is worth noticing that, our new spectrum configuration defines a significant agreement at Ku-band and it better represents the ocean response at C-band, compared to the other models used in our analysis. However, in order to have an optimal agreement at any frequency, the difference in the radar sensitivity to the ocean when using different frequencies must be accounted for. This requires a full understanding of the sources of these differences and it requires a corresponding modification of the shape of the spectrum. We will investigate that in order to reach a final optimized configuration for a multi-frequency ocean response. Such investigation is left for future work.

Chapter IV

Theoretical Modeling in Rainy Conditions

4.1 Introduction to Surface Rain Effects on Ocean Scatterometry

Atmospheric rain has a strong impact on spaceborne scatterometer signal and several investigations have been carried out in order to understand and address the effects of the rain on scatterometer observations and wind retrievals at Ku-band radar frequency [Weissman *et al*., 2005; Weissman and Bourassa, 2008; 2011] as well as at C-band frequency [Lin *et al*., 2013; 2014; 2015].

The rain contaminates the scatterometer measurements in several ways: (i) Atmospheric rain modifies the scatterometer signal by introducing an attenuation factor once the signal passes through the atmosphere in both directions. This is mainly seen at rain rates higher than 5 mm/h. (ii) Rain increases the signal by adding a scattering contribution produced by the rain volume. (iii) Rain modifies the roughness of the surface by impinging on it. These "splash" effects modulate the distribution of the ocean waves, causing a modification of the ocean wave spectrum and in turn of the surface backscatter. (iv) Rain modifies the wind field by inducing downdraft phenomena, which often hit the ocean surface, leading to wind variability in speed and direction. Such variability causes a degradation of the quality of the scatterometer wind retrievals.

The strength of these rain effects on the scatterometer signal depends on the radar frequency, the higher the frequency, the larger the impact of the rain attenuation and the volume backscattering. Indeed, it is known that for Ku-band system, these two rain contributions have a significant impact, whereas for C-band scatterometers, they are relatively small. The rain-induced roughening of the ocean surface affects both C-band and Ku-band frequencies, but its effects are visible depending on the wind intensities and the instrument resolution. Recently, it has been recognized that the C-band signal is mainly affected by the rain-induced wind variability [Lin *et al*., 2015]. Specifically, the non-homogeneous winds induced by the rain-generated downdraft, increase the wind variability within the sampling errors, leading to artifacts in the wind retrievals that must be accounted for.

In order to provide reliable wind products to the users, several semi-empirical techniques have been developed to address the rain effects on scatterometer backscattered signal [Weissman *et al*., 2012]. Such techniques consist in: rain-contaminated data flagging [Haddlenston and Stiles, 2000], definition of advanced retrieval algorithm employing observation from passive radiometers [Hristova-Veleva *et al*., 2013], development of enhanced quality control systems [Portabella *et al*., 2012], development of backscatter semi-empirical models including both wind and rain effects [Draper and Long., 2004; Nie and Long, 2007] and use of neutral-network approach to map the radar backscatter to wind speed in all weather conditions [Stiles and Dunbar, 2010]. However, a full understanding of the impact of the rain is still under investigation.

Figure 4.1. Splash effects due to a raindrop falling onto the water surface [Contreras *et al*., 2003].

Many studies have tried to improve the theory of the radar observations of the ocean surface, in presence of rain. On the one hand, Le Mehaute (1988), Craeye *et al*. (1997; 1999), and Bliven *et al.* (1997), carried out laboratory studies, which identified the generation of surface ring waves as a dominant contribution in presence of rain. At scatterometer frequencies, such ring waves can come into resonance with the incident electromagnetic waves, so that they may increase the backscattered power. Sobiesky and Bliven, (1995) concluded that, although the rain-induced effects of crowns/crates and stalks are not negligible at Ku-band frequency, their effects are much smaller that the ring waves. A representation of these splash effects is illustrated in Fig. 4.1. By using data collected from the Kwajalein Experiment (KWAJEX), Contreras *et al.* (2003) have found that for wind speed below 10 m/s, the surface roughening effects induced by rain is stronger than surface wind effects, limiting the wind estimation. On the other hand, as presented by Tsimplis and Thorpe, (1989) and Nyusten (1990), rainfall had been also associated to short-gravity waves damping. In contrast to the ring-waves, this effect produces a decrease of the surface roughness, introducing a decrease of the ocean surface radar return. Based on these theories, Contreras and Plant, (2006) have presented a model of the ocean surface backscattering coefficient accounting for both wind and rain on theoretical basis. This model is based on a physical representation of the ocean surface roughness accounting for both ring waves and short-gravity wave damping. However, as the authors explained, the model has been tuned to match the measurements at Ku-band in both rainy and non-rainy conditions, and the simulations performed at other frequencies in absence of rain have not been validated with empirical model functions or real data. The evaluation of the rain effects has been also performed by Draper and Long (2004), but their model does not fully describe the modification of the ocean surface waves due to the impact of the raindrops.

Defining a theoretical model of the scatterometer backscatter able to account for the effects of both wind and rain is extremely challenging. Especially for the surface, a full understanding of the all the surface modifications induced by the impact of the raindrops is still an open issue, making the complete evaluation of the surface rain effects difficult to be performed. However, a theoretical model would represent a valuable contribution for several applications in scatterometry, such as studying the rain signature on the scatterometer observations, analyzing the uncertainty of the wind retrievals due to the rain. It would also provide the opportunity to jointly estimate wind and rain. Therefore, here we present our approach to build such a model, based on the work performed by Contreras and Plant. (2006). To describe the surface backscattering coefficient

in non-rainy conditions, we have used the Two Scale Model (TSM), where the new ocean surface wave spectrum configuration, as described in Chapter III, has been included (TSM-New). Although further investigations are needed in order to obtain a final form able to model the ocean surface backscattering at any frequency, the TSM-New shows significant results at Ku-band frequency. Hence, we use it here as backbone model to further investigate the ocean response in presence of rain.

4.2 Methodology

4.2.1 Rain-affected Ocean Wave Spectrum

To describe the ocean surface roughness modification caused by the rain, we have defined a rain-extended ocean surface wind wave spectrum, by including the effects of the ring waves and the rain-induced wave damping, in addition to the effect of the wind.

The wind wave damping is based on the theory proposed by Nyusten, (1990). This theory states that the attenuation of the ocean waves is due to the propagation of the kinetic energy caused by falling raindrops over the ocean surface and subsurface. The kinetic energy generates ripples on the surface, causing a turbulent layer, which overlays the background layer. The latter is the place where the ocean wind waves have the highest velocity, so that the superimposition of a turbulent layer causes the waves attenuation.

To characterize the ocean surface turbulent layer associated to the rain event, the theory of Nyusten relies on the concept of the "*eddy viscosity*". In fluid dynamics, the fluid turbulence is associated to eddies characterized by several length scales. It consists in the kinetic energy transfer from bigger eddies to smaller eddies, where the energy is then transformed into heat due to the effect of the viscous dissipation. The *eddy viscosity* v_e is used to model the turbulent phenomenon and it is expressed as the product of the turbulence length scale l, and velocity scale v. These quantities are described by the Kolmogorov theory as $l = (v^3/\varepsilon)^{1/4}$ and $v = (v\varepsilon)^{1/4} = (l\varepsilon)^{1/3}$, with v the kinematic viscosity and ε the dissipation rate of the kinetic energy. Therefore, modeling the turbulence requires the definition of l-v or l-ε [William, 2005; Landahl and Christensen, 1992].

To parameterize the turbulent layer generated by the raindrops falling into the ocean surface, the theory of Contreras and Plant, (2006) suggests that the size of the raindrop-generated eddies is equal to the diameter D of the raindrop, such that $l = D$, whereas the energy dissipation rate ε equals the raindrops kinetic energy flux $\mathbb{F}$, so that $\varepsilon = \mathbb{F}/d_{mix}$ with d_{mix} the mixing depth of the turbulent layer. Thus, the velocity scale v can be defined as:

$$v = \left(\frac{\mathbb{F}D}{d_{mix}\rho_w}\right)^{1/3},$$

(4.1)

where ρ_w is the water density, included after a dimensional analysis [Contreras and Plant, 2006]. Therefore, the eddy viscosity v_e, characterizing the turbulent layer due to the raindrops falling into the ocean surface can be defined as follows:

$$v_e \approx lv = D \left(\frac{\mathbb{F}D}{d_{mix}\rho_w}\right)^{1/3}. \tag{4.2}$$

Here, we have assumed $d_{mix} = 19$ cm as proposed by Contreras and Plant, (2006), based on the experiments conducted in a tank of 19 cm depth by Tsimplis, (1992). According to Eq. (4.2), it is necessary to define the kinetic energy flux $\mathbb{F}$ of the falling raindrops to completely characterize v_e. In this work, we have relied on the formulation proposed by Fox, (2004), who defined $\mathbb{F}$ as:

$$\mathbb{F} = 3.78^3 \frac{\pi\rho_w}{6} N_0 \frac{\Gamma(6+\mu)}{\Delta^{(6+\mu)}}, \tag{4.3}$$

where we have used $\Delta = \Delta(RR) = 4100RR^{-0.21}$ m^{-1} (with RR the rain rate), $\mu = 0$ and $N_0 = 8000$ m^{-4} as the Drop Size Distribution (DSD) parameters of the consolidated Marshall and Palmer DSD [Marshal and Palmer, 1948]. By this definition, v_e becomes a function of the rain rate.

Therefore, according to the theory proposed by Nyusten, (1990), the eddy viscosity can be used to compute the rain-induced enhanced attenuation of the ocean waves characterized by wavenumber k. Such attenuation is defined as follows:

$$A(k, RR)^{Ny90} = -4v_0 k^2 \left[\left(1 - e^{-2kd_{mix}}\right)\frac{v_e(RR)}{v_o} + e^{-2kd_{mix}}\right], \tag{4.4}$$

where v_0 is the dynamic viscosity of the background surface layer and v_e as defined in Eq. (4.2).

Base on this concept, in order to account for such wave damping, we have then used Eq. (4.4) as attenuation factor of the ocean wave spectrum in the small-scale wave range when the rain is present (rain rate $RR > 0$ mm/h). In absence of rain, there is not any turbulent layer so that the rain-induced wave attenuation is zero. Hence, we have parameterized such attenuation in the whole RR range as:

$$A(k, RR) = \begin{cases} A(k, RR)^{Ny90} & \text{for } RR > 0 \\ 0 & \text{for } RR = 0 \end{cases}. \tag{4.5}$$

In addition to the wave damping, we have included the effects of the ring waves since they are the dominant contributors in roughening the ocean surface. Experimental data allowed the development of a spectral model of the rain-generated ring waves. Such model is described by Bliven *et al.* (1997), and it is used here as an

additional contribution on the ocean surface short waves spectrum. The spectral shape of the ring waves is defined as a log-Gaussian wavenumber representation as shown in Eq. (4.6):

$$S(k, RR) = \frac{1}{2\pi} C_g S_{fp}(RR) \exp\left\{ -\pi \left[\frac{\ln\left(\frac{1}{2\pi f_p} \sqrt{gk + \frac{\tau}{\rho} k^3} \right)}{\frac{\Delta f}{f_p}} \right]^2 \right\} , \qquad (4.6)$$

where C_g, g, ρ and τ are the phase velocity, the acceleration due to gravity, the density of water and water surface tension ($\tau = 74$ cm^{3}s^{-2}). In this model, the peak frequency f_p and the bandwidth Δf are independent on RR, whereas the RR-dependence is shown by the spectral peak amplitude $S_{fp}(k, RR) = 0.06RR^{0.53}$. Thus, at $RR = 0$ mm/h, $S(k, 0) = 0$.

Therefore, our rain-extended omnidirectional curvature spectrum has been modeled such that:

$$B(k) = B(k)_l + \left[B(k)_h^{New} e^{-A(k,RR)} + k^3 S(k, RR) \right] , \qquad (4.7)$$

where $B(k)_l$ is the long wave curvature spectrum as expressed in Eq. (3.1) [Elfouhaily *et al*., 1997], $B(k)_h^{New}$ is our proposed short waves curvature spectrum, which includes the modified equilibrium range parameter as described in Eq. (3.6). It is worth pointing out that to define the directional spectrum, the spreading function is used to multiply only $B(k)_l$ and $B(k)_h^{New}$. Ring waves are isotropic, so that their contribution does not depend on the wind direction.

The results of the rain affected omnidirectional elevation and curvature spectrum are illustrated in Fig. 4.2(a) and Fig. 4.2(b), respectively. The spectrum has been computed at wind speed of 5 m/s and for rain rate values equal to 0 mm/h, 1 mm/h, 5 mm/h, 10 mm/h, 20 mm/h, 50 mm/h, 100 mm/h. To compute the wave damping, a distribution of raindrops having a mean diameter of 1.5 mm has been considered. The comparison between the rain affected and rain free models is also shown. The results are consistent to expectations. The rain-affected spectrum at wavenumber corresponding to the short waves increases with the rain intensity due to the effect of the ring waves. The wave damping contributes to the modification of the spectrum as can be seen in Fig. 4.3, however, this effect is much smaller compared to the ring waves' effects, as observed by Bliven *et al*., (1993), so that it cannot be seen in Fig. 4.2.
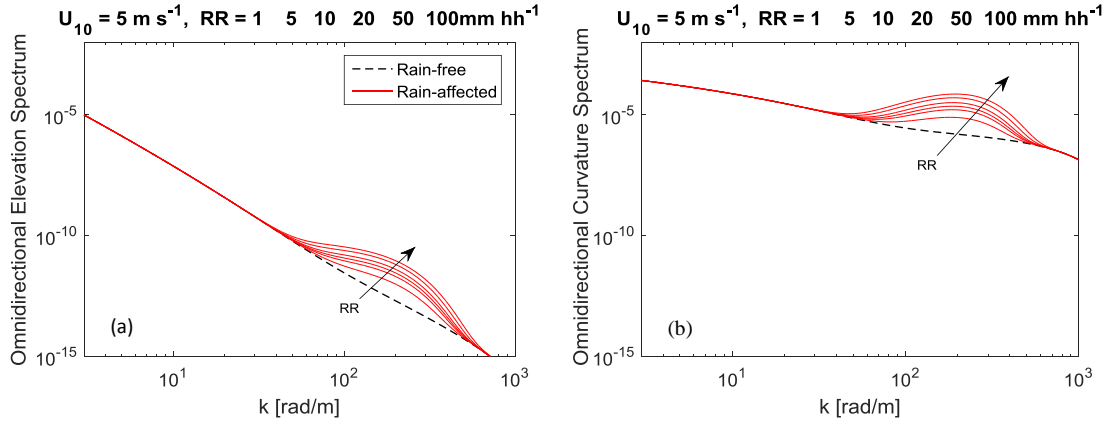
Figure 4.2. Omnidirectional elevation (a) and curvature (b) spectrum model where the tuned E spectrum of surface wind waves at wind speed U_{10} = 5 m/s is considered (dashed-black). The corresponding rain-affected spectra (solid-red) are computed for rain rate values equal to RR = 1, 5, 10, 20, 50, 100 mm/s. The black arrow points out the direction of the increasing rain intensity.
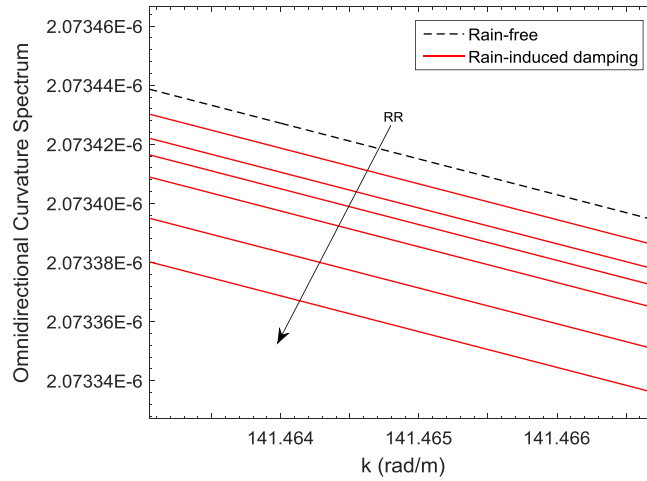

Figure 4.3. Zoom-in of the omnidirectional curvature spectrum model in the short wind waves region at wind speed U_{10} = 5 m/s. Comparison between the rain-free model (dashed-black) and rain-induced wave damping (solid-red). Rain values are RR = 1, 5, 10, 20, 50, 100 mm/h. The black arrow points out the direction of the increasing rain intensity.

4.2.2 Simulation of Rain-affected Surface Backscattering Coefficient

The Two-Scale Model (TSM) has been used to physically describe the ocean surface backscattering coefficient in presence of both wind and rain. To simulate the ocean backscattering, we have then properly modified the SEAWIND2 software, previously used to simulate the NRCS in clear weather, in order to include our rain-extended wind wave spectrum accounting for the ocean surface roughness modifications due to the raindrops' impact. We have then derived a new software version that has been called SEAWIND3.

We have first simulated the azimuthally-averaged Ku-band NRCS for wind speed of 7 m/s. The mean has been computed by averaging the NRCS for wind direction ranging between 0° to 90°. Such angles, frequency and wind speed have been chosen in order to meet the conditions proposed by Contreras and Plant, (2006). Their work has been used, here, to make comparisons with our results in order to firstly test the magnitude of the modeled rain effects. Different rain rates as RR = 0 mm/h, 1 mm/h, 10 mm/h, 40 mm/h have been considered and comparisons with the NRCS in non-rainy conditions have been also performed. The NRCS has been computed for incidence angles ranging between 40° and 60°. This range has been chosen according to the angles where the Ku-band GMF has been defined. We have included the comparison with the NRCS in non-rainy condition and the empirical GMF, in order to further prove the reliability of our model in clear air at different incidence angles. The results are shown in Fig. 4.4. A remarkable agreement between the proposed theoretical model in non-rainy conditions (TSM-wind) and the empirical GMF is obtained. Overall, the rain increases the NRCS, due to the dominant roughening of the ring waves. The model in rainy conditions (TSM-RR) agrees with the results shown in Fig. 5 of Contreras and Plant, (2006) (hereafter CP). However, our analysis differs from their work since it reveals that, within the range of 40° and 60°, the rain affects more lower incidence angles than higher angles. This difference is probably due to our different representation of the NRCS in non-rainy condition compared to their model. Additional tests have been also carried out for different wind speeds. Results are shown in Fig. 4.5 and 4.6 for 4 and 16 m/s, respectively. As expected, the rain effects on the ocean return are higher at lower winds. As the wind increases, the roughness generated by the wind prevails over the rain-induced modifications.
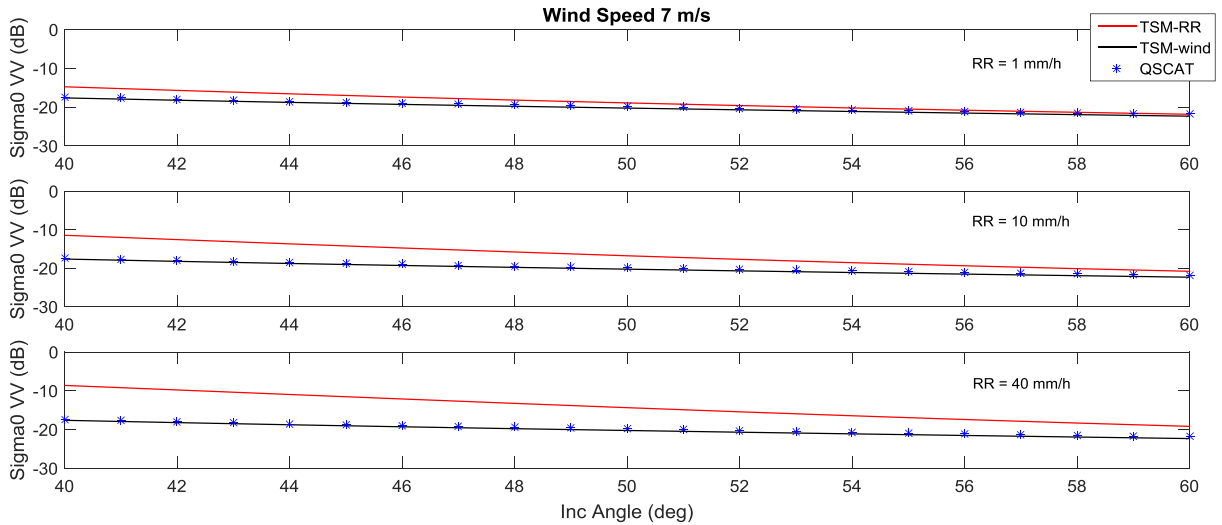
Figure 4.4. Simulations of azimuthally averaged Ku-band NRCS in vertical polarization, versus the incidence angles, with rain (red) and no rain (black), for wind speed of 7 m/s. Rain rates RR = 1 mm/h (top), 10 mm/h (middle) and 40 mm/h (bottom) have been analyzed, according to the work presented by Contreras and Plant, (2006). The model in non-rainy conditions is validated by comparing the results with the empirical GMF of Ku-band QuikScat (blue star).
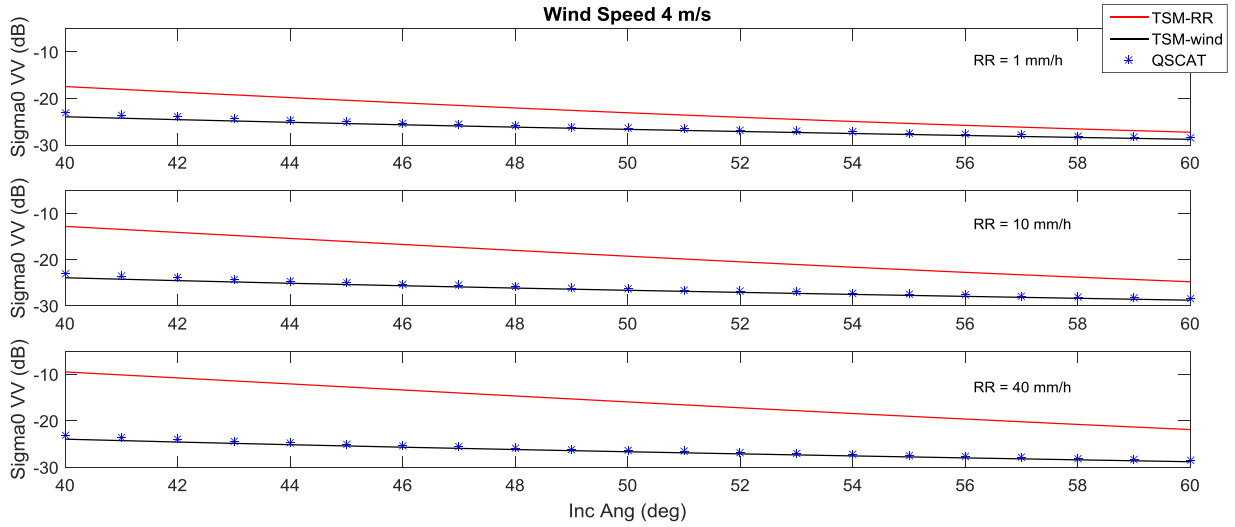
Figure 4.5. Simulations of azimuthally averaged Ku-band NRCS in vertical polarization, versus the incidence angles, with rain (red) and with no rain (black), for wind speed of 4 m/s. Rain rates RR = 1 mm/h (top), 10 mm/h (middle) and 40 mm/h (bottom) have been analyzed. The model in non-rainy conditions is validated by comparing the results with the empirical GMF of Ku-band QuikScat (blue star).
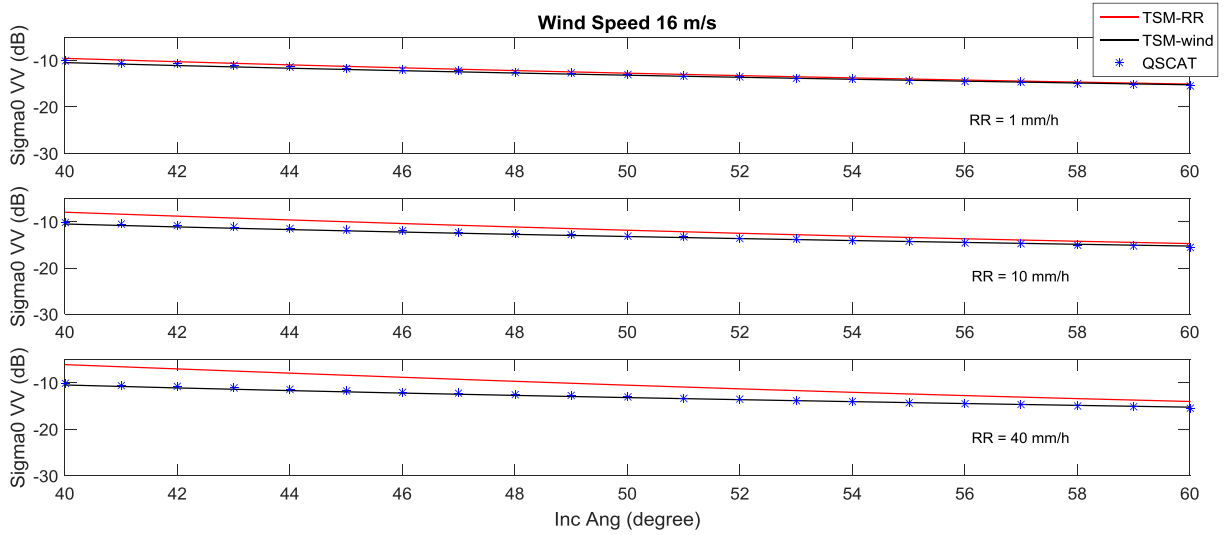
**Figure 4.6**. Simulations of azimuthally averaged Ku-band NRCS in vertical polarization, versus the incidence angles, with rain (red) and with no rain (black), for wind speed of 16 m/s. Rain rates RR = 1 mm/h (top), 10 mm/h (middle) and 40 mm/h (bottom) have been analyzed. The model in non-rainy conditions, for different incidence angles is validated by comparing the results with the empirical GMF of Ku-band QuikScat (blue star).

4.3   Validation in Presence of Rain

4.3.1 Simulated Wind and Rain Scenario

The rain effects on the ocean surface backscattering coefficient (σ^0) have been firstly evaluated in a simulated scenario. We have decided to focus on the Ku-band frequency due to the reliability of our model in non-rainy conditions. The analysis has been performed for an incidence angle θ equal to 40° and 54°, as for the case of clear air (Chapter 3).

We have first analyzed the effects on the σ^0 directional component. To do that, we have computed σ^0 in the whole wind direction (φ) range between 0° and 360°, for wind speeds covering low, medium, medium-high and high wind speed regimes, corresponding to 4 m/s, 10 m/s, 16 m/s and 20 m/s, respectively. The analysis has been performed for different rain rates as RR = 1 mm/h, 5 mm/h, 10 mm/h and 15 mm/h. The results are shown in Fig. 4.7 and Fig. 4.8 for θ equal to 54° and 40°, respectively. Overall, the rain causes an increase of σ^0 for the entire wind direction range. However, the rain tends to smooth the directionality of σ^0 and it reduces the upwind ($\varphi = 0°$) and crosswind ($\varphi = 90°$) asymmetry, which is essential to estimate wind direction from scatterometer observations. In particular, these effects are more evident at low wind speed and they increase for higher rain rates.
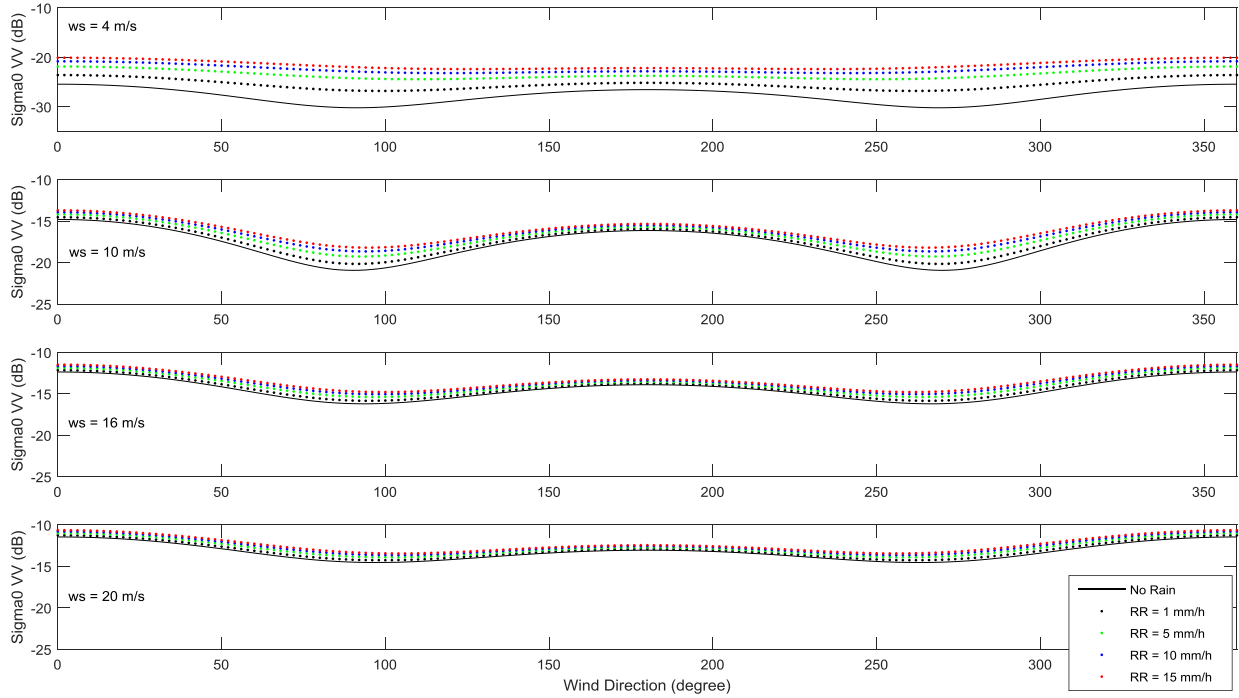
Figure 4.7. NRCS (σ^0) versus wind direction at an incidence angle equal to 54°. Comparisons are shown between σ^0 in non-rainy condition (black) and for RR equal to 1 mm/h (black-dotted), 5 mm/h (green-dotted), 10 mm/h (blue-dotted) and 15 mm/h (red-dotted). σ^0 is computed for wind speeds of 4 m/s, 10 m/s, 16 m/s and 20 m/s.
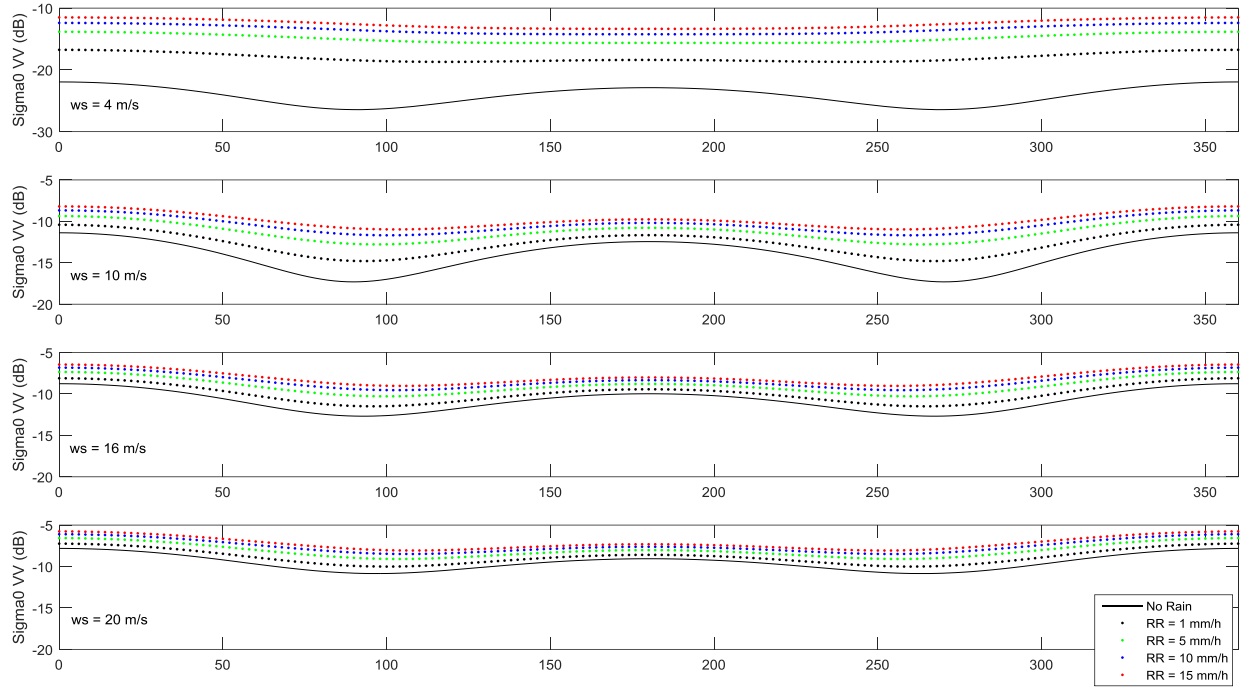
Figure 4.8. NRCS (σ^0) versus wind direction at an incidence angle equal to 40º. Comparisons are shown between σ^0 in non-rainy condition (black) and for RR equal to 1 mm/h (black-dotted), 5 mm/h (green-dotted), 10 mm/h (blue-dotted) and 15 mm/h (red-dotted). σ^0 is computed for wind speeds of 4 m/s, 10 m/s, 16 m/s and 20 m/s.

Table 4.1 shows the upwind/crosswind asymmetry for the different wind speeds and rain rates. For both incidence angles, the values confirm that as the rain rate increases, this asymmetry decreases more rapidly at lower winds than higher winds. This means that σ^0 in crosswind direction is more affected by the rain than in upwind direction. In contrary, σ^0 in downwind ($\varphi = 180°$) is less affected by the rain compared to the upwind, causing an increase of the upwind/downwind asymmetry, as shown in Table 4.2.

Table 4.1. Upwind/Crosswind asymmetry computed for different wind speeds (*ws*) and rain rates (*RR*). Two incidence angle are considered as θ equal to 54° and 40°.

| *Up/Cross* (dB)	*theta = 54 deg*					*theta = 40 deg*				
	RR = 0 mm/h	RR = 1 mm/h	RR = 5 mm/h	RR = 10 mm/h	RR = 15 mm/h	RR = 0 mm/h	RR = 1 mm/h	RR = 5 mm/h	RR = 10 mm/h	RR = 15 mm/h
ws = 4 m/s	4.769	3.133	2.360	2.055	1.890	4.484	1.69	1.271	1.153	1.095
ws = 10 m/s	6.142	5.628	5.075	4.715	4.463	5.924	4.364	3.362	2.908	2.649
ws = 16 m/s	3.825	3.662	3.465	3.326	3.223	3.906	3.344	2.852	2.586	2.422
ws = 20 m/s	3.039	2.943	2.825	2.740	2.676	2.989	2.682	2.383	2.209	2.099

Table 4.2. Upwind/Downwind asymmetry computed for different wind speeds (*ws*) and rain rates (*RR*). Two incidence angle are considered as θ equal to 54° and 40°.

Up/Down (dB)	*theta = 54 deg*					*theta = 40 deg*				
	RR = 0 mm/h	RR = 1 mm/h	RR = 5 mm/h	RR = 10 mm/h	RR = 15 mm/h	RR = 0 mm/h	RR = 1 mm/h	RR = 5 mm/h	RR = 10 mm/h	RR = 15 mm/h
ws = 4 m/s	1.101	1.571	1.882	2.022	2.098	0.928	1.635	1.793	1.835	1.849
ws = 10 m/s	1.334	1.415	1.513	1.584	1.638	1.066	1.255	1.423	1.513	1.567
ws = 16 m/s	1.539	1.601	1.678	1.734	1.776	1.213	1.33	1.447	1.515	1.559
ws = 20 m/s	1.599	1.654	1.724	1.774	1.813	1.247	1.349	1.450	1.510	1.550

Then, we have analyzed the σ^0 trend versus the wind speed for upwind, crosswind and downwind. The rain does not significantly affect higher winds in all the three cases and it is also evident that, at wind speed lower than 10 m/s, the crosswind direction is characterized by an enhanced increase compared to the other two directions. These results are shown in Fig. 4.9 for θ equal to 54°. Same trends are obtained for θ equal to 40°(not shown here).
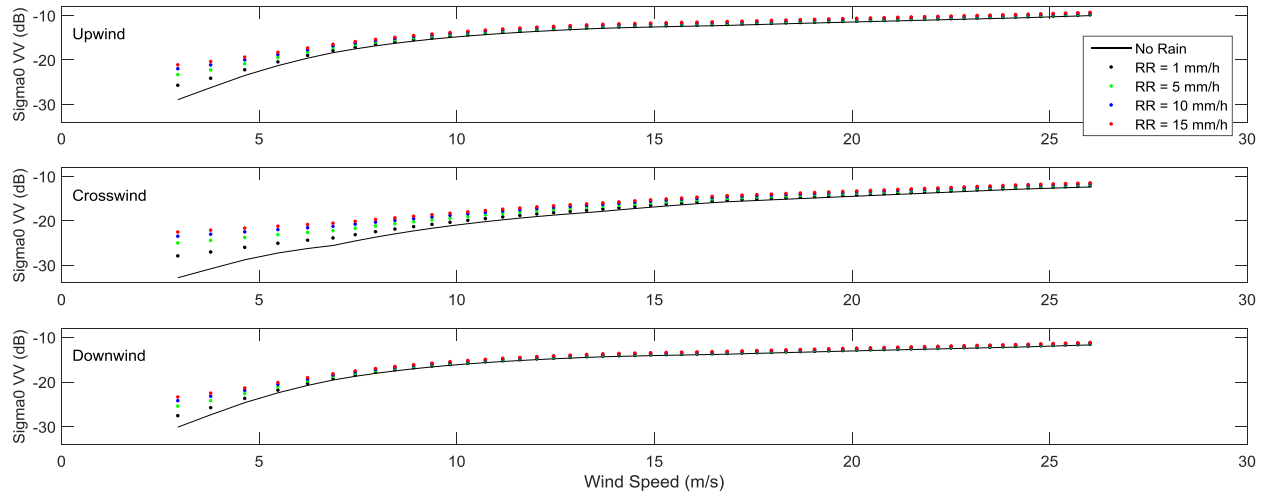

Figure 4.9. NRCS (σ^0) versus wind speed at an incidence angle equal to 54°. Comparisons are shown between σ^0 in non-rainy condition (black) and for RR equal to 1 mm/h (black-dotted), 5 mm/h (green-dotted), 10 mm/h (blue-dotted) and 15 mm/h (red-dotted). σ^0 is computed in upwind, crosswind and downwind directions.

4.3.2 Preliminary Analysis with Spaceborne Actual Data

As mentioned in Chapter III, the spaceborne data used in this work are those collected by the ADEOS-II mission, during 2003. By carrying the Ku-band SeaWinds scatterometer and Advanced Microwave Scanning Radiometer (AMSR), the ADEOS-II spacecraft allowed simultaneous observations of near-surface winds and rain. By receiving weak microwave radiation from the Earth's surface and atmosphere, AMSR measures physical parameters concerning water, such as water vapor, precipitation, sea surface temperature, sea surface wind and sea ice; therefore, a large dataset of collocated surface wind and rain is available from the ADEOSS-II mission. The data used in this analysis were kindly provided by NASA-*Jet Propulsion Laboratory* (JPL). The JPL Scatterometry Radar Science Team developed a retrieval algorithm to estimate geophysical parameters from AMSR observations. In presence of rain, this algorithm accounts for non-uniform beam filling and hydrometeor structure uncertainty in a new way. It uses a Rain Indicator (RI) to determine degree of homogeneity of the rain within the satellite's Field of View (FOV) and such information allows to choose the appropriate retrieval database to estimate the geophysical parameters of interest [Dunbar *et al*., 2006]. AMSR retrievals were used to correct and improve the SeaWinds σ^0 in presence of rain. Two models – empirical and physical – were developed by JPL to estimate the effect of atmospheric attenuation and rain volume backscattering on scatterometer measurements as a function of the retrieved geophysical parameters. Both corrections are provided within the user's data products and we have decided to use the data corrected from the physical method [Hristova-Veleva *et al*., 2006].

AMSR data are organized in 12-km Wind Vector Cell (WVC) Quadrants. A set of four WVC quadrants covers each of the 25-km WVC of the L2A σ^0 SeaWinds data. Figure 4.10 displays the arrangement of the AMSR wind vector cell quadrants in the WVCs in the spacecraft swath. Since SeaWinds data are provided as 1624x76 WVCs (covering the entire spacecraft swath and Earth circumference), we have decided to compute the mean of the AMSR measurements available in the four quadrants in order to have 1:1 correspondence between SeaWinds winds and AMSR rain rates measurements [Dunbar *et al*., 2006].
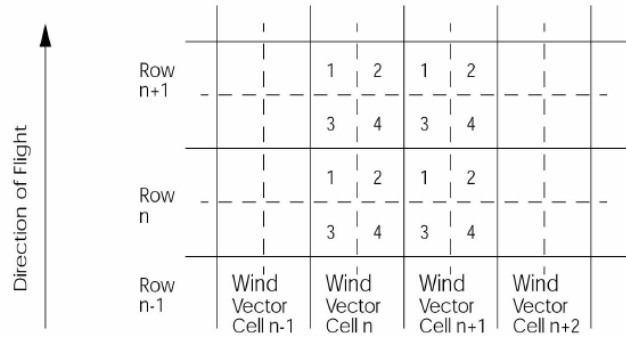

Figure 4.10. Arrangement of the AMSR quandrants in the corresponding Wind Vector Cell within the spacecraft swath [Dunbar *et al*., 2006].

As the scatterometer signal propagates through the atmosphere it interacts with the hydrometeors, water vapor and gases that are present there and they all act to attenuate the scatterometer signal (A_{atm}). In addition, in presence of heavy rain, the power that is backscattered by the precipitating raindrops (${\sigma^0}_{vol}$) adds up to the power scattered by the wind. Therefore, the full σ^0 measured by the scatterometer at the top-of-atmosphere (${\sigma^0}^{TOA}$) can be modeled as:

$$\sigma^{0^{TOA}} = {\sigma^0}_{surf} A_{atm} + {\sigma^0}_{vol} \, . \tag{4.8}$$

From Eq. (4.7), we have computed the surface contribution affected by both wind and rain (${\sigma^0}_{surf}$) to be compared with the model backscattering coefficient derived from our SEAWIND3 software. To do that, we have read from the SeaWinds data the $\sigma^{0^{TOA}}$, whereas from the AMSR dataset, we have focused on the measurements of A_{atm} and ${\sigma^0}_{vol}$ within the corresponding WVCs. The surface contribution determined from the data is illustrated in Fig. 4.11 for the fore and aft SeaWinds look directions. As for the clear air analysis, we have analyzed the data collected during Hurricane Isabel in 2003. We have focused on the orbit number 3927 and 3941 corresponding to September 15th from 1429 to 1611 UTC and September 16th from 1404 to 1545 UTC, respectively. The data are consistent to what it is expected. For light to moderate rain intensities, the attenuation prevails over the volume backscattering, causing a decrease of the radar return as the rain rate increases. Indeed, as shown in Fig. 4.11, ${\sigma^0}_{surf}$ is higher than $\sigma^{0^{TOA}}$ as the rain rate increases, due to the rain attenuation effect.

In order to compute the ocean surface backscattering coefficient from our rain-extended model, we have used the corresponding L2B surface wind vector in presence of rain, as well as and the rain rate estimates from
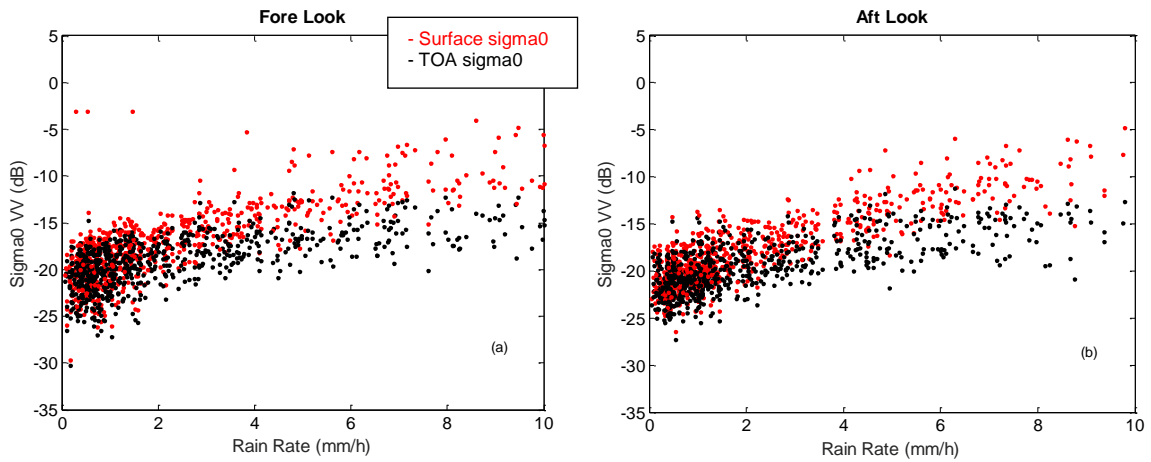
Figure 4.11. Ku-band Seawinds NRCS versus the collocated AMSR rain rate measurements. Surface contribution (red) and NRCS at the top-of-atmosphere (black) are shown.

AMSR data as input of the SEAWIND3 software. The rain rate values are needed to compute the contribution of ring waves and rain-induced damping in order to properly modify the spectrum in our optimized TSM. The SEAWIND3 software has been properly adjusted in order to read all these values directly from the corresponding data. Due to a limited speed of our processing system, we have decided to perform an analysis based on one single orbit, specifically the orbit number 3927. As for the clear air analysis, we have used those data from the outer beam (V pol), characterized by acceptable signal-to-noise ratio and acquired in the operating wind observation mode. For this analysis, rain-contaminated data have been selected by using the rain flag available in the corresponding L2A/L2B data products [Dunbar *et al.*, 2006].

The comparison between the surface σ^0 measured by the SeaWinds scatterometer (Sigma0$_{meas}$) and the surface σ^0 modeled with our extended TSM (Sigma0$_{TMS}$) in presence of rain, reveals that the model slightly underestimates the actual data with a mean bias of 1.8 dB and standard deviation of the difference of 2.8 dB, as shown in Fig. 4.12(a-b). By analyzing the difference between the modeled and measured sigma0, it is possible to notice that, besides the strength of the wind, the disagreement increases as the rain rate becomes higher. As shown in Fig. 4.3, the modeled damping rate of the short-gravity waves does not significantly affect the wave spectrum for increasing rain rates, suggesting that a possible over-attenuation of the surface waves is not the cause of such underestimation. Since the ring waves are the main contributors in the surface roughness modification, these results show that the ring waves do not fully cover the observed increase of the NRCS in presence of rain. This suggests that the additional roughening contributions from craters and stalks induced by the raindrops need to be accounted for. This is also shown by Fig. 4.13. The disagreement for wind speeds lower than 10 m/s, where the rain-roughening effects are expected to be more evident, is higher than for wind speed over 10 m/s and it also increases more rapidly as the rain rate increases. Such results are consistent with the observations of Contreras and Plant, (2006). They showed that an additional splash effect contribution is essential for agreement with Ku-band data at incidence angle higher that 50°.
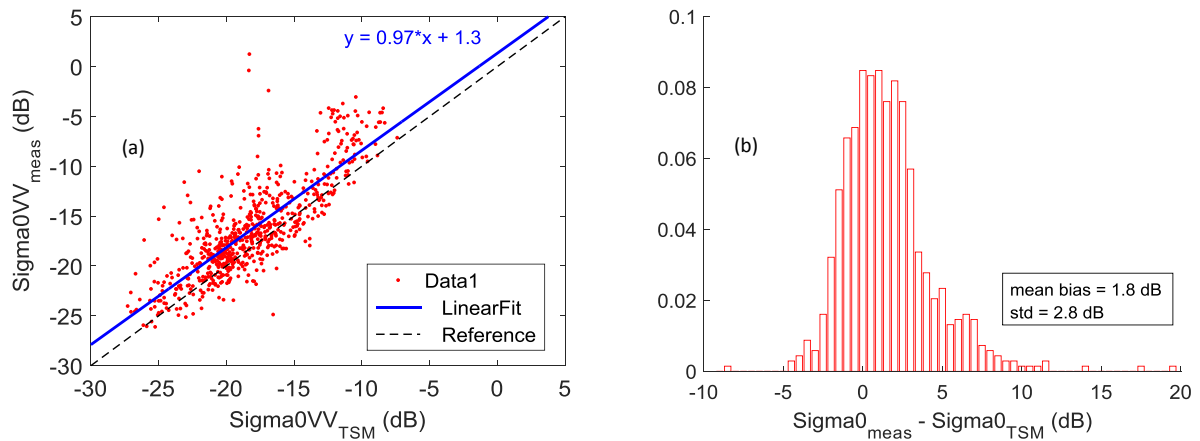
Figure 4.12. Scatterplot (a) of the modeled σ^0 with the rain-extended TSM versus the measured σ^0 with SeaWind scatterometer and normalized histogram (b) of the difference between the model and the measurements.
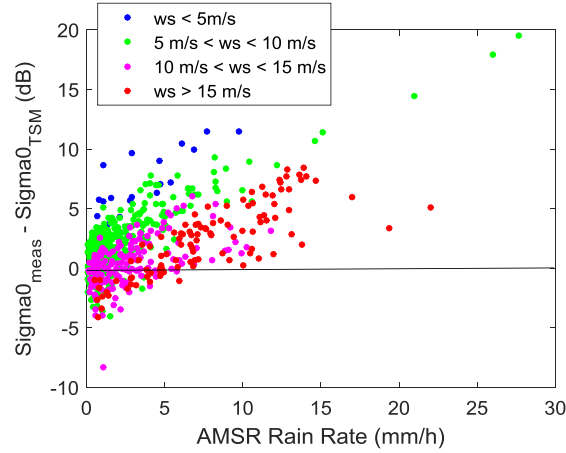
Figure 4.13. Difference between measured and modeled σ^0 versus AMSR rain rate. Different wind speed (ws) range are shown such as: ws < 5 m/s (blue), 5m/s < ws <10 m/s (green), 10 m/s < ws <15 m/s (magenta) and ws>15 m/s (red).

4.4   Summary and Conclusion

Rain compromises the scatterometer observations by introducing a volume backscattering and attenuation on the signal as well as by modifying the ocean surface roughness responsible for the surface radar return. The rain impact needs to be accounted for to derive corrected scatterometer wind retrievals. In this work, we have developed an approach to theoretically model the scatterometer surface backscattering coefficient in presence of rain. At this stage, we have not considered the volume backscattering and the rain attenuation.

To model the backscattering coefficient of the ocean surface perturbed by the impact of the raindrops, our approach consists in the development of an ocean wave spectrum model, which is dependent upon both wind and rain parameters. We have used our wind wave spectrum model described in Chapter III, as background of this new rain-extended wave spectrum. We have modified such model in the short-gravity and capillary waves range, by introducing the rain-induced wave damping and the generation of the ring waves. Such spectrum has been properly implemented in the SEAWIND2 software in order to simulate the ocean surface backscattering coefficient in presence of both wind and rain. We have then developed a new version of this software, which has been called SEAWIND3. The magnitude of the simulated rain affects on the ocean surface NRCS, as proposed in this work, is in agreement with the work proposed by Contreras and Plant, (2006).

The model has been firstly tested in a simulated scenario. With simulated wind and rain, the results show that the rain-generated ring wave effect is the dominant contribution, causing an overall increase of the NRCS of the ocean surface. Such effects are higher in low wind regimes than at higher wind regime, where the wind effects are expected to be dominant. In addition, the rain smoothes the directional component of the NRCS, suggesting that the rain may limit the possibility to correctly estimate wind direction from scatterometer

observations. The NRCS in crosswind direction increases more rapidly than in the upwind direction, causing a general decrease on the upwind/crosswind asymmetry essential for wind vector retrievals. On the other hand, the upwind/downwind asymmetry increases with the rain. Such results are consistent with previous observations of the rain effects on the ocean surface, proving that our proposed model properly addresses the contribution of the rain in the surface backscattering coefficient.

The validation has been also carried out in a real scenario by the inter-comparison with the Ku-band SeaWinds scatterometer onboard the ADEOS-II spacecraft. We have continued the analysis started in clear air, focusing on the case study of Hurricane Isabel in 2003 (Chapter III). We have analyzed the data in presence of rain according to the rain measurements collected by the AMSR instrument. Our preliminary results show that the proposed model slightly underestimates the SeaWinds NRCS. This underestimation is probably due to the fact that the model does not account for the additional splash effects as craters and stalks, which instead may have a significant impact especially at lower wind regimes. Additional tests are planned to test these assumptions, but they are in agreement with the observations of Contreras and Plant, who showed that these additional effects may affect the ocean response at Ku-band for incidence angles higher than 50°.

The validation reveals that this model properly represents the behavior of the ocean surface backscattering coefficient in presence of rain. In contrast with the model of Contreras and Plant, the proposed model has not been empirically tuned to match the Ku-band data. Adjustments have been done in clear air but they have been formulated in such a way to not include any empirical/arbitrary relation. In addition, compared to the model developed by Draper and Long, our model specifically accounts for the theoretical representation of the ocean surface modification induced by the rain. Therefore, although our model needs to be further investigated to obtain an optimal agreement with the data and to fully cover all the surface rain effects, it provides a significant improvement towards the theoretical modeling of ocean surface backscattering coefficient affected by rain and it proves to be a valuable tool for improving the knowledge of the scatterometer observations.

Chapter V
Conclusion and Future Work

The theoretical modeling of the ocean response is one of the most challenging tasks in ocean scatterometry. Empirical geophysical model functions (GMFs) are preferable by the scientific community to performed wind retrievals as well as wind analysis, and the ocean vector wind science team has reached high confidence on that. However, it has been also recognized that relying only on empirical models is not advisable, since they are based on other measurements affected by their own uncertainties and they are not able to fully account for the effects compromising the radar signal, such as very high wind conditions and rain events, causing additional uncertainty in the radar observations and wind estimates. A theoretical model has the big potential to describe the ocean response in a more complete way, helping the understanding of the physics of the observations and the development of improved model functions for more accurate wind retrievals. Especially now, as the ocean wind climate data records are improved and extended for studies of ocean/atmosphere interaction and Earth Climate system, reliable wind retrievals and deep knowledge of the scatterometer observations are critically needed. In this perspective, the objective of this research is to advance the theoretical modeling of the ocean surface backscattering coefficient, with the aim of understanding/addressing its limitations and to propose a new strategy towards a multi-frequency optimized model able to account for the effects of both wind and rain.

This work has been divided in two main steps, consisting in: (i) modeling the ocean response in clear air and (ii) extending the model in presence of rain. Before including any additional effect that contributes to the radar signal, it is essential to firstly determine a reliable model in absence of rain. Many attempts have been done in the past, but this topic remains highly debated within the scientific community. Moreover, measurement-based empirical tuning is often included, limiting the model applicability to just those conditions where the tuned relations are valid.

A single model able to operate at any frequency is highly desirable, however, such requirement is particularly difficult to achieve, since different radar frequencies are sensitive to different effects. For this reason, we have decided to perform this work starting from two of the most used frequencies in ocean scatterometry, such as C-band and Ku-band frequencies. To study and address the limitations of the theoretical modeling of the ocean backscattering, we have relied on the well-known Two-Scale Model based on the approach of Pierdicca and Pulvirenti, (2008). This model strongly depends on the representation of the ocean surface roughness, namely the ocean wind wave spectrum. According to the Bragg theory, the microwave scatterometer samples the ocean wave spectrum at a particular ocean wavenumber k_B, which changes according to the radar frequency but, it generally falls within the range of short wind-driven ocean surface waves. The wind/wave relation enclosed in the wave spectrum, regulates the $\sigma°$/wind relation in the TSM, so that the main

effort of this work was to identify and properly describe the spectrum parameters that mainly affect the wind/wave relation, in order to improve the TSM-based $\sigma°$ response to the wind-forcing.

We have carried out an inter-comparison among different wave spectrum models and based on the result, we have decided to rely on the model proposed by Elfouaily *et al.*, (1997). When this spectrum is ingested into the TSM (TSM-E), it leads to a significant disagreement with the GMF-based $\sigma°$, especially at lower wind regimes. Thus, our approach has consisted in investigating TSM-based $\sigma°$ in terms of the Elfouhaily spectrum model, in order to correct such disagreement. Our analysis reveals that, the spectrum parameter regulating the $\sigma°$/wind relation is the equilibrium range parameter (α_m), which mostly drives the wind speed/wave relation. This parameter can be interpreted as the representation of equilibrium condition among the strength of the surface wind, the water viscosity and the non-linear wave-wave interactions. This condition determines the distribution of the ocean wave energy over the different ocean wave components. We have carried out a careful analysis of the α_m models available in the literature and we have found that, in contrast with the two-range logarithmic law proposed so far - where the two ranges refer to low and high wind regimes - an exponential α_m at low winds (α_{m_exp}) and a linear α_m at high winds (α_{m_lin}) significantly reduce the disagreement between the theoretical and empirical models. In addition, we have shown that a unified α_m law remarkably improves the TSM-GMF agreement in the whole wind range and we have defined a new patching function that combines together α_{m_exp} and α_{m_lin}.

The validation of this model at Ku-band frequency shows that this relation leads to a very good agreement. Such validation has been performed by using the Ku-band QuikSCAT scatterometer GMF as well as the actual data collected by the Ku-band SeaWinds scatterometer onboard the ADEOS-II satellite, in 2003. Our work differs from others in that our spectrum adjustments are not the result of an empirical tuning relation derived by fitting the Ku-band $\sigma°$ measurements and we have not introduced any arbitrary value that leads to such optimized agreement. Therefore, it can be used to investigate other frequencies.

However, the validation performed at C-band frequency shows that this spectrum configuration slightly improves the agreement with the CMOD5 GMF and the results are not as good as for the Ku-band case. To explain such diversity, we have performed an inter-comparison between the C-band and the Ku-band GMFs. Such comparison reveals that the Ku-band frequency is more sensitive to the wind speed, meaning that slope of the $\sigma°$/wind speed relationship is slightly steeper than the C-band case. To reproduce such diversity, we have concluded that an α_m parameter as a function of only the wind speed does not meet this requirement. It is necessary to further modify the spectrum model to change the $\sigma°$/wind speed relationship according to the radar frequency. Based on our experience of the α_m, we have concluded that this can be achieved by properly defining α_m as a function of both wind speed (U) and ocean wavenumber (k) $\alpha_m(U, k)$. In this way, as the radar frequency changes, $\alpha_m(U, k = k_B)$ changes accordingly and in turn, the $\sigma°$ dependence on the wind speed. Similar results are achieved for the upwind/crosswind asymmetry. This can be explained as a consequence of the different ocean wave components observed at different radar frequencies (Bragg waves).

The non-linear wave-wave interactions modify the shape of the surface wave components and in turn the relation with the surface wind, causing different ocean responses when different radar frequencies are used.

Although we have not determined this new relation yet, the key point of this result is that, in order to obtained a theoretical model able to accurately describe the ocean response at any radar frequency, the different radar sensitivity to the wind must be accounted for. Scatterometers operating at different radar frequencies are sensitive to different ocean wave components, which are regulated by different wind/wave relations in order to keep the condition of equilibrium. This suggests new features of the ocean wave spectrum configuration and it reveals the importance of accurately modeling the equilibrium of the ocean waves. These new findings devise a new research path to further investigate the ocean surface backscattering coefficient towards a fully optimized multi-frequency theoretical model in non-rainy conditions.

At Ku-band frequency, the very good agreement between the empirical model and our proposed theoretical model in absence of rain, has allowed us to broaden our analysis in a combined wind/rain scenario. Thus, the second step of this research has been focused on extending our spectrum model to properly include the ocean surface modifications induced by the impact of the raindrops, on a theoretical basis. Based on the work proposed by Contreras and Plant, (2006), Bliven *et al.*, (1997) and Nyusten (1990), we have derived a new spectrum model that accounts for the generation of ring waves and the rain-induced short wave damping. In presence of rain, these two effects are known to be the main contributions to the ocean surface response. We have then analyzed the Ku-band ocean surface backscattering coefficient for different wind conditions and rain intensities. By focusing only on the ocean response, we have not considered the modifications of the radar signal due to atmospheric rain attenuation and volume backscattering.

The magnitude of the rain effects in the $\sigma°$ obtained with our rain-extended model has been first tested by comparing that to the model proposed by Contreras and Plant, (2006). The results reproduce fairly well their work, proving that the proposed model correctly represents the surface roughness modifications. Compared to the non-rainy $\sigma°$ trend, for incidence angle ranging between $40° - 60°$, our analysis reveals that the rain mainly affects lower incidence angles in this range, especially at low wind regimes, where the wind effects are expected to be small. In addition, the results show that the rain smoothes the directional component of $\sigma°$ by reducing the upwind/crosswind asymmetry and it also produces an overall increase of $\sigma°$ due to the dominant roughening effects of the ring-waves. All these results are consistent with previous work available in the literature [Draper and Long, 2004, Contreras et.al, 2003], but the advantage of our model in presence of rain is that it has not been empirically tuned to reproduce these results and it specifically accounts for the physical representation of the ocean surface modification induced by the rain.

However, our preliminary analysis using rain-affected actual data shows that our model slightly underestimates the rain effects. We have calculated the disagreement for different wind regimes and have shown that such disagreement increases with the rain rates and it is higher at lower winds than at medium-high winds. This suggests that the ring waves do not fully represent the $\sigma°$ increase due to the rain. Although the additional splash effects, as crowns/craters and stalks, are considered of a secondary order compared to the ring

waves, such effects cannot be neglected. To obtain an optimal agreement, they need to be accounted for, as also shown by Contreras and Plant.

Therefore, this work has revealed novel important features of the ocean surface backscattering coefficient and, by investigating the ocean wind wave spectrum in both rainy and non-rainy conditions, we were able to learn a lot about the mechanisms that regulate the frequency-specific model response with respect to the ocean waves. Although the adjustments developed so far still need a more complete physical interpretation and remaining inconsistencies need to be accounted for, our approach has demonstrated to be able to improve the theoretical modeling of the ocean backscatter and to help the interpretation of few open issues observed in the ocean response. From these findings, there is evidence that the wind wave spectrum modifications may be the key point to understand the physical reasoning of the differences seen in the scatterometer-specific observations. Such characterization may also help to understand the reason why external factors, like rain and SST, affect the ocean response differently when using different frequencies.

Additional analysis are already planned, consisting in using collocated Ku and C-band observations to advance the existing parameterizations for vertical and horizontal polarization, for a variety of incidence angles, in clear and rainy conditions, accounting for the rain attenuation and volume backscattering. The availability of a multi-frequency set of data from C-band ASCAT, Ku-band NASA SeaWinds, QuikSCAT and RapidScat scatterometers as well as AMSR-2 and WindSat microwave radiometers will offer the chance to effectively apply this methodology. Furthermore, such investigations will benefit from the new dataset offered by the very recent ISRO ScatSat-1 satellite that, by flying through a similar orbit plane of the C-band ASCAT, will provide for the first time a complete dataset of joint C/Ku-band measurements.

References

Apel, J. R., "An improved model of the ocean surface wave vector spectrum and its effects on radar backscatter," *J. Geophys. Res.*, vol. 99, n. 16, pp. 269-291, 1994.

Atlas, R., R. Hoffman, J. Ardizzone, S. Leidner, J. Jusem, D. Smith, and D. Gombos, "A Cross-Calibrated, Multiplatform ocean surface wind velocity product for meteorological and oceanographic applications," *Bull. Amer. Meteor. Soc.*, vol. 92, pp. 157–174, 2011, doi: 10.1175/2010BAMS2946.1.

Bliven, L., H. Branger, P. Sobieski, and J. P.Giovanangeli, "An analysis of scatterometer returns from a water surface agitated by artificial: evidence that ring-waves are the main feature," *Int. J. of Remote Sens.*, vol. 14, pp. 2315-2329.

Bliven L. F., P. W. Sobieski, C. Craeye, "Rain generated ring-waves: Measurements and modelling for remote sensing," *Int. J. of Remote Sens.*, vol. 18, no. 1, pp. 221-228, 1997.

Bourassa, M. A., S. T. Gille, D. L. Jackson, J. B. Roberts, and G. A. Wick, "Ocean winds and turbulent air-sea fluxes inferred from remote sensing," *Oceanography*, vol. 23, pp. 36–51, 2010(a), doi:10.5670/oceanog.2010.04.

Bourassa, M. A. and Co-Authors, "Remotely sensed winds and wind stresses for marine forecasting and ocean modeling," *Proc. of the OceanObs'09: Sustained Ocean Observations and Information for Society Conference (Vol. 2)*, Sept. 21-25, 2009, Hall, J., Harrison, D.E. & Stammer, D., Eds., ESA Publication WPP-306, 2010(b), doi:10.5270/OceanObs09.cwp.08.

Bourassa, M. A., E. Rodriguez, and R. Gaston, "NASA's Ocean Vector Winds Science Team workshops," *Bull. Amer. Meteor. Soc.*, vol. 91, 2010(c), doi:10.1175/2010BAMS2880.1

Bourlier C. and G. Berginc, "Microwave analytical backscattering models from randomly rough anisotropic sea surface – comparison with experimental data in C and Ku bands," *Progress in Electromagnetics Research*, vol. 37, pp. 31-78, 2002.

Bourlier C., N. Déchamps, and G. Berginc, "Comparison of asymptotic backscattering models (SSA, WCA, and LCA) from one-dimensional Gaussian ocean-like surfaces," *IEEE Trans. Geosci. Remote Sens.*, vol. 53, n. 5, pp. 1640–1652, 2005.

Brekhovskikh, L.M., "The diffraction of waves by a rough surface", *Zh. Eksper, i Teor. Fiz.*, vol. 23, pp. 275-289, 1952.

Contreras, R. F., W. J. Plant, W. C. Keller, K. Hayes, J. Nystuen, "Effects of rain on Ku-band backscatter from the ocean," *J. Geophys. Res.*, vol. 108, no. C5, 3165, 2003. doi:10.1029/2001JC001255.

Contreras R. F., and W. J. Plant, "Surface effect of rain on microwave backscatter from the ocean: Measurements and modeling," *J. Geophys. Res.*, vol. 111, no. C08019, 2006.

Cox C. and W. Munk, "Measurement of the roughness of the sea surface from photographs of the sun's glitter," *J. Opt. Soc. Amer.*, vol. 44, n. 11, pp. 838–850, 1954.

Craeye C., P. W. Sobieski, L. F. Bliven, "Scattering by artificial wind and rain roughened water surfaces at oblique incidences," *Int. J. of Remote Sens.*, vol. 18, no. 10, pp. 2241-2246, 1997. doi: 10.1080/014311697217864

Craeye C., P. W. Sobieski, L. F. Bliven, A. Guissard, "Ring-waves generated by water drops impacting on water surfaces at rest," *IEEE J. of Oceanic Engineering*, vol. 24, no. 3, 1999.

Cronin, M. and Co-Authors, "Monitoring ocean - Atmosphere interactions in western boundary current extensions," *Proc. of the OceanObs'09: Sustained Ocean Observations and Information for Society Conference (Vol. 2)*, Sept. 21-25, 2009, Hall, J., Harrison, D.E. & Stammer, D., Eds., ESA Publication WPP-306, 2010, doi:10.5270/OceanObs09.cwp.20.

DeMott, C. A., N. P. Klingaman, and S. J. Woolnough, "Atmosphere-ocean coupled processes in the Madden-Julian oscillation," *Rev. Geophys.*, vol. 53, pp 1099–1154, 2015, doi:10.1002/2014RG000478.

Donelan M. A., J. Hamilton, and W. H. Hui, "Directional spectra of wave generated waves," *Philos. Trans. R. Soc. Lond. A*, vol. 315, no. 1534, pp. 509–562, 1985.

Donelan, M. A., and W. J. P. Pierson, "Radar scattering and equilibrium ranges in wind-generated waves with application to scatterometry," *J. Geophys. Res.*, vol. 92, pp. 4971-5029, 1987.

Draper, D. W., and D. G. Long, "Evaluating the effect of rain on SeaWinds scatterometer measurements," *J. Geophys. Res.*, vol. 109, no. C02005, 2004. doi:10.1029/2002JC001741.

Dunbar S. and Co-authors, "SeaWinds Science Data Product User's Manual", 2006. [Available online at: ftp://podaac-ftp.jpl.nasa.gov/OceanWinds/seawinds/L2B12/docs/SWS_SDPUG_V2.0.pdf].

Durden S. and J. Vesescky, "A physical radar cross-section model for a wind-driven sea with swell," *IEEE J. Ocean. Eng.*, vol. OE-10, no. 4, pp. 445–451, 1985.

Elfouhaily T., B. Chapron, K. Katsaros, and D. Vandemark, "A unified directional spectrum for long and short wind-driven waves," J. *Geophys. Res.*, vol. 102, no. C7, pp. 15781-15796, 1997.

Fairall, C. and Co-Authors, "Observations to quantify air-sea fluxes and their role in climate variability and predictability, " *Proc. of OceanObs'09: Sustained Ocean Observations and Information for Society (Vol. 2)*, Venice, Italy, Sept. 21-25 2009, Hall, J., Harrison, D.E. & Stammer, D., Eds., ESA Publication WPP-306, 2010, doi:10.5270/OceanObs09.cwp.27.

Fois F., (2015) "Enhanced Ocean Scatterometry," Ph.D. Dissertation, Dept. Geoscience and Remote Sensing, University of Technology, Delft, The Netherlands, doi:10.4233/uuid:06d7f7ad-36a9-49fa-b7ae-ab9dfc072f9c.
Fois F., P. Hoogeboom, F.L. Chevalier, and A. Stoffelen, "An analytical model for the description of the full-polarimetric sea surface Doppler signature," *J. Geophys. Res.*, vol. 120, no. 2, pp. 988-1015, 2015.

Fox N., "Technical note: The representation of rainfall drop-size distribution and kinetic energy," *Hydrology and Earth System Sciences*, vol. 8., no. 5, pp. 1001-1007, 2004.

Fore A. G., B. W. Stiles, A. H. Chau, B. A. Williams, R. S. Dunbar and E. Rodriguez, "Point-Wise wind retrieval and ambiguity removal improvements for the QuikSCAT climatological data set," *IEEE Trans. on Geosci. and Remote Sens.*, vol. 52, n. 1, pp. 51-59, 2014. doi: 10.1109/TGRS.2012.2235843.

Fung, A. and K. Lee, "A semi-empirical sea spectrum model for scattering coefficient estimation, " *IEEE J. of Oceanic Eng.*, vol.7, n.4, pp.166-176, 1982.

Hasselmann and Co-authors, "Measurements of wind-wave growth and swell during the Joint North Sea Wave Project (JONSWAP), *Dtsch. Hydrogr. Z.*, vol. 12, 1973.

Hersbach H., A. Stoffelen, and S. de Haan, "An improved C-band scatterometer ocean geophysical model function: CMOD5," *J. Geophys. Res.*, vol. 112, no. C3, C03006, pp. 1-18, . 2007.

Hersbach, H., (2008), "CMOD5.N-A C-band geophysical model function for equivalent neutral wind". *ECMWF Technical memorandum*, n. 554.

Holliday, D., "Resolution of a controversy surrounding the Kirchhoff approach and the small perturbation method in rough surface scattering theory," *IEEE Trans. Antennas Propag*., vol. 35, n. 1, pp. 120-122, 1987.

Hristova-Veleva, S., P. Callahan, R. Dunbar, B. Stiles, S. Yueh, J. Huddleston, S. Hsiao, G. Neumann, B. Vanhoff, R. Gaston, E. Rodriguez, D. Weissman, "Revealing the winds under the rain. Part I: Passive microwave rain retrievals using a new observation-based parameterization of subsatellite rain variability and Intensity-Algorithm description," *J. Appl. Meteor. Climatol.*, vol. 52, pp. 2828–2848, 2013. doi: 10.1175/JAMC-D-12-0237.1.

Hristova-Veleva, S. M., and Co-authors, "Revealing the SeaWinds ocean vector winds under the rain using AMSR. Part I: The physical approach," *14th Conf. on Satellite Meteorology and Oceanography*, Atlanta, GA, 2006. [Available online at: https://ams.confex.com/ams/Annual2006/techprogram/paper_104160.htm].

Huddleston, J., and B. Stiles. "A multi-dimensional histogram technique for flagging rain contamination on QuikSCAT," *Proc. IEEE Int. Geosci. and Remote Sens. Symp.*, Honolulu, HI, vol. 3, pp. 1232-1234, 2000. doi: 10.1109/IGARSS.2000.858077.

Hwang, P.A., D. M. Burrage, D. W. Wang, and J. C. Wesson, "Ocean surface roughness spectrum in high wind condition for microwave backscatter and emission computations,". *J. Atmos. Oceanic Technol.*, vol. 30, pp. 2168–2188, 2013.

Jelenak Z., Steyn-Ross M. and Jelenak A. (1998), "Wind Parameters from Scatterometry", *Publication of University of Waikato*, New Zealand. [Available online at:
http://eng.waikato.ac.nz/pdfs/remote_sensing/Wind_scatterometry_ARSC98_paper.pdf]

Johnson J. T., "A study of ocean-like surface thermal emission and reflection using Voronovich's small slope approximation," *IEEE Trans. Geosci.Remote Sens.*, vol. 43, n. 2, pp. 306–314, 2005.

Johnson J. T., "An efficient two-scale model for the computation of thermal emission and atmospheric reflection from the sea surface," *IEEE Trans. Geosci. Remote Sens.*, vol. 44, n. 3, pp. 549–559, 2006.

Kudryavtsev, V. N., V. K. Makin, and B. Chapron, "Coupled sea surface-atmosphere model 2. spectrum of short wind waves," *J. Geophys. Res.*, vol. 104, n. C4, pp. 7625-7639, 1999.

Kudryavtsev V. N., D. Hauser, G. Caudal, and B. Chapron, "A semiempirical model of the normalized radar cross-section of the sea surface. 1 Background model," *J. Geophys. Res.*, vol. 108, n. C3, 8054, pp. 2 1-2 24, 2003.

Landahl M. T., E. Mollo-Christensen (1992), "Turbulence and random processes in fluid mechanics (2nd ed.)". Cambridge University Press, ISBN 978-0521422130.

Lemaire D., P. Sobieski and A. Guissard, "Full-range sea surface spectrum in nonfully developed state for scattering calculations," *IEEE Trans. on Geosci. and Remote Sens*, vol. 37, no. 2, pp. 1038-1051, 1999, doi: 10.1109/36.752222

Le Mehaute, B. "Gravity-capillary rings generated by water drops," *J. Fluid Mech.*, vol. 197, pp. 415–427, 1988.

Lin, W., M., Portabella, A., Stoffelen, A., Verhoef, D., Weissman, T., Johnson, J., Wolf,. "Towards a correction of ASCAT ocean measurements for rain effects", *ESA Living Planet Symp,* 2013. [Available online at: http://seom.esa.int/LPS13/0d9f3342/ESA_Living_Planet_LIN20130827_MP3.pdf].

Lin, W., M., Portabella, A., Stoffelen, A., Turiel, A., Verhoef, "Rain identification in ASCAT winds using singularity analysis," *IEEE Geosci. and Remote Sens. Letters*, vol. 11, pp.519-1523, 2014.

Lin, W., M., Portabella, A., Stoffelen, A., Verhoef, A., Turiel, "ASCAT wind quality control near rain," *IEEE Trans. on Geosci. and Remote Sens.*, vol. 53, no. 8, pp. 4165-4177, 2015.
doi: 10.1109/TGRS.2015.2392372.

Lin, W., M. Portabella, A. Stoffelen, J. Vogelzang, A. Verhoef, "ASCAT wind quality under high subcell wind variability conditions," *J. Geophys. Res. Oceans*, vol. 120, no. 8, pp. 5804–5819, 2015. doi: 10.1002/2015JC010861, 2015.

Liu, Y., X. Yan, W. Liu, and P. Hwang, "The probability density function of ocean surface slopes and its effects on radar backscatter," *J. Phys. Oceanogr.*, vol. 27, pp. 782–797, 1997.
doi: 10.1175/1520-0485(1997)027<0782:TPDFOO>2.0.CO;2.

Marshall J. S. and W. Mc K. Palmer, "The distribution of raindrops with size". *J. Meteor.*, vol. 5, pp. 165–166, 1948.

Nie C., and D. G. Long, "A C-band wind/rain backscatter model," *IEEE Trans. on Geosci. and Remote Sens.*, vol. 45, no. 3, pp. 621-631, 2007. doi: 10.1109/TGRS.2006.888457.

Nystuen, J. A. "A note on the attenuation of surface gravity waves by rainfall," *J. Geophys. Res.*, vol. 95, pp. 18,353–18,355, 1990.

Phillips O. M., "Spectral and staitistical properties of the equilibrium range in the wind-generated gravity waves," *J. Fluid Mech.*, vol. 156, pp. 505-531, 1985.

Pierdicca N. and L. Pulvirenti, "Comparing scatterometric and radiometric simulations with geophysical model functions to tune a sea wave spectrum model," *IEEE Trans. on Geosci. and Remote Sens*., vol. 46, no. 11, pp. 3756-3767, 2008.

Plant, W. J., "A two-scale model of short wind-generated waves and scatterometry," *J. Geophys. Res.*,vol. 91, n. C9, pp. 10735–10749, 1986. doi:10.1029/JC091iC09p10735.

Plant, W. J., "A stochastic, multiscale model of microwave backscatter from the ocean," *J. Geophys. Res*., vol. 107, n. C9, 3120, 2002.

Portabella, M., and Stoffelen, A., "Rain detection and quality control of SeaWinds, " *J. Atm. and Ocean Techn*., vol. 18, n. 7, pp. 1171-1183, 2001.

Portabella, M., A., Stoffelen, W., Lin, A., Turiel, A., Verhoef, J., Verspeek, J., Ballabrera-Poy, "Rain effects on ASCAT-retrieved winds: Toward an improved quality control," *IEEE Trans. on Geosci. and Remote Sens*., vol. 50, pp. 2495-2506, 2012. doi:10.1109/TGRS.2012.2185933.

Ricciardulli L., and F. J. Wentz, "A scatterometer geophysical model function for climate-quality winds: QuikSCAT Ku-2011," *J. Atmos. Oceanic Technol.*, vol. 32, no. 10, pp. 1829–1846, 2015.

Romeiser, R., and W. Alpers, "An improved composite surface model for the radar backscattering cross section of the ocean surface: Model response to surface roughness variations and the radar imaging of underwater bottom topography," *J. Geophys. Res*., vol. 102, n. C11, pp. 25251–25267, 1987.

Sobieski P., A. Guissard, and C. Baufays, "Synergic inversion technique for active and passive microwave remote sensing of the ocean," *IEEE Trans. Geosci. Remote Sens.*, vol. 29, n. 3, pp. 391–406, 1991.

Sobieski, P. W., and L. F. Bliven, "Analysis of high speed images of raindrop splash products and Ku-band scatterometer returns," *Int. J. of Remote Sens.*, vol. 16, pp. 2721-2726, 1995.

Soisuvarn S., Z. Jelenak, P. S. Chang, S. O. Alsweiss, Q. Zhu, "CMOD5.H—A high wind geophysical model function for C-band vertically polarized satellite scatterometer measurements," *IEEE Trans. on Geosci. and Remote Sens.*, vol. 51, no. 6, pp. 3744-3760, 2013.

Spencer M. W., C. Wu and D. G. Long, "Improved resolution backscatter measurements with the SeaWinds pencil-beam scatterometer *IEEE Trans. Geosci. Remote Sens.*, vol. 38, no. 1, pp. 89-104, 2000.

Stiles B. W., B. D. Pollard and R. S. Dunbar, "Direction interval retrieval with thresholded nudging: a method for improving the accuracy of QuikSCAT winds," *IEEE Trans. on Geosci. and Remote Sens.*, vol. 40, n. 1, pp. 79-89, 2002. doi: 10.1109/36.981351.

Stiles B. W. and R. S. Dunbar, "A neural network technique for improving the accuracy of scatterometer winds in rainy conditions," *IEEE Trans. on Geosci. and Remote Sens*., vol. 48, no. 8, pp. 3114-3122, 2010. doi: 10.1109/TGRS.2010.2049362.

Stoffelen, A., (1998), "Scatterometry, " PhD Thesis, ISBN 90-393-1708-9.

Stoffelen A., Verspeek J., Vogelzang J., Wang Z., Verhoef A., Ricciardulli L., "Reconciliation of C and Ku-band Geophysical Model Functions," *Int. Ocean Vector Wind Science Team Meeting*, May 17-19, 2016, Sapporo, Japan. [Available online at: https://mdc.coaps.fsu.edu/scatterometry/meeting/docs/2016/Wed_PM/GMFs.pdf].

Tang W., S. H. Yueh, A. Fore, G. Neumann, A. Hayashi, G. Lagerloef, "The rain effect on Aquarius L band sea surface brightness temperature and radar scattering," *Remote Sens. of Envir.*, vol. 137, pp. 147-157, 2013.

Thomson, J., E. A. D' Asaro, M. F. Cronin, W. E. Rogers, R. R. Harcourt, and A. Shcherbina, "Waves and the equilibrium range at Ocean Weather Station P, " *J. Geophys. Res. Oceans*, vol. 118, pp. 5951‑5962, 2013. doi:10.1002/2013JC008837.

Tsimplis, M., and S. A. Thorpe, "Wave damping by rain", *Nature*, vol. 342, pp. 893-895, 1989.

Tsimplis, M., "The effect of rain in calming the sea," *J. Phys. Oceanogr.*, vol. 22, pp. 404–412, 1992.

Ulaby, F. T., R. K. Moore, and A.K. Fung, (1982), "Microwave remote sensing: Active and passive, Vol. II -- Radar remote sensing and surface scattering and emission theory", Addison-Wesley.

Valenzuela, G. R., "Theories for the interaction of electromagnetic waves and oceanic waves. A review, " *Bound. Layer Met.*, vol. 13, no. 1, pp. 61-85, 1978.

Verhoef A., M. Portabella, A. Stoffelen and H. Hersbach, "CMOD5.n - the CMOD5 GMF for neutral winds," *Ocean and Sea Ice SAF, Tech. Rep. SAF/OSI/CDOP/KNMI/TEC/TN/165*, 2008.

Verhoef A. and J. Vogelzang; J. Verspeek; A. Stoffelen, "Long-term scatterometer wind climate data records," *J. Sel. Topics Applied Earth Obs. and Rem. Sens*, vol. PP, no.99, pp.1-9, 2016, doi: 10.1109/JSTARS.2016.2615873.

Voronovich, A. G., "Small-slope approximation for electromagnetic wave scattering at a rough interface of two dielectric half-spaces". *Waves in Random and Complex Media*, vol. 4, n. 3, pp. 337-367, 1994.

Voronovich A. G., V. U. Zavorotny, V. G. Irisov, "Sea-roughness spectrum retrieval from radar and radiometric measurements," in *Proc. IGARSS*, vol. 7, pp. 3102–3104, 2000.

Voronovich A. G. and V. U. Zavorotny, "Theoretical model for scattering of radar signals in Ku- and C-bands from a rough sea surface with breaking waves," *Waves Random Media*, vol. 11, no. 3, pp. 247-269, 2001.

Wang Z., A. Stoffelen and A. Verhoef, "Ku-band scatterometer SST sensitivity and geophysical model function," *2016 IEEE Int. Geosci. and Remote Sens. Symp.,* Beijing, 2016, pp. 4629-4632. doi: 10.1109/IGARSS.2016.7730208.

Weissman, D. E., G., Apgar, J. S., Tongue., M. A. Bourassa, "Correcting scatterometer winds by removing rain effects," *Bulletin of the American of Meteorological Society*, vol. 86, pp. 621-622, 2005.

Weissman, D. E., and M. A., Bourassa, "Measurements of the effect of rain-induced sea surface roughness on the QuikSCAT scatterometer radar cross section," *IEEE Trans. on Geosci. and Remote Sens,* vol. 46, pp. 2882-2894, 2008.

Weissman, D. E., and M. A. Bourassa, "The influence of rainfall on scatterometer backscatter within tropical cyclone environments - Implications on parameterization of sea surface stress," *IEEE Trans. on Geosci. and Remote Sens.,* vol. 49, pp. 4805-4814, 2011. doi: 10.1109/TGRS.2011.2170842.

Weissman D. E., B. W. Stiles, S. M. Hristova-Veleva, D. G. Long, D. K. Smith, K. A. Hilburn, and W. L. Jones, "Challenges to satellite sensors of ocean winds: addressing precipitation effects," *J. Atmos. Oceanic Technol.*, vol. 29, no.3, pp. 356-374, 2012.

Wentz, F. J., and D. K. Smith, "A model function for the ocean-normalized radar cross section at 14 GHz derived from NSCAT observations," *J. Geophys. Res.*, vol. 104(C5), pp. 11499–11514, 1999, doi:10.1029/98JC02148.

Wentz F. J. and L. Ricciardulli, "Improvements to the vector wind climate record using RapidScat as a common reference and Aquarius/SMAP for high winds in rain," *RSS Technical Report 111313, Remote Sensing Systems*, Santa Rosa, 2013.

Wentz F. J., and Co-Authors, "Evaluating and extending the ocean wind climate data record," *J. Sel. Topics Applied Earth Obs. and Rem. Sens.,* 2016, [Online: http://ieeexplore.ieee.org/stamp/stamp.jsp?arnumber=7820114].

William G. K., (2005), "Lectures in turbulence for the 21st Century," Department of Thermo and Fluid Engineering, Chalmers University of Technology, Göteborg, Sweden. p 64. [Available online at: http://www.turbulenceonline.com/Publications/Lecture_Notes/Turbulence_Lille/TB_16January2013.pdf].

Wright, J. W., "A new model for sea clutter", *IEEE Trans. Antennas and Propagation*, vol. 16, n. 2, pp. 217-223, 1968.

Yueh, S. H., R. T. Shin, and J. A. Kong, "Scattering of electromagnetic waves from a periodic surface with random roughness, " J. *Appl. Phys.*, vol. 64, pp. 1657-1670, 1988.

Yueh S. H., R. Kwok, F. K. Li, S. V. Nghiem, W. J. Wilson, and J. A. Kong, "Polarimetric passive remote sensing of ocean wind vectors," *Radio Sci.*, vol. 29, n. 4, pp. 799-814, 1994.

Yueh S. H., "Modeling of wind direction signals in polarimetric sea surface brightness temperatures," *IEEE Trans. on Geosci. and Remote Sens.*, vol. 35, n. 6, pp. 1400-1418, 1997.

Acknowledgements

This work would have never been possible without the support of my family, who has always encouraged me to keep following my dreams. A special thank goes to Fedele, because he has hold my hand and he has never left me alone since then, thank you for everything !

I am mostly grateful to my advisor Prof. Frank Marzano (Sapienza University of Rome). We have worked together since I got the Bachelor degree and his guidance and help has always inspired me. Thank you for always supporting me in any new scientific challenge I decided to face. I really appreciated the availability and help of the Ph.D. Program Coordinator, Prof. Maria-Gabriella Di Benedetto (Sapienza University of Rome). I would like to express my gratitude for her support, guidance and prompt emails, which were essential during these years. Thanks also to Prof. Nazzareno Pierdicca (Sapienza University of Rome) and Dr. Luca Pulvirenti (CIMA Research Foundation) for giving me the opportunity to continue their work and for sharing their experience.

I really cannot find the right words to express how much grateful I am to my advisors Dr. Joe Turk (Jet Propulsion Laboratory) and Dr. Svetla Hristova Veleva (Jet Propulsion Laboratory). Thank you for your technical help, valuable advices, your patience during our meetings and for letting me be part of the JPL ocean scatterometry group. This was a unique experience from the scientific and personal point of view. I will never forget anything of that. I would like to thank also Dr. Ernesto Rodriguez (Jet Propulsion Laboratory) and Dr. Bryan Stiles (Jet Propulsion Laboratory) for their valuable scientific support and for sharing their knowledge anytime I needed. Thanks to Dr. Ziad Haddad (Jet Propulsion Laboratory) for giving the chance to join his group.

I would like also to thank Prof. Simona Bordoni (California Institute of Technology) and Prof. Mark Bourassa (Florida State University) for their valuable contribution in reviewing this work.

Many thanks to all of the JPL colleagues and friends, who have contributed to this unforgettable experience. Many thanks also to the DIET collogues and friends, especially to Walter for being such a good friend during these years and for keeping me posted while I was in USA. Last but not least, thanks to Martina and Gloria, the best friends ever !

List of Acronyms

ADEOS	Advanced Earth Observation Satellite
AMSR	Advanced Microwave Scanning Radiometer
ASCAT	Advanced Scatterometer
CDR	Climate Data Record
DMSP	Defense Meteorological Satellite Program
EBC	Extended Boundary Condition
ECMWF	European Centre for Medium-range Weather Forecasting
ERS	European Remote-sensing Satellite
ESA	European Space Agency
EUMETSAT	European Organization for the Exploitation of Meteorological Satellites
FOV	Field of View
GMF	Geophysical Model Function
ICM-CSIC	Institut de Ciences de Mar- Consejo Superior de Investigaciones Científicas
ISRO	Indian Space Research Organization
ISS	International Space Station
JPL	Jet Propulsion Laboratory,
KNMI	Royal Netherland Meteorological Institute
KWAJEX	Kwajalein Experiment
NASA	National Aeronautic and Space Administration
NOAA	National Oceanic and Atmospheric Administration
NRCS	Normalized Radar Cross Section
NSCAT	NASA Scatterometer
NWP	Numerical Weather Prediction
OSCAT	Ocean-satellite Scatterometer
OVWST	Ocean Wind Vector Science Team
QuikSCAT	Quick Scatterometer
RapidScat	Rapid Scatterometer
RSS	Remote Sensing Systems

ScatSat	Scatterometer Satellite
SMAP	Soil Moisture Active Passive
SMOS	Soil Moisture and Ocean Salinity
SPM	Small Perturbation Method.
SSA	Small Slope Approximation
SSMI	Special Sensor Microwave Imager
SSMIS	Special Sensor Microwave Imager Sounder
SST	Sea Surface Temperature
TSM	Two-Scale Model
WindSat	Wind Satellite

List of Publications

A. *The relevance and originality of this work has been published/presented in the following papers/conferences:*

- F. Polverari, S. M. Hristova-Veleva, F. J. Turk, N. Pierdicca, L. Pulvirenti, F. S. Marzano, "New ocean wind wave spectrum configuration towards an optimized theoretical model of multi-frequency scatterometry," *IEEE Trans. on Geosci. and Rem. Sens.,* 2016, (under review).

- F. Polverari, F. S. Marzano, L. Pulvirenti, N. Pierdicca, B.W. Stiles, S. M. Hristova-Veleva, F. J. Turk, "Addressing the rain effects on ocean wind scatterometry at C and Ku band: modification of the ocean surface backscattering coefficient", *ESA Living Planet Symp.* 2016, May 9-13, 2016, Prague, Czech Republic.

- F. Polverari, F. S. Marzano, L. Pulvirenti, N. Pierdicca, B.W. Stiles, S. M. Hristova-Veleva, F. J. Turk, "Addressing the rain effects on the ocean scattering: a theoretical model of the ocean surface backscattering coefficient in presence of both wind and rain", *International Ocean Vector Wind Science Team (IOVWST) Meeting*, May 17 - 19, 2016, Sapporo, Japan.

- F. Polverari, F. S. Marzano, L. Pulvirenti, N. Pierdicca, B.W. Stiles, S. M. Hristova-Veleva, F. J. Turk, "Addressing the polarization signature of the ocean scattering at Ku band in presence of both non homogenous winds and rain", 2015 *American Geophysical Union (AGU) Fall Meeting*, Dec. 14 - 18, 2015, San Francisco, California, USA.

- F. Polverari, F. S. Marzano, L. Pulvirenti, N. Pierdicca, S. M. Hristova-Veleva, F. J. Turk, "Modeling ocean wave surface to simulate spaceborne scatterometer observations in presence of rain," Proc. of *IEEE Int. Geosci. and Remote Sens. Symp. (IGARSS),* pp.1203-1206, Jul. 26 – 31, 2015, Milan, Italy. doi: 10.1109/IGARSS.2015.7325988.

- F. Polverari, F. S. Marzano, L. Pulvirenti, N. Pierdicca, S. M. Hristova-Veleva, F. J. Turk, "Combining wind and rain in spaceborne scatterometer observations: modeling the splash effects in the sea surface backscattering coefficient", *International Ocean Vector Wind Science Team (IOVWST) Meeting*, May 19 – 21, 2015, Portland, Oregon, USA.

B. *Additional research activities have been carried out during the Ph.D. course, concerning the analysis of the rain signature in Synthetic Aperture Radar (SAR) imagery over ocean. This work has been published in the following papers:*

- S. Mori, F. Polverari, L. Mereu, L. Pulvirenti, M. Montopoli, N. Pierdicca, F. S. Marzano, "Atmospheric precipitation impact on synthetic aperture radar imagery: Numerical model at X and KA bands," Proc. of *IEEE Int. Geosci. and Remote Sens. Symp. (IGARSS),* pp. 1582-1585, Jul. 26 - 31, 2015, Milan, Italy. doi: 10.1109/IGARSS.2015.7326085.

- F. Polverari, S. Mori, L. Pulvirenti, N. Pierdicca, F.S. Marzano, "Precipitation Signature on Side-looking Aperture Radar Imaging: Sensitivity Analysis to Surface Effects at C, X and Ku band", Proc. of *European Microwave Week-EuRAD 2014*, Oct. 5 - 10, 2014, Rome, Italy. doi: 10.1109/EuRAD.2014.6991241.

- S. Mori, F. Polverari, L. Pulvirenti, M. Montopoli, N. Pierdicca, F.S. Marzano, "Modeling atmospheric precipitation impact on synthetic aperture radar imagery at X and Ka bands", Proc. of *SPIE Remote Sensing 2014*, Sept. 22 - 25, 2014, Amsterdam, Netherlands. doi: 10.1117/12.2067376.

- <u>F. Polverari</u>, S. Mori, L. Pulvirenti, N. Pierdicca, F.S. Marzano, "Modeling the Polarimetric Response to Atmospheric Precipitation on Synthetic Aperture Radar Imagery over Ocean", Proc. of *XX RiNEm 2014*, Sept. 15 - 18, 2014, Padova, Italy.

- S. Mori, <u>F. Polverari</u>, L. Pulvirenti, M. Montopoli, N. Pierdicca, F. S. Marzano, "High resolution spatial analysis of a hurricane structure by means of X-band and Ka-band satellite synthetic aperture radar", Proc. of *ERAD 2014 – 8th European Conference on Radar in Meteorology and Hydrology*, Sept. 1 - 5, 2014, Garmisch-Paterkirchen, Germany.